November 2014

Single-Phase Turbulent Enthalpy Transport

Bradley J. Shields
University of Massachusetts Amherst

SINGLE-PHASE TURBULENT ENTHALPY TRANSPORT

A Thesis Presented

by

BRADLEY SHIELDS

Submitted to the Graduate School of the
University of Massachusetts Amherst in partial fulfillment
of the requirements for the degree of

MASTER OF SCIENCE IN MECHANICAL ENGINEERING

September 2014

Mechanical and Industrial Engineering

SINGLE-PHASE TURBULENT ENTHALPY TRANSPORT

A Thesis Presented

by

BRADLEY SHIELDS

Approved as to style and content by:

David P. Schmidt, Chair

Blair Perot, Member

Stephen Nonnenmann, Member

Donald Fisher,
Department Head
Mechanical and Industrial Engineering

To Palermo

ACKNOWLEDGMENTS

I would like to thank my advisor Prof. David Schmidt for the opportunity to pursue my Master's degree. He has been a source of guidance and wry wit during the course of my study here. For that, I am very grateful. Thanks also to Professors Blair Perot and Stephen Nonnonmann for serving on my committee. I would also like to thank Professor Perot for putting up with my unannounced visits to his office over the years, whether they were for his classes or not.

I would like to thank Mom and Dad, for their constant support and uncanny ability to ignore the passage of years and dollars. I can't thank you enough. Thank you to my friends and labmates, for helping me through late nights and long days. You've made Amherst a great place to be.

I acknowledge the financial support of the General Motors company and the National Aeronautics and Space Administration.

ABSTRACT

SINGLE-PHASE TURBULENT ENTHALPY TRANSPORT

SEPTEMBER 2014

BRADLEY SHIELDS

B.S., UNIVERSITY OF MASSACHUSETTS AMHERST

M.S.M.E., UNIVERSITY OF MASSACHUSETTS AMHERST

Directed by: Professor David P. Schmidt

Vapor generation is central to the flow dynamics within fuel injector nozzles. Because the degree of atomization affects engine emissions and spray characteristics, quantification of phase change within diesel fuel injectors is a topic of design interest. Within the nozzle, the large pressure gradient between the upstream and downstream plena induce large velocities, creating separation and further pressure drop at the inlet corner. When local pressure in the throat drops below the fluid vapor pressure, phase change can occur with sufficient time. At the elevated temperatures present in diesel engines, this process can be dependent upon the degree of superheat, motivating the modeling of heat transfer from the wall.

By modeling cavitation and flash boiling phenomena as a departure from equilibrium conditions, the HRMFoam model accurately reproduces canonical adiabatic flows. An experimentally determined relaxation time controls the rate at which vapor

is generated, and includes model constants tuned for water and a diesel fuel surrogate. The model is shown to perform well for several benchmark experimental cases, including the work of Reitz, Lichtarowicz, and Nurick.

With the implementation of the Farve-averaged energy equation, the present work examines and validates the transport of enthalpy through the fixed heat flux and fixed wall temperature boundary conditions. The pipe heat transfer experiments of Boelter and Allen are replicated using the kEpsilon, Realizable kEpsilon, and Spalart-Allmaras models. With proper turbulence model selection, Allen's heat transfer coefficient data is reproduced within 2.9%. Best-case bulk temperature rise prediction is within 0.05%. Boelter's bulk temperature rise is reproduced within 16.7%. Turbulent diffusivity is shown to determine radial enthalpy distribution.

TABLE OF CONTENTS

Page

ACKNOWLEDGMENTS . . . . . **v**

ABSTRACT . . . . . **vi**

LIST OF FIGURES . . . . . **xi**

CHAPTER

1. LITERATURE REVIEW: PHYSICS **1**

1.1 Vapor Generation and Bubble Growth 2
1.2 Geometric Considerations 4

2. LITERATURE REVIEW: TWO-PHASE CRITICAL FLOW MODELING **8**

2.1 Limiting Assumption Models 9

2.1.1 Homogeneous Equilibrium Model 9
2.1.2 Slip Flow 9

2.2 Empirical and Two-Fluid Models 10

2.2.1 Frozen Flow 10
2.2.2 Bubble Dynamics Modeling 11
2.2.3 Homogenous Relaxation Model 14
2.2.4 Two-Fluid Models 17
2.2.5 Modern Modelers 18

3. PRELIMINARY WORK: VALIDATION CASES **20**

3.1 Elevated Temperature 20
3.2 Low Velocity Flow 25
3.3 Inlet Rounding 27
3.4 Coefficient of Discharge Benchmark Comparison 32

4. PRELIMINARY WORK: PARAMETER TUNING STUDY 34

5. HEAT TRANSFER: EXPERIMENTAL CASES AND COMPUTATIONAL IMPLIMENTATION 46

5.1 Transport of Energy and HRMFoam 47
5.2 Enthalpy Boundary Conditions 52

5.2.1 Specified Heat Flux: Allen Experiment 52
5.2.2 Numerical Approach: Allen 53
5.2.3 Specified Surface Temperature: Boelter Experiment 58
5.2.4 Numerical Approach: Boelter 59

5.3 Turbulence Models 60

5.3.1 kEpsilon 60
5.3.2 Realizable kEpsilon 62
5.3.3 Spalart-Allmaras 62

6. COARSE MESH APPROACH 63

6.1 Near-wall Boundary Layer Modeling 63
6.2 Coarse Mesh Results 66

7. FINE MESH APPROACH: SPECIFIED HEAT FLUX 75

7.1 Results 75

7.1.1 kEpsilon 76
7.1.2 Realizable kEpsilon 78
7.1.3 Spalart-Allmaras 79

7.2 Near-wall Enthalpy Curves 81
7.3 Conclusions 82

8. FINE MESH APPROACH: SPECIFIED SURFACE TEMPERATURE 83

8.1 Results 83

9. MODULE INTERACTION TESTING 86

10. CONCLUSIONS AND FUTURE WORK 89

APPENDIX: ENERGY TRANSPORT EQUATION IMPLIMENTATION 91

BIBLIOGRAPHY 92

LIST OF FIGURES

Figure **Page**

1.1 Generic pressurve vs. temperature diagram 2

1.2 Enthalpy vs. temperature diagram for a two-phase system 2

1.3 Reynolds number vs. Coefficient of Discharge for Lichtarowicz 7

1.4 Critical pressure ratio vs. L/D ratio for 0.25 inch inner diameter tube 7

2.1 Rayleigh's Bubble Nomenclature 11

2.2 Plesset's Experimental Bubble Radius in Time 13

2.3 Downar-Zapolski Relaxation Time 15

3.1 Computational Mesh used in Reitz simulations 21

3.2 Closeup of computational mesh used in Reitz simulations, inlet corner. 22

3.3 HRMFoam and Reitz experiments 23

3.4 Tabulated HRMFoam simulation and Reitz experimental data 24

3.5 HRMFoam low velocity flow results, by Reynolds Number. 25

3.6 Lichtarowicz's compiled experimental results 26

3.7 Inlet rounding's effects on coefficient of discharge 27

3.8 Torres' raw flow rate data 28

3.9 Mesh used for Torres validation cases 28

3.10 Closeup of mesh used for Torres validation cases 29

3.11 Torres' 10MPa experimental and HRMFoam data 30

3.12 Tabulated Torres' 10MPa experimental and HRMFoam data 30

3.13 Torres' 20MPa experimental and HRMFoam data 31

3.14 Tabulated Torres' 20MPa experimental and HRMFoam data 31

3.15 Nurick Theory vs. Experiments 32

3.16 State of system before optimization. 33

3.17 Tabulated HRMFoam vs. Nurick data 33

4.1 Pressure values for parametric study 36

4.2 State of system before optimization. 36

4.3 Computational grid used for parametric study 37

4.4 Increased mesh density at inlet corner on mesh used in parametric study 38

4.5 Steepest descents tabulated parameter study data 40

4.6 Parameter study V_N values tabulated across each case. 41

4.7 Parameter Values separated by iteration and search step. 43

4.8 Parameter coefficient of discharge values by iteration 43

4.9 Close-up of parameter study coefficient of discharge values by iteration. 44

4.10 Tabulated coefficient of discharge parameter study data, by iteration. 45

5.1 Local heat transfer coefficient, Allen [1] 53

5.2 Experimental temperature and local heat transfer coefficient 54

5.3 Streamwise velocity vs. transverse distance 55

5.4 Converged turbulent diffusivity α_t field 56

5.5 Allen simulation velocity, pressure, and vapor fraction 57

5.6 Tube dimensions for test section used in the UCLA water experiments [6] 58

5.7 Boelter high-temperature, high-pressure water experimental data [6] 59

6.1 Boundary Layer Regions 64

6.2 Meshes for use with wall functions 66

6.3 Turbulence Kinetic Energy for the coarse mesh Allen and Boelter cases 68

6.4 Turbulence Dissipation Rate for the coarse mesh Allen and Boelter cases 69

6.5 Turbulent Diffusivity for the coarse mesh Allen and Boelter cases 70

6.6 Enthalpy for the coarse mesh Allen and Boelter cases 71

7.1 Side-view of computational domain 76

7.2 Normalized heat transfer coefficient vs. axial pipe location, HRMFoam with kEpsilon 77

7.3 Turbulent diffusivity for the kEpsilon turbulence model 77

7.4 Normalized heat transfer coefficient vs. axial pipe location, HRMFoam with Realizable kEpsilon 78

7.5 Turbulent diffusivity for the Realizable kEpsilon turbulence model 79

7.6 Normalized heat transfer coefficient vs. axial pipe location, HRMFoam with Spalart-Allmaras 80

7.7 Turbulent diffusivity for Spalart-Allmaras 80

7.8 Axial Near-Wall Enthalpy, Allen [1] 81

8.1 Boelter simulation velocity, pressure, and vapor fraction 84

8.2 Boelter simulation enthalpy and turbulent diffusivity 85

9.1 Mesh used to test interaction of compressibility and heat transfer 86

9.2 Enthalpy and velocity for single-phase compressible heat transfer 87

9.3 Pressure for single-phase compressible heat transfer 87

9.4 Vapor fraction and turbulent diffusivity for single-phase compressible heat transfer 88

CHAPTER 1

LITERATURE REVIEW: PHYSICS

Within an automotive internal combustion engine, the process of phase change heavily influences spray mechanics and overall performance. Fuel injector atomization determines engine power and emissions. In this processes, fuel forced through the injector's diminutive orifice experiences a pressure drop. If the pressure drop lowers the pressure of the fluid below the vapor pressure, the flow may begin to change phase. If the downstream pressure is also below the vapor pressure, the vapor will not recondense, yielding a vapor/liquid mixture at the nozzle exit.

The process of a medium's phase change from liquid to vapor is thermodynamically identical whether it occurs via predominantly enthalpy or pressure [10]. Figure 1.1 shows a system comprised of some simple substance (represented by the red dot) in the liquid phase. Applying enough enthalpy to move the system across the saturated liquid/vapor line (while holding pressure constant) causes the liquid to become vapor by boiling; if instead the system is depressurized at constant temperature, cavitation takes place. In practice, the phase change process is gradual and a combination of the two; raising the temperature increases the vapor pressure, whereby a relatively smaller drop in pressure is able to cause phase change. Figure 1.2 shows this process in more detail - once sufficent enthalpy moves the system out of the subcooled region into the two-phase region, vapor generation occurs. The mass fraction of vapor x increases as enthalpy is added, until the fluid is completely converted to vapor in the superheated region.

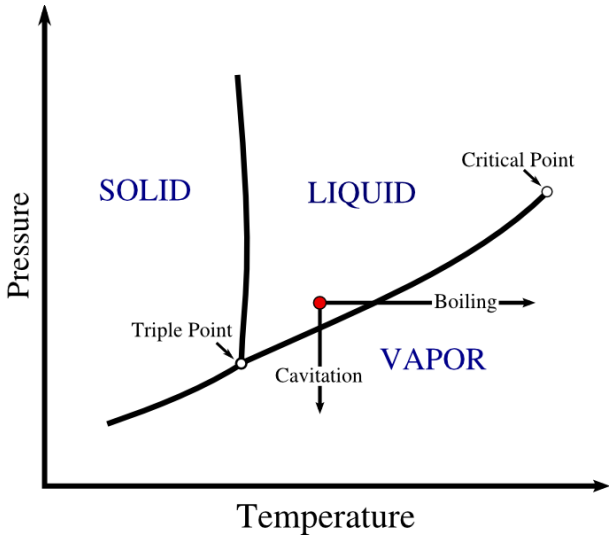

Figure 1.1: Generic pressure vs. temperature diagram for a material; system state represented by red dot.

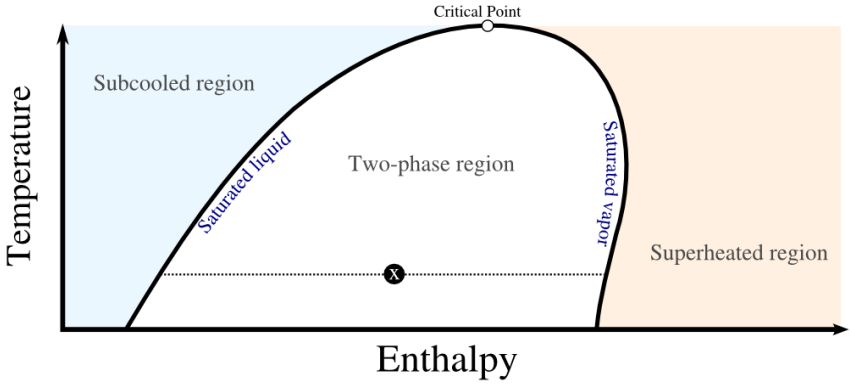

Figure 1.2: Enthalpy vs. temperature diagram for a two-phase system. Mass vapor fraction (x) increases from left to right in the two-phase region.

1.1 Vapor Generation and Bubble Growth

Once the pressure within a fluid has dropped below the vapor pressure, the flow is considered metastable, and bubble nucleation can occur. Disturbances such as density fluctuation or variable composition (dissolved particles/gasses) can lead to bubble formation [10]. More specifically, this process is separated into heterogeneous and homogeneous formation. Heterogeneous formation stems from wall roughness and inconsistencies in composition. Homogeneous formation comes from microscopic

density fluctuations due to Brownian motion and is dependent on the degree of superheat [11] [27]. Once vapor nuclei form, they grow or dissolve based on pressure fluctuations. Surface tension resists the bubble's growth; if the pressure difference across the edge of the bubble balances the surface tension, the bubble will survive [39].

If the bubble does not collapse, growth occurs as fluid evaporates at the bubble wall. Early on, surface tension is the primary limiting factor. Once the bubble roughly doubles in size from its original radius, the difference between the vapor pressure and the exterior pressure drives growth rapidly [39]. In hot ambient conditions, once the bubble is large enough, evaporation at the wall is driven by heat from the surrounding liquid. At high temperature, vapor pressure and vapor temperature each drop with evaporation, necessitating added heat for continued bubble growth [27]. This makes the bubble's growth a function of heat transfer rate [11].

Interphase heat transfer is therefore important to quantify. In the context of a fuel injector, the vapor generation process is limited in part by the available heat energy. This is expressed by Jakob number, which represents the ratio of the heat capacity of a fluid to the heat required for phase change (the latent heat of vaporization), and is definied as

$$Ja = \frac{\rho_l C_p \Delta T}{\rho_v h_{fg}} \tag{1.1}$$

with ρ representing density, subscripts l and v the liquid and vapor phases respectively, C_p the specific heat at constant pressure. The latent heat of vaporization is h_{fg}, and ΔT is the degree of superheat. When Jakob number is large, phase change occurs readily upon bubble nucleation. Low Jakob number indicates that the process is controlled by a lack of heat supply.

A small ΔT yields more potential phase change at low temperatures than the same ΔT at higher temperatures. Because vapor density and therefore latent heat of

vaporization increase with temperature, cold flows require less energy for evaporation by Eq. 1.1 [27]. In addition, at higher temperatures, phase change causes a drop in vapor temperature and consequently vapor pressure. The degree of superheat becomes essential, as the newly formed vapor drops in temperature and the bubble requires additional heat energy to continue expanding [27]; heat transfer affects low-temperature bubble growth little, where kinematic effects dominate [27], but is the crux of high temperature bubble growth.

1.2 Geometric Considerations

While a nozzle's pressure and enthalpic conditions may suggest the presence of vapor generation, physical geometric considerations have strong effects on the amount of phase change actually taking place and the flow dynamics. The length of the nozzle determines the time available for bubble nucleation and growth, while the sharpness of the inlet orifice controls the size of the vena contracta [16]. The inlet of a nozzle represents a severe contraction in the flow, and a change in pressure and velocity to fluid particles. At large pressure differences, fluid only fills the nozzle partially, as the high-velocity fluid is unable to turn the inlet corner. The space unoccupied by fluid is referred to as the vena contracta, and extends from the nozzle orifice along the wall of the injector. While the gap created by this phenomena often becomes filled with vapor, it is not actually caused by vapor generation; Numachi found a constant reduction in cross-sectional nozzle area with a given pressure differential, regardless of the degree of cavitation [43].

The output of the effective nozzle area, reduced by the vena contracta, is measured by coefficient of discharge. It is the ratio of the ideal Bernoulli mass flow rate to the actual nozzle output [12], or

$$C_d = \frac{\dot{m}_{actual}}{\dot{m}_{ideal}} = \sqrt{\frac{\frac{1}{2}\rho\bar{V}^2}{p_1 - p_2}} \tag{1.2}$$

where $\dot{m}$ is mass flow rate, $\bar{V}$ is the mass averaged velocity in the throat, P_1 is the pressure upstream of the nozzle, and P_2 is downstream pressure. As a function of C_c (the ratio of flow cross-sectional area to total nozzle cross-sectional area), the fraction of the nozzle's cross-sectional area remaining after considering the vena contracta [44],

$$C_d = C_c\sqrt{\frac{P_1 - P_v}{P_1 - P_2}} \tag{1.3}$$

where P_v is the vapor pressure. By continuity, the flow will increase in velocity due to the reduced area in the nozzle throat. This can yield the choked flow condition, where the nozzle output becomes independent of the downstream pressure. This will be explored in greater detail in the following sections. Stemming from continutity and Bernoulli's equation, Nurick [44] generated this analytical model by varying upstream and downstream pressure with nozzles of various length to diameter (L/D) ratios. Quantifying the effects of the vena contracta on output flowrate, Nurick's model summarizes the performance of round orifices in the cavitating region for water and yields accurate coefficient of discharge values for L/D ratios of 2-20 [44].

In the noncavitating region, C_D is instead dependent upon Reynolds number [35] (Fig. 1.3). By aggregating the experiments of Morgan [41], James [26], Sanderson [54], and others, Lichtarowicz [35] organized coefficient of discharge data by L/D ratio (Fig. 1.3). Within each L/D ratio and as a strict function of Reynolds number, C_D becomes essentially constant beyond a Re of 10^4. Without sufficient length for the vena contracta to reattach, L/D ratios below roughly 2 show a drop in C_D as Re increases before approaching the final constant value C_D.

The geometry of an injector potentially has strong influence on the behavior of the flow. The sharpness of the inlet corner determines the behavior of the vena contracta. When sharp, the inlet corner can potentially cause the vena contracta to extend though the nozzle exit (called hydraulic flip) [3]. In contrast, with a suffi-

ciently rounded inlet the transition from the plenum to the nozzle throat is eased such that there is essentially no vena contracta. With rounded nozzles, lower critical cavitation number is found [44], translating to larger critical pressure ratios and a small increase in flow rate [16] as compared to sharp nozzles with identical L/D ratios and pressure conditions. Many experimentalists do not document the inlet rounding of their nozzles, making comparision between sources problematic.

Further, the ratio of a nozzle's length to its diameter (L/D) can be limiting even if nozzle conditions would otherwise produce vapor. Large superheats in metastable systems yield spontatenous vapor generation given sufficient time; in short nozzles, the flow-through time may be so short that no phase change actually takes place within the nozzle. To accurately determine the effect of nozzle length on quantity of vapor generation, Fauske examined the relationship between L/D ratio and the pressures that caused choking. Under flashing conditions, Faukse [16] performed a series of nozzle tests with various L/D ratios (Fig. 1.4). Increasing L/D ratio while holding the upstream and downstream pressures constant yielded greater critical exit pressure to upstream stagnation pressure ratio. More simply, shorter nozzles choked at larger pressure differences than their longer counterparts, indicating less vapor generation under identical pressure and enthalpic conditions. Fauske's data collapsed for various inlet and outlet pressure combinations.

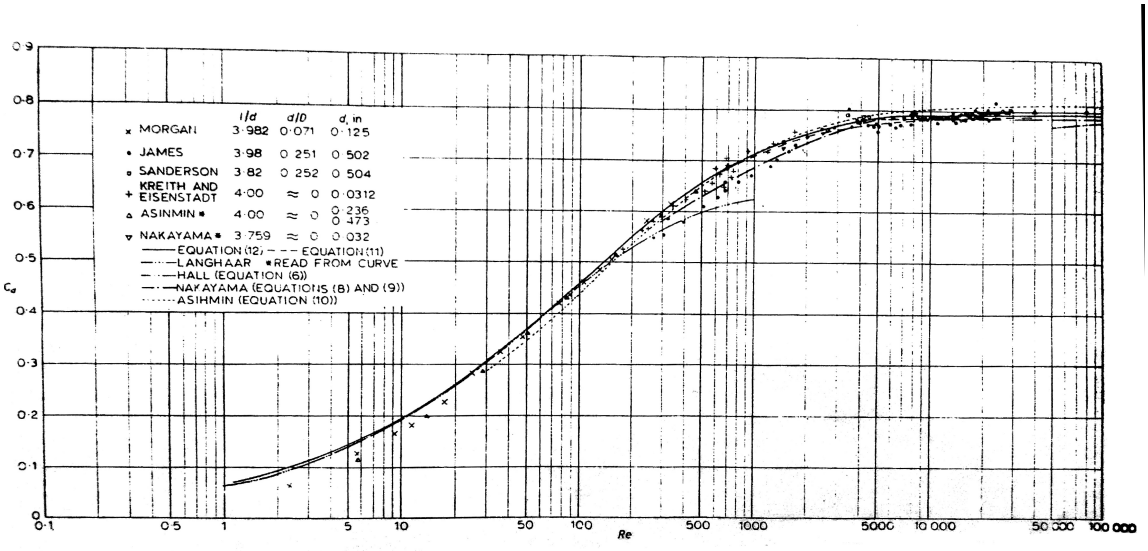

Figure 1.3: Reynolds number vs. C_D. Adapted from Lichtarowicz [35]. L/D = 4.

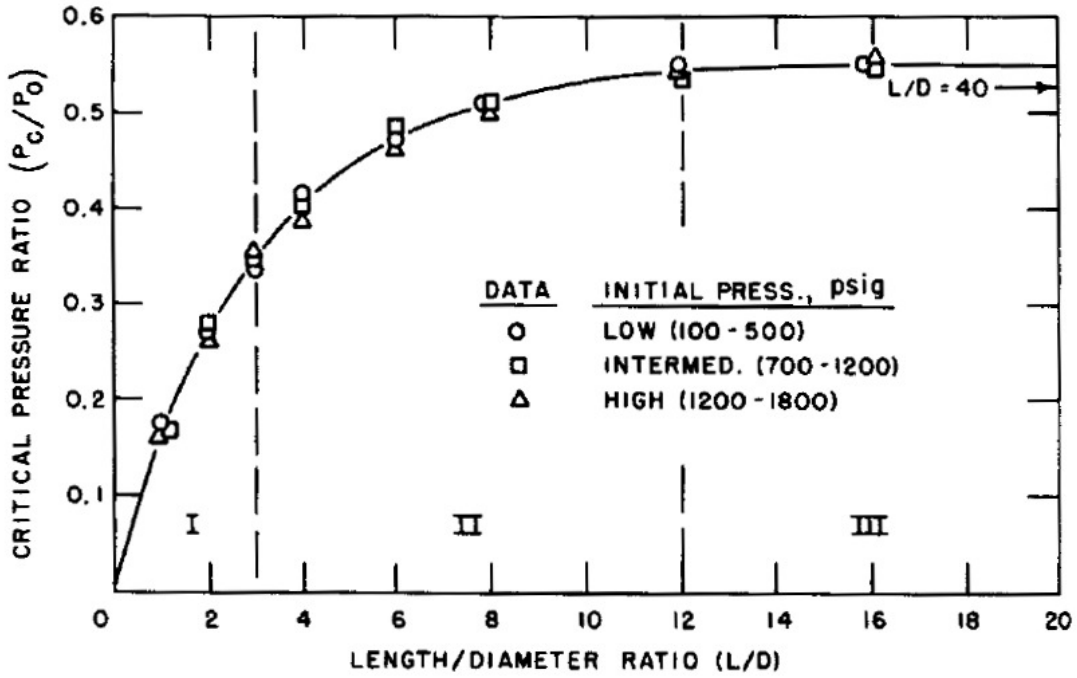

Figure 1.4: Critical pressure ratio vs. L/D ratio for 0.25 inch inner diameter tube [16].

CHAPTER 2

LITERATURE REVIEW: TWO-PHASE CRITICAL FLOW MODELING

Analytical approaches to two-phase flow vary in detail. They are seperated into those that attempt to quantify non-equilibrium phenomena and those that make simplifying assumptions to remove some complexity in modeling. The Homogenous Equilibrium Model (HEM), for example, assumes the two phases to be in complete equilibrium. More in-depth analytical approaches attempt to directly model intricate phenomena such as bubble dynamics and vapor generation. Seperated flow models are the most involved, and treat each phase as a seperate fluid with unique equations for each aspect of the two phases.

Much two-phase modeling is done in the context of critical flow. Pressure differential across a body of fluid imparts a velocity differential. The greater the pressure difference, the larger the velocity. When fluid velocity will no longer rise with decreasing downstream pressure, channel flow is considered choked, or under critical flow conditions. In general, flow rate is maximized when

$$\left(\frac{\delta G}{\delta p}\right)_S = 0 \tag{2.1}$$

where G is mass flux and p is local pressure; moreover, this path is usually thermodynamically assumed isentropic [53]. This condition is useful to find the maximum flow rate for a nozzle, pipe, or channel.

There are many industrial applications, as systems transporting fluid under pressure may exhibit choked flow conditions in the event of a break [7] [37]. Pressure

vessels and pipes can exhibit critical flow conditions, making critical flows useful to nuclear reactor power plant safety systems in measuring the rate of energy release should an accident occur [16]. During an accident, the time required for breakage to cause a reactor to become uncovered as well as the quantity of water required to cool the core post-break are essential quantities that hinge upon proper flow rate predicition [53]. The motion of refrigerant and cryogens can likewise depend upon critical flow conditions [23].

2.1 Limiting Assumption Models

2.1.1 Homogeneous Equilibrium Model

The HEM is perhaps the simplest analytical approach, and treats the flow as a single fluid. The HEM assumes velocity, pressure, and thermal equilibrium between the vapor and liquid phases. The two-phase flow is treated as a single pseudo-fluid, with thermodynamic properties calculated via equations of state or from tabulated data. This complete equilibrium assumption is most appropriate in channels of large L/D ratio, where there is sufficient time for the fluid to transition to its equilibrium state [16]. Experimentally, little difference is shown in maximum critical flowrate between channels of L/D 12 and L/D 40, indicating the validity of this assumption past L/D 12 [16] [37]. Lee and Reitz [69] used a generalized HEM model to examine transient end-of-injection nozzle phenomena in single and multihole VCO nozzles.

2.1.2 Slip Flow

Slip Flow models make a limiting assumption regarding the relative velocites of the vapor and liquid phases. Because each of the phases exhibit different densities and are not finely dispersed in one another, their velocities are likely to be different [53]. Solving for slip ratio K, defined as the ratio of mean vapor velocity to mean liquid velocity, while determining exit quality with a frozen flow or equilibrium model,

yields maximum overall flow rate [65]. Moody [40] assumed thermal equilibrium and used stagnation enthalpy to determine maximum choked flowrate, as

$$K = \left(\frac{V_{gas}}{V_{liquid}} \right)^{1/3} \tag{2.2}$$

with V representing the velocity of each phase. If instead the exit momentum flux is known, maximum flowrate occurs when [65].

$$K = \left(\frac{V_{gas}}{V_{liquid}} \right)^{1/2} \tag{2.3}$$

Fauske [17] and Moody [40] each showed that the fluid velocity of each phase does not limit the speed of the other, as previously proposed by several researchers [70].

2.2 Empirical and Two-Fluid Models

2.2.1 Frozen Flow

Frozen flow uses the assumption that quality remains constant throughout a flow. Appropriate in short nozzles where there is insufficient time for vapor nucleation, it is often paired with the assumptions of isentropic expansion, ideal gas behavior, equal average phase velocities, and a lack of heat or mass transfer between phases [23]. The model suggests no vapor formation and a strict adherence to the velocity predicted by Bernoulli's equation when the flow is initially subcooled [65].

Henry and Fauske [23] used an empirical coefficient based on the difference in HEM quality prediction at the nozzle throat and experimentally determined stagnation quality. The authors found good agreement between both HEM and frozen flow to experimental values, except that frozen flow understimated the critical pressure ratio while the HEM underestimated flowrate. Therefore, with stagnation quality above 0.10, the model resembles HEM, while very low values use the frozen flow model; moderate values blend the two approaches. Their blended model required only knowledge of upstream conditions.

2.2.2 Bubble Dynamics Modeling

Reliably predicting the rate of vapor generation in a liquid flow is central to the accuracy of flash boiling/cavitation models. In addition to an understanding of the physical phenomena taking place, quantifying the vapor generation fundamental to the development of vapor pockets and bubbles is necessary for a more complete view of two-phase fluid dynamics, especially when modeling. Bubble growth is inherently tied to pressure - after passing a critical formation radius, a bubble only grows as large as the difference between vapor pressure and far-field pressure will allow [39].

In his 1917 paper, Rayleigh [49] examines the scenario of a vapor bubble in an infinite incompressible liquid medium. Far-field pressure P_∞ and initial internal bubble pressure P_o are related to bubble radius (at a given time t) R and initial bubble radius R_o.

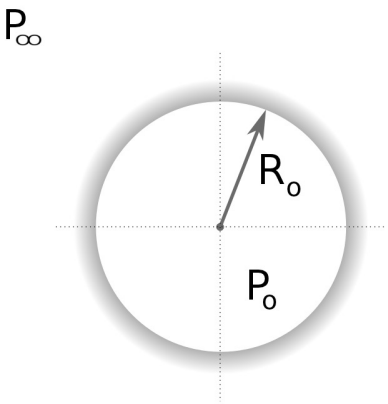

Figure 2.1: Rayleigh's Bubble Nomenclature

Beginning with the work done by the boundary of the collapsing bubble (Equation 2.4) and equating it to the kinetic energy of this collapse (Equation 2.5), a relation is derived for wall velocity vs. bubble radius with static pressures inside and outside the bubble.

$$\frac{4\pi P_\infty}{3}(R_0^3 - R^3) \tag{2.4}$$

$$\frac{1}{2}\int_R^\infty u^2 \cdot 4\pi r^2 dr = 2\pi\rho\dot{R}^2 R^3 \tag{2.5}$$

Equation 2.5 contains r, the radial location at some arbitrary length greater than the bubble radius, and u, the velocity of the surrounding fluid at that radius. The integral is performed over the range of possible r to find the work associated with the bubble's collapse. By Boyle's Law, the pressure and volume of a gas are inversely proportional when temperature and mass are held constant. Assuming that temperature change is negligible during compression, the work due to compressing the vapor bubble is subtracted from the combination of Equations 2.4 and 2.5, yielding:

$$U^2 = \frac{2P_\infty}{3\rho}\left(\frac{R_0^3}{R^3} - 1\right) - \frac{2P_o}{\rho}\frac{R_0^3}{R^3} log\frac{R_0}{R} \tag{2.6}$$

Equation 2.6 is then solved for the point at which wall velocity is zero for various combinations of far-field pressure and initial internal pressure. The pressure/radius relationship becomes more important with decreasing volume, as does the impact of pressure itself.

Plesset [47] further examined the relationship between bubble growth and pressure. To assess the growth of a vapor bubble, he combined experimentally-determined non-cavitating absolute pressure distributions known at each point on the surface of a submerged body with the general equation of motion for a spherical bubble in liquid (2.7),

$$\frac{p(R) - P(t)}{\rho} = \frac{3}{2}\dot{R}^2 + R\ddot{R} \tag{2.7}$$

where P(t) represents external pressure, P(R) is the pressure at the boundary, $\dot{R}$ is the wall velocity and $\ddot{R}$ its acceleration. Note that Rayleigh's bubble radius equation is a special case of this equation. Applying this equation to a bubble traveling along

the body correlates bubble position in space to absolute pressure in space, thereby yielding the pressure experienced by the bubble as a function of time $P(t)$. It is further stipulated that,

$$p(R) = p_v - \frac{2\sigma}{R} \tag{2.8}$$

with p_v as vapor pressure and σ as the surface tension constant. Numerically integrating the combination of Equation 2.7 and Equation 2.8 yields an equation for bubble radius as a function of time, which allows for the characterization of growth/-collapse periods. This model does not account for bubble asymmetry due to pressure gradient near the body, overestimates the wall acceleration due to the proximity of the body, and ignores boundary layer effects, but these errors are quite small [47]. Furthermore, the change in temperature associated with bubble formulation/collapse is small under cold conditions, and is likewise neglected [47]. However, the product of bubble pressure and volume is non-trivial and can rise during collapse and slow wall velocity [47]. Despite these caveats, it is clear that there is a delay time between a change in pressure experienced by a vapor bubble and the corresponding change in radius (see Figure 2.2); vapor formation is a finite rate process.

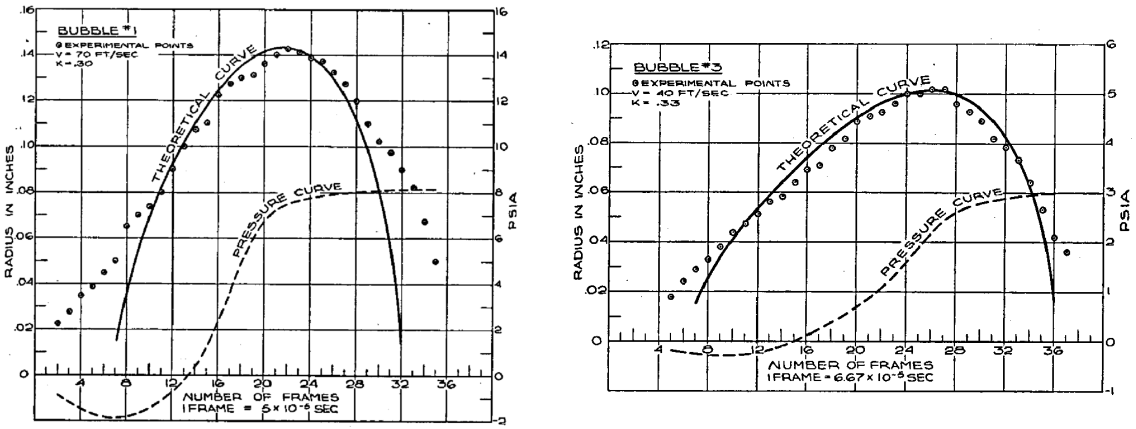

Figure 2.2: Bubble growth in response to pressure. Note the latency associated with change in radius.

Kubota et al.[31] extended Rayleigh's model to predict mean bubble radius in cloud cavitation. Attached sheet cavitation, critical to nozzle flows, can become unsteady, and produce boundary layer seperation. The resulting separated shear layer can roll up, creating a vortex that is advected with the flow. The vortex contains a low pressure region at its center, producing a cavitation cloud that can be assumed locally homogenous in bubble number density and bubble radius. Using a finite differencing scheme, Kubota et al.[31] modeled two-phase bubbly flow about a hydrofoil to investigate these phenomena, including sub-grid-scale bubble interaction in their model. Their model sucessfully predicted sheet and cloud cavitation structures as compared to experimental data.

2.2.3 Homogenous Relaxation Model

The Homogenous Relaxation Model is an extension of HEM. In addition to conservation of mass, momentum, and energy, HRM includes a differential equation describing the rate at which local dryness fraction x returns to equilibrium,

$$\frac{Dx}{Dt} = \frac{x - \bar{x}}{\theta} \tag{2.9}$$

where $\bar{x}$ is the unconstrained-equilibrium dryness fraction. In the limit of $\theta = 0$, the HRM acts like HEM, with an instantaneous return to equilibrium conditions. When θ approaches ∞, the quality will not change, as in frozen flow. This linear, one-dimensional approximation of the finite rate phase change process makes the HRM adept at capturing dispersion and wave dissipation effects more easily than two-fluid models[15]. Dispersion markedly affects the primary flow mechanics, and is caused by the non-equilibrium of the two phases, making quantification of this process extremely important in the correct prediction of void fraction, pressure, and velocity distribution [4] [15]. Two-fluid models are able to do this, but at high computational cost.

Relaxation models have had success in chemical reaction gas dynamics, motivating their experimentally-validated use in two-phase flow [4].

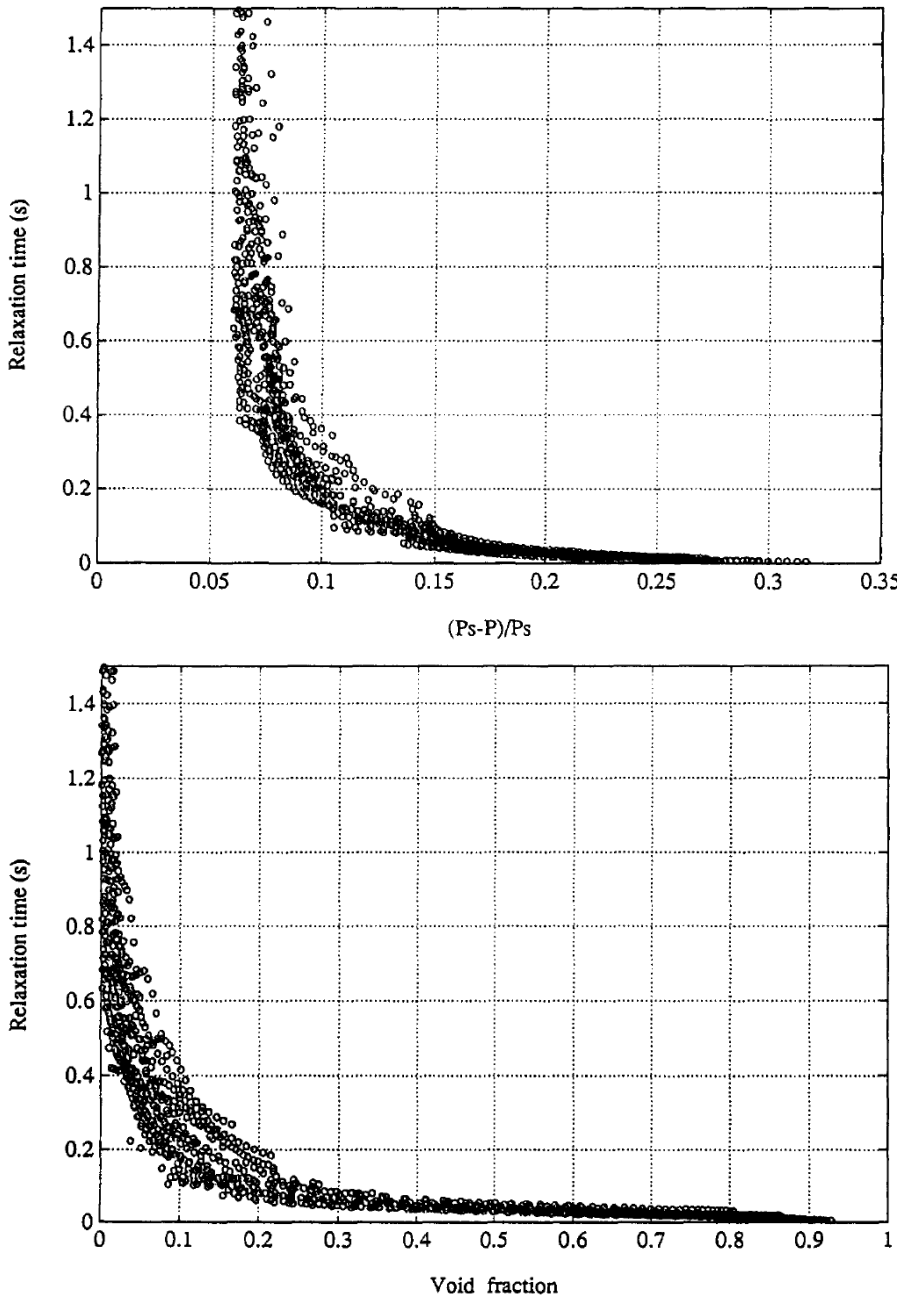

Figure 2.3: Relaxation time as a function of relative pressure drop and void fraction. Relaxation time rapidly approaches zero as either pressure drop or void fraction increases. Ps here is saturated pressure. Adapted from [15]

Prediction of the vapor generation rate determines the character of HRM, as in Equation 4.1. However, it is dependant upon local relaxation time, which is very difficult to measure. Instead, analyzing the experimental void fraction and pressure distribution measurements of Reocreux [52], relaxation time is a strictly decreasing monotonic function of void fraction and non-dimensional pressure difference with an exponential tendency toward equilibrium conditions [15], as

$$\Theta = \Theta_0 \epsilon^{-0.54} \varphi^{-1.76} \tag{2.10}$$

where $\Theta_0 = 3.84 \times 10^{-7}$ seconds, ϵ is void fraction, and φ is the non-dimensional pressure difference, computed as

$$\varphi = \left[\frac{P_{sat}(T_{in}) - P}{P_{critical} - P(T_{in})} \right] \tag{2.11}$$

Schmidt [56] examined diesel injector nozzles using both the HEM and HRM. Through short nozzles running fluid below superheat values of 10^oC, comparison to the experimental results of Reitz [51] showed good agreement using the thermodynamic equilibrium assumption. As temperature increased and the vapor pressure became greater than the downstream pressure, the flow rate values predicted by the numerical model diverged from the experimental. The homogenous pressure assumption did not allow for pressures lower than the vapor pressure that were found in the nozzle throat. In reality, the lower pressures yield additional fluid acceleration, a non-equilibrium phenomenon outside the scope of the HEM.

Neerokar et al. [42] simulated both non-cavitating and cavitating conditions in 3D using the HRM. A modeled diesel surrogate was used as the working fluid, with thermodynamic properties interpolated from a lookup table. Comparison to the experiments of Winklhofer et al. [68] was favorable for discharge coefficient under vapor-lock conditions, but showed that the model overpredicted near-wall vapor velocity.

2.2.4 Two-Fluid Models

Separated flow models, also known as Two-Fluid models, use separate equations for the mass, momentum, and energy conservation of the vapor and liquid phases. Two-fluid models seek to reproduce the mechanics underlying flow phenomena rather than emulate their observable effects, in contrast to bubble dynamics models or flow regime catagorizations. In this way, these models attempt to remove the application-specific nature of models that require significant limiting assumptions, either in part [53] or almost completely [7]. This leads to large, complex models, able to solve many different flow conditions at the expense of heavily increased computational cost.

Richter [53] utilized a one-dimensional separated flow model, emphasizing the hydrodynamic and thermal non-equilibrium pertnient to two-phase critical flow. While unique conservation equations were used for the two phases, initial bubble density and bubble diameter were empirically assumed, in line with the experiments of Reocreux [52]. Bubble flow regimes were characterized by void fraction. The bubble regime, dominated by thermal non-equilibrium, was found to exist until vapor generation yielded a vapor fraction α of 0.3. The churn-turbulent zone, characterized by bubble coalescence, yielded decreasing interfacial area and increasing vapor velocity to liquid velocity ratio. A return to thermal equilibrium and the onset of velocity non-equilibrium was also evident. This gave way to the annular flow regime at a void fraction α of 0.8 [53], where choking flow yielded unequal velocity and temperature.

Minato et al [37] focused on two-dimensional two-phase pipe flow from a vessel to evaluate the effects of multi-dimensional flow on critical discharge rate and compare 1D and 2D calculations. Their model reproduced choked flow conditions, and emphasized the importance of pipe inlet geometry. The model gave physical results, prediciting a liquid core surrounded by heavily gaseous two-phase fluid. Their two-dimensional calculations produced very similar results to their one-dimensional results when inlet velocity was uniform. A relatively steady-state region between the pipe

inlet and exit was found beyond a L/D ratio of 1, but was no longer found at a L/D of $\frac{1}{3}$.

Boure [7] examined the classical model of Vernier and Delhaye [63] and Boure and Reocreux [8], which utilized transfer terms in the conservation equations assumed to be functions of only space, time and dependant flow variables [7]. For two-phase flow, the model returned identical results for critical flow rate and the rate of small disturbance propogation, yielding erroneous results. Boure generalized these equations, implimenting partial derivatives of the dependant variables, allowing better coupling between phases. Friction and heat transfer relations based only on dependant flow variables were used for closure, while interfacial drag was determined by flow regieme. His critical flow criterion was determined by setting the determinant of the set of conservation and closure equations equal to zero under stady state flow conditions [7]. The resulting model was properly non-reactive to increasing pressure difference beyond the threshold required for choked flow.

2.2.5 Modern Modelers

Modern cavitation models tend to incorporate various effects in addition to cavitation itself. Formation and transport of vapor bubbles, the effects of turbulence on the pressure and velocity field, and the presence of dissolved non-condensible gasses and their implications are described by the Full Cavitation Model [57]. Validated against high-speed flow over a hydrofoil and cylindrical bodies, Singhal used the Rayleigh-Plesset equation and a homogenous flow approach. Empirically tuned model constants handled vapor generation and condensation. Their efforts produced a robust and accurate model for high speed cavitating flows.

Other models incorporate heating effects. The variable density, viscosity, heat capacity, and thermal conductivity that stem from high heat and pressure dramatically affect the volumetric efficiency of an injector. Theodorakakos et al [61] found

significant change in coefficient of discharge when compressibility and variation of fuel properties were considered, as compared to constant property simulations. Using a parcel-based Lagrangian cavitation bubble model with a RANS CFD model, they simulated high temperature and pressure flow through both sharp edged and round tapered nozzles. Stochastic Monte Carlo approximation modeled the physical processes experienced by the bubbles, with growth and collapse handled with the Rayleigh-Plesset equation. Viscous heating was quantified with an energy equation paired with the variable fuel properties. Dramatic changes in volumetric efficiency were found due to the heating from wall friction and variable fuel processes.

With the goal of decreasing injection-to-injection and hole-to-hole variation in multi-hole injectors, Mitroglou et al [38] coupled transparent real-scale nozzle experimental results with CFD analysis. Experimentally observed string cavitation was controlled through geometric design considerations yielding stable spray patterns at the nozzle exit in resulting simulations. These led to controlled levels of spray atomization with constant cavitation number but varying needle lift.

The stability of steady-state quasi-1D bubbly cavitating nozzle flow are explored through bubble radius and flow speed evolution equations by Pasinlioglu [46]. After perturbing these evolution equations, normal mode analysis of varying inlet conditions show their model as stable for only very low wave numbers. All damping mechanisms were lumped into viscous dissipation with a sole damping coefficient with a polytropic law for bubble formation and collapse. They found increased stability when wall shear stress was included.

CHAPTER 3

PRELIMINARY WORK: VALIDATION CASES

To examine the current state of HRMFoam's predicitive accuracy, four sets of experimental results have been modeled. These include comparisons to: high temperature cases, with increased vapor generation; large diameter nozzles with much lower velocities than diesel injection simulations; a geometry with a large degree of inlet rounding, and subsequently increased coefficient of discharge; and finally, a set of cases that collapse across various working fluids to provide a general benchmark for coefficient of discharge.

3.1 Elevated Temperature

To assess the preliminary performance of the model at elevated temperature (prior to the validated use of an energy transport equation), HRMFoam was run with settings mirroring the 1990 work of Reitz [51]. Reitz examined the high-speed nozzle flow of water under flashing conditions, from 300K up to the saturation temperature at his experimental pressure, 432K. In simulation, enthalpy values of 364E3 J/kg (367K) through 645E3 J/kg (426K) were used to meet these conditions. The nozzle was considered adiabadic and the flow laminar to isolate the effects of the model. The physical geometry was a broader channel of 1.58mm diameter that contracted to an L/D ratio 4 nozzle with a diameter of 0.34 mm.

The geometry was assumed axisymmetric for meshing purposes, and as such a 5° slice of the round injector was considered representative when paired with wedge boundary conditions on the front and back faces. This wedge was meshed with 33,000

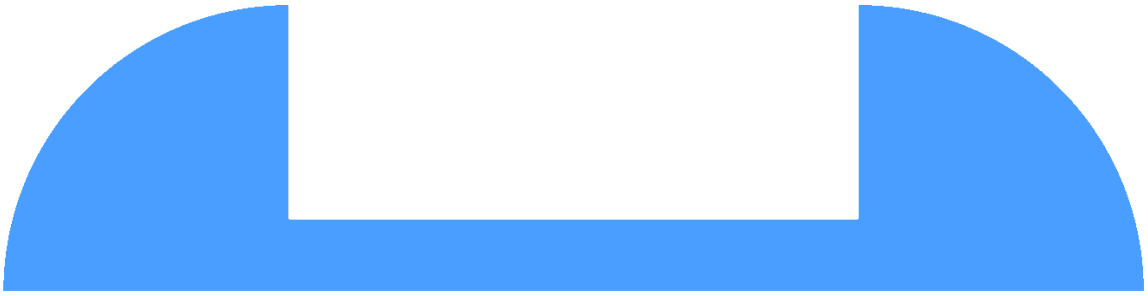

Figure 3.1: Computational Mesh used in Reitz simulations. L/D = 4, 33,000 cells. Flow is from left to right.

cells, as in Figure 3.1, with 78 cells across the throat diameter (Figure 3.2). The inlet was very slightly rounded with an inlet radius to diameter ratio of 0.0125, to approximate realistic injector manufacturing processes that do not generate a perfectly sharp inlet corner.

Reitz's experiments produced measurements of mass flow rate and temperature. Flash boiling decreases volumetric flow rate, and as temperature increases, the effect becomes more pronounced (Figure 3.3). As the injection temperature becomes very close to the fluid vapor temperature, the flow rate drops sharply as the entering fluid becomes predominantly gas. HRMFoam was able to reproduce the experimental trend, within 2.55% of the experimental flow rate on average (Figure 3.4) in the evaluated temperature range. Increasing temperature yielded more divergent results, as vapor production rate and condensation rate became more critical to the calculated flow rate.

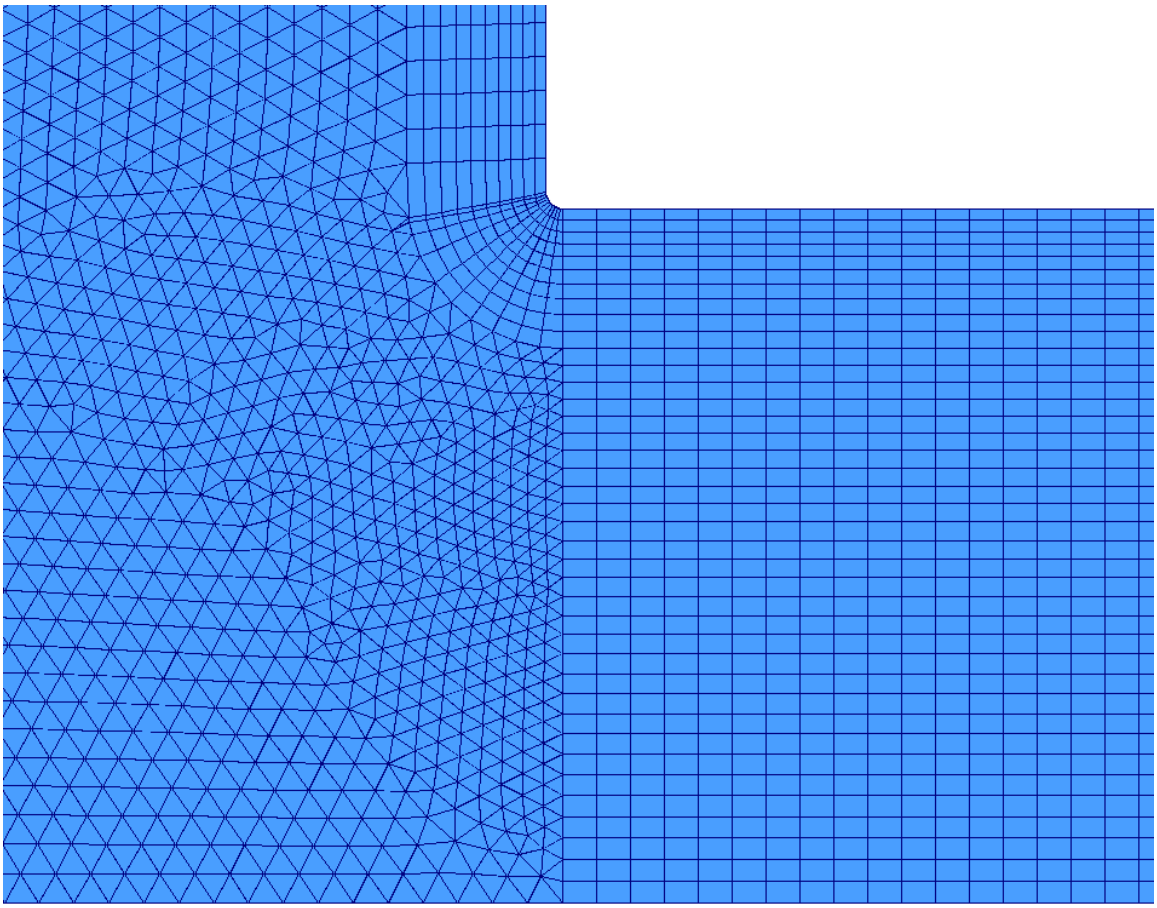

Figure 3.2: Closeup of computational mesh used in Reitz simulations, inlet corner.

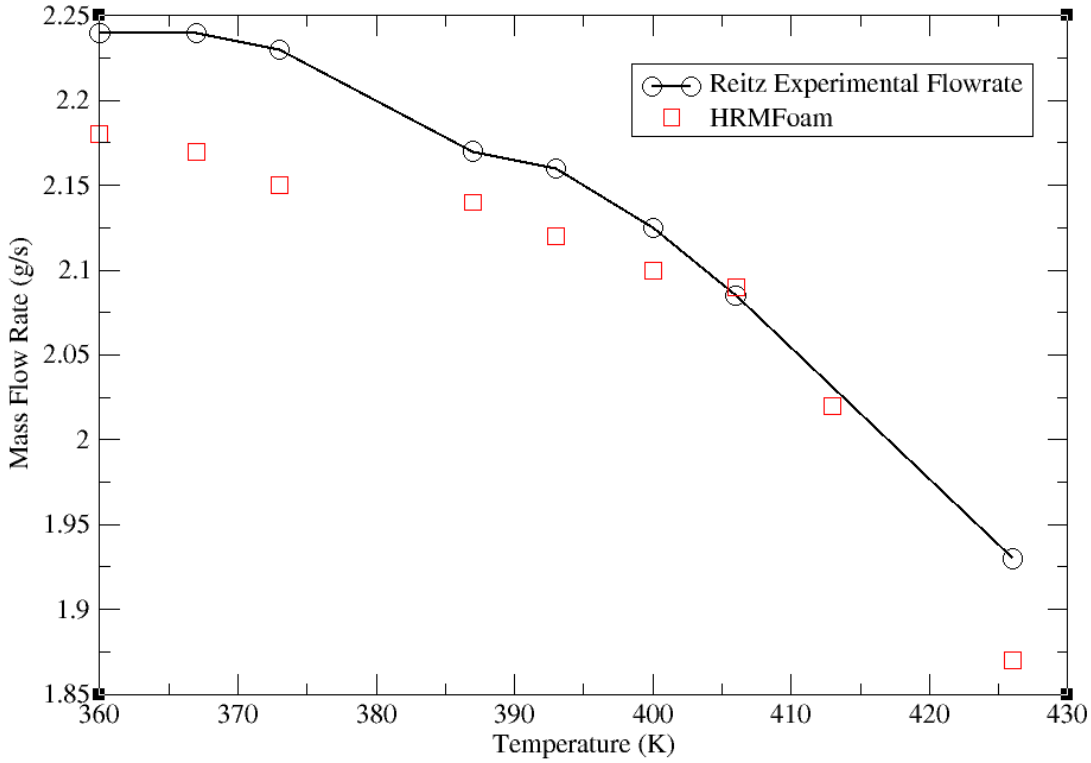

Figure 3.3: Reitz's [51] experiments and HRMFoam. Error rises rapidly very close to the fluid's saturated temperature.

Temperature (K)	Experimental Flow Rate (g/s)	Simulation Flow Rate	% Error
360	2.24	2.18	-2.77
367	2.24	2.17	-3.10
373	2.13	2.15	1.35
387	2.16	2.14	-0.94
393	2.15	2.12	-1.01
400	2.15	2.10	-2.24
406	2.07	2.09	0.90
413	2.04	2.02	-0.93
426	1.93	1.87	-3.04

Figure 3.4: Comparison of simulation results to experimental data of Reitz [51].

3.2 Low Velocity Flow

For pressure-driven nozzle flow, coefficient of discharge is a monotonically increasing function of Reynolds number. Given the Reynolds Number of a room temperature water flow, a prediction of coefficient of discharge can be made using the compiled experimental data of Morgan [41] and James [26]. Lichtarowicz [35] organized the work of these and other experimentalists into a series of plots separated by length to diameter ratio; the plot shown in Figure 3.6 contains Lichtarowicz' compiled data for nozzles of L/D ratio 4, and presents data from nozzles ranging in size from 0.032 inches to 0.504 inches. These large diameters (relative to real-scale diesel injectors) translate to extremely low fluid velocities, especially at low Reynolds number.

A number of HRMFoam cases were run under the experimental conditions of Morgan and James, with three sets of settings. The Re 32, 71, and 9945 cases (see Figure 3.5) matched Reynolds number but not physical size. Simulation fluid velocities were closer to diesel injection velocities in these cases. The Re 5, 14, and 112 cases use Morgan's experimental nozzle diameter of 0.125 inches and retain the very low experimental velocity, and the Re 632 case utilizes James' nozzle diameter of 0.502 inches. All cases utilized the mesh from the preceding Reitz validation.

Reynolds Number	D (m)	C_D (Expected)	C_D (Simulation)	% Error
5	3.18E-003	0.14	0.282	-50.35
14	3.18E-003	0.23	0.296	-22.29
32	1.00E-005	0.31	0.323	-4.16
71	4.72E-006	0.42	0.408	3.06
112	3.18E-003	0.46	0.466	-1.39
632	1.28E-002	0.68	0.665	2.26
9945	4.72E-006	0.80	0.72	10.00

Figure 3.5: HRMFoam low velocity flow results, by Reynolds Number.

HRMFoam's coefficient of discharge predictions are overlaid with Lichtarowicz's data in Figure 3.6. All of the runs were again assumed laminar. HRMFoam predicted coefficient of discharge in these cases with up to 1.4% accuracy (Figure 3.5). Prediction error was small for Re = 32-632, but increased dramatically at lower Reynolds

number, in the region of Re = 2.3-14. This is to be expected at very low Reynolds number, as creep flow depends heavily upon the diffusion terms of Navier-Stokes, and HRMFoam's PISO algorithm assumes advection-dominant flow. For Reynolds numbers above roughly 5000, Lichtarowicz's data show an asymptotal approach to a C_D of 0.8, which HRMFoam underpredicts by roughly 10%. HRMFoam does, however, predict the behavior of the experimental curve at very low and very high Reynolds numbers.

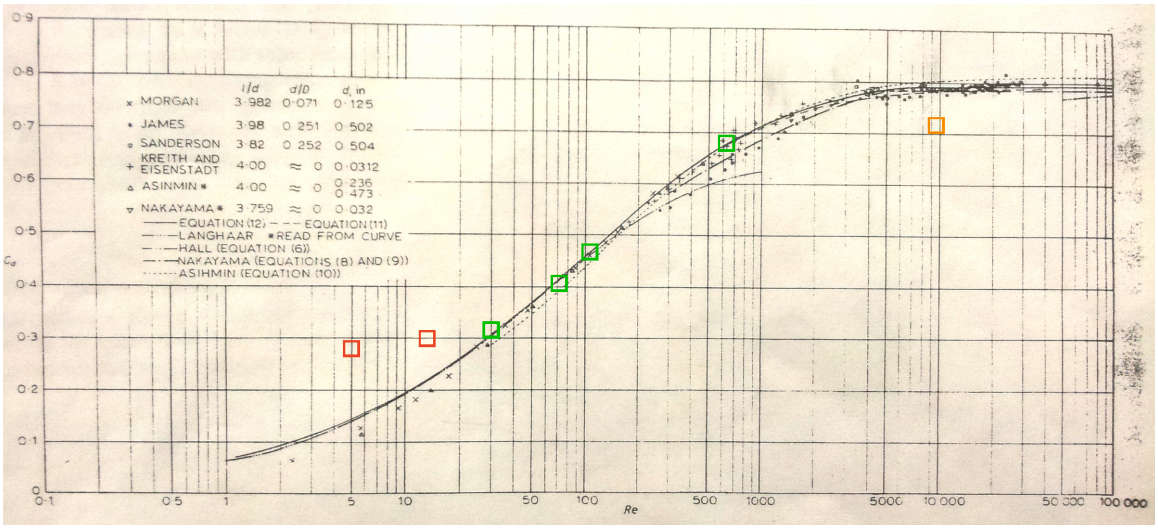

Figure 3.6: Lichtarowicz's compiled experimental results [35]. HRMFoam results shown as squares, color coded by percent error; See Figure 3.5. Figure from Lichtarowicz [35].

3.3 Inlet Rounding

As previously discussed, the degree of rounding applied to a nozzle's inlet orifice can strongly influence its overall mass flow rate and velocity profile. Increased rounding eases the transition from plenum to nozzle throat, and allows the flow to fill more of the channel. This translates to increased coefficient of discharge as rounding becomes more pronounced [55] (Figure 3.7).

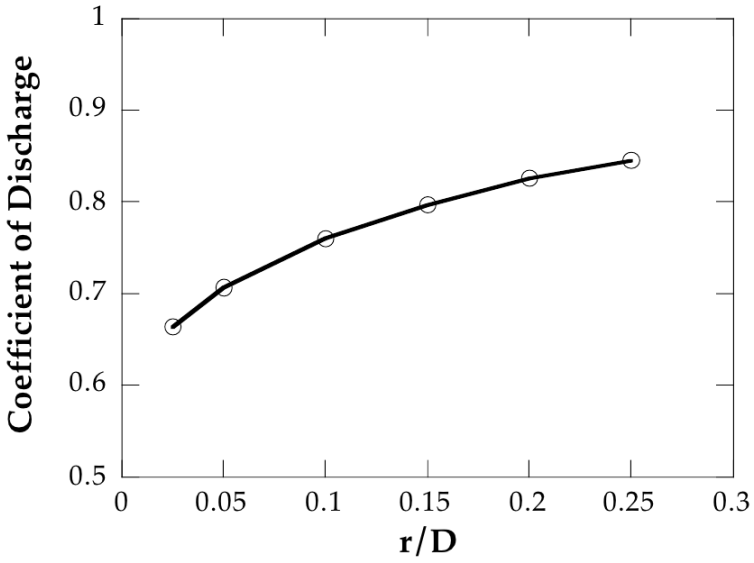

Figure 3.7: Inlet rounding's effects on coefficient of discharge. Increasing rounding smooths the flow and increases C_D. Figure from Schmidt [55].

HRMFoam was used to reproduce the coefficient of discharge data for Torres' [62] two-stage nozzles. Torres conducted tests using two upstream pressures, 10 MPa and 20 MPa, with nozzles that exhibited a high degree of inlet rounding and little-to-no vena contracta region in the throat. Varying the pressures downstream of the nozzles led to a range of flow rate data, shown in Figure 3.8 [62]; the plateau in flow rates with increasing pressure difference indicates the onset of choked flow.

The injector geometry (Figure 3.9) was meshed as a 5° wedge as in the preceding Reitz validation, with roughly 16,000 cells. The inlet orifice was rounded with an

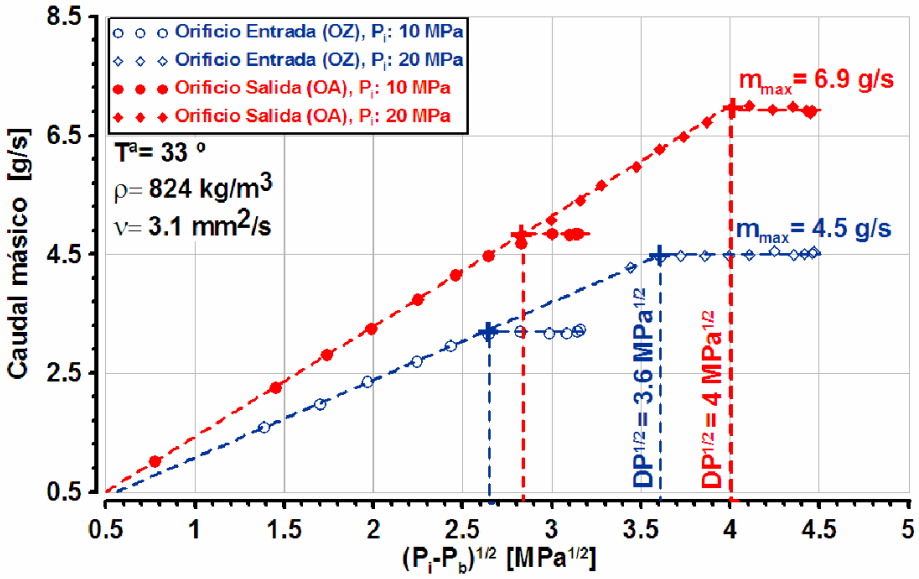

Figure 3.8: Torres' raw flow rate data. Cases are organized by upstream pressure. Figure from Torres [62].

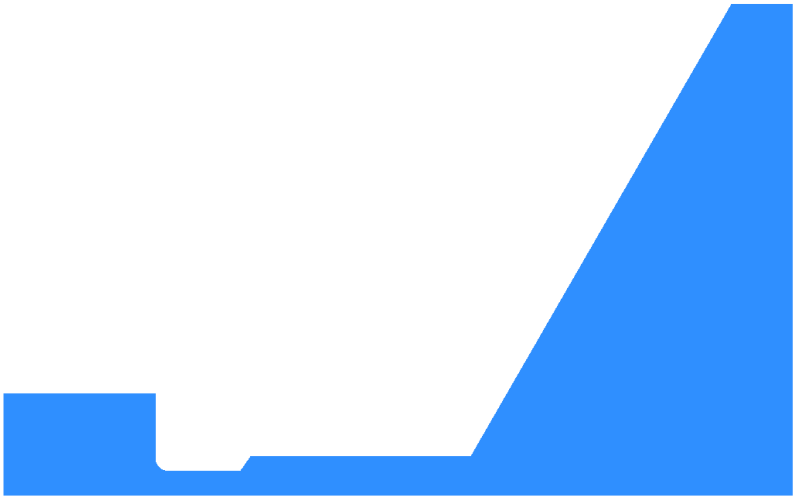

Figure 3.9: Mesh used for Torres validation cases. Flow is from left to right; note two-stage nozzle. Mesh includes 16,000 cells.

inlet radius to diameter ratio of 0.25, with 20 cells across the throat and 40 across wider second stage diameter.

With this high level of rounding, HRMFoam was able to very accurately reproduce the results of Torres' cases in the cavitating region. For Torres' 10 MPa upstream

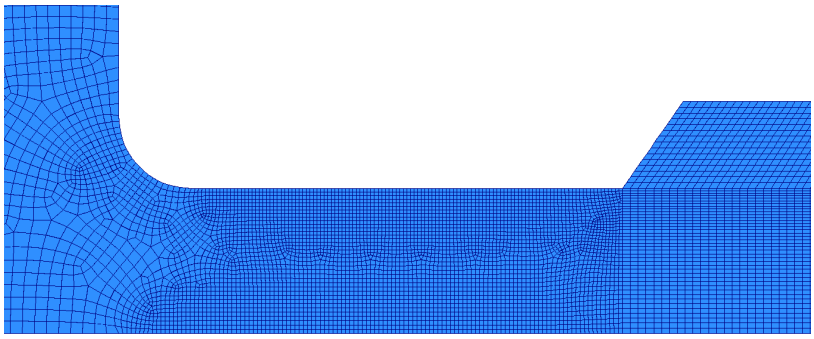

Figure 3.10: Closeup of mesh used for Torres validation cases.

pressure cases, HRMFoam was accurate to within 0.53% of the experimental coefficient of discharge (Figure 3.11); for the 20 MPa cases, within 0.46% (Figure 3.13). Beyond K values of 1.7 (roughly the onset of the non-cavitating region), predicted mass flow rates exceeded their Bernoulli-equation-calculated counterparts, surely a non-physical result. Those results are regarded here as outliers. The coefficent of discharge data is tabulated in Figures 3.12 and 3.14.

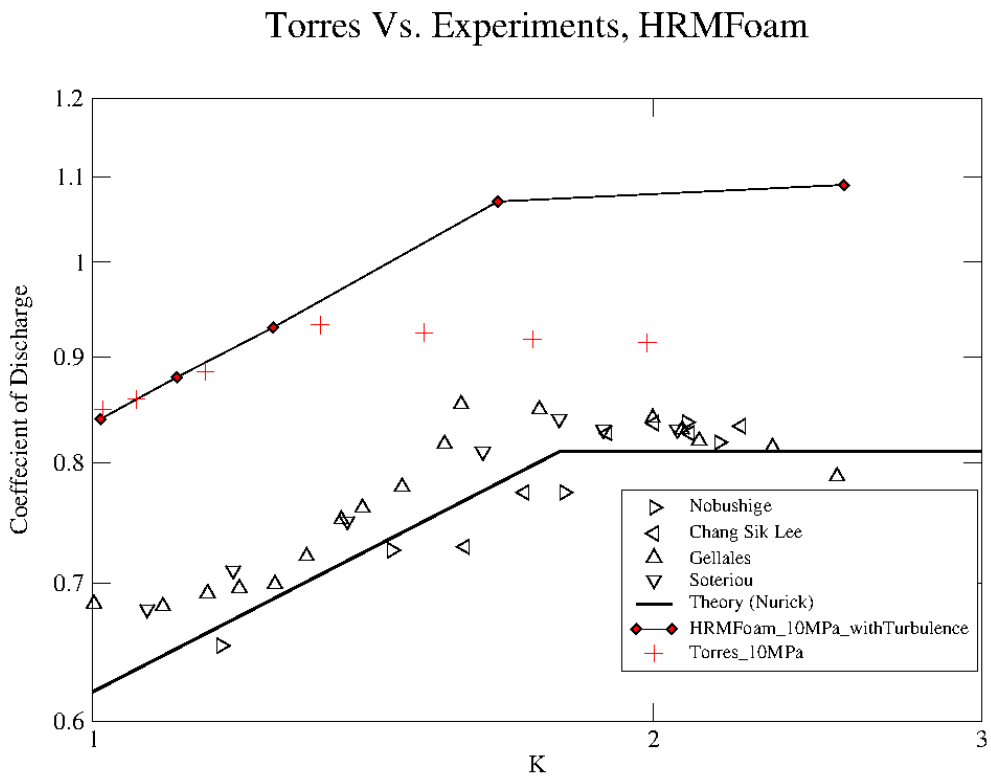

Figure 3.11: Comparison between various experimentalists [33, 60, 21, 58], Nurick's theory line[44], Torres' 10 MPa nozzle experiments [62], and HRMFoam.

K	Downstream Pressure (MPa)	Experimental C_D	Simulation C_D	% Error
1.01	0.08	0.847	0.841	-0.770
1.11	0.98	0.875	0.878	0.439
1.25	2.20	0.912	0.931	2.011
1.65	3.94	0.918	1.07	15.159
2.53	6.05	n/a	1.09	n/a
			Average Error	4.210

Figure 3.12: HRMFoam tabulated data, as compared to the data of Torres [62] at 10 MPa.

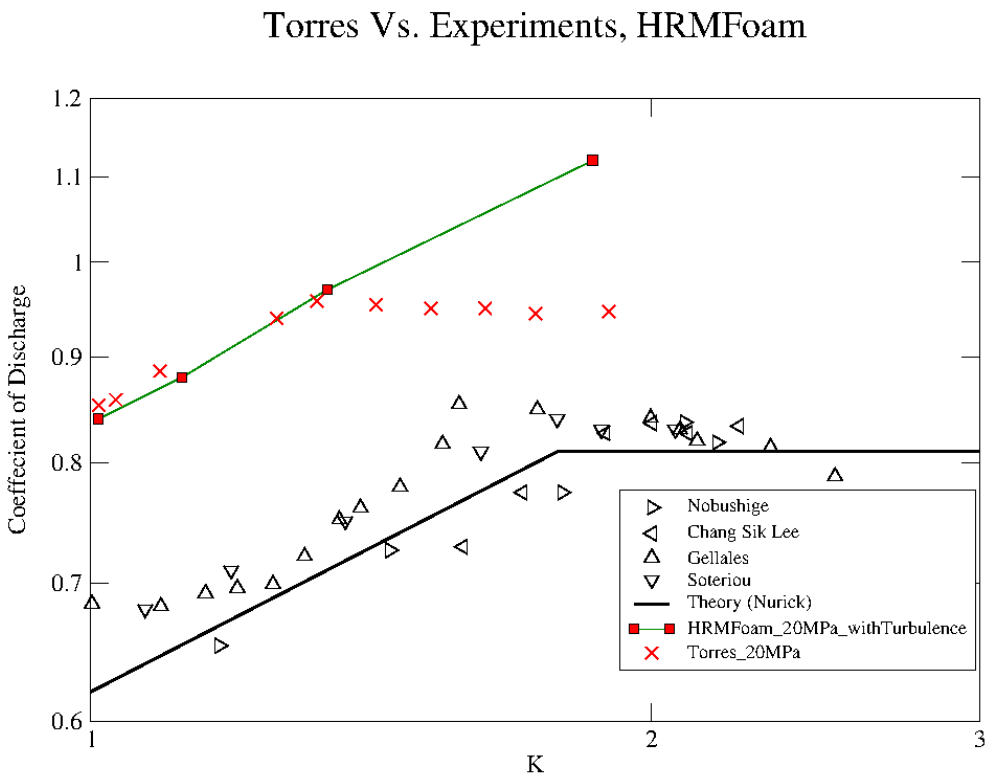

Figure 3.13: Comparison between various experimentalists [33, 60, 21, 58], Nurick's theory line[44], Torres'20 MPa nozzle experiments [62], and HRMFoam.

K	Downstream Pressure (MPa)	Experimental C_D	Simulation C_D	% Error
1.01	0.14	0.854	0.842	-1.446
1.12	0.10	0.891	0.886	-0.646
1.34	5.07	0.966	0.973	0.770
1.86	9.25	0.945	1.12	17.543
			Average Error	4.055

Figure 3.14: HRMFoam tabulated data, as compared to the data of Torres [62] at 20 MPa.

3.4 Coefficient of Discharge Benchmark Comparison

Coefficient of discharge C_D is positively correlated with pressure ratio K in the cavitating region. Nurick proposed a model that collapsed a great deal of experimental nozzle output flow rate data based on his experimental observations using sharp-edged nozzles and water. As the reduction in cross-sectional area is dependent only upon pressure ratio K, this relation holds for various temperatures and working fluids with a given L/D ratio [44]. Figure 3.15 is a compilation [12] [56] of experimental data points from various experimentalists plotted with the Nurick model (labeled "Theory").

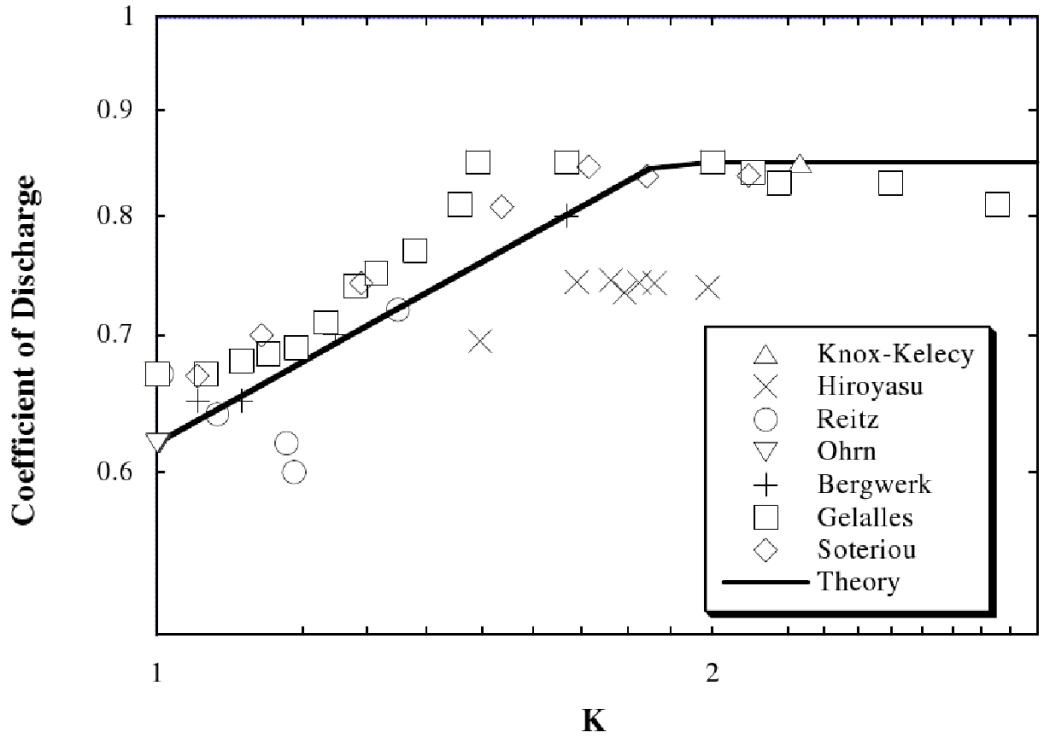

Figure 3.15: Nurick Theory vs. Experiments. Data are plotted on log-log axes from [44, 30, 24, 50, 45, 3, 21, 58]. Figure from [12, 56].

Because much data exist to confirm the accuracy of Nurick's theory [44, 30, 24, 50, 45, 3, 21, 58], Nurick's coefficient of discharge predictions have been used as a quality metric in the present work. HRMFoam's predictions are compared with Nurick's

theory below (Figure 4.2), with simulations conducted using a diesel fuel surrogate at room temperature. The data show reasonable agreement in the cavitating region but diverges from the theory at higher K values, averaging 8.02% error across the curve (Figure 3.17). This error forms the basis for the parameter tuning study to follow.

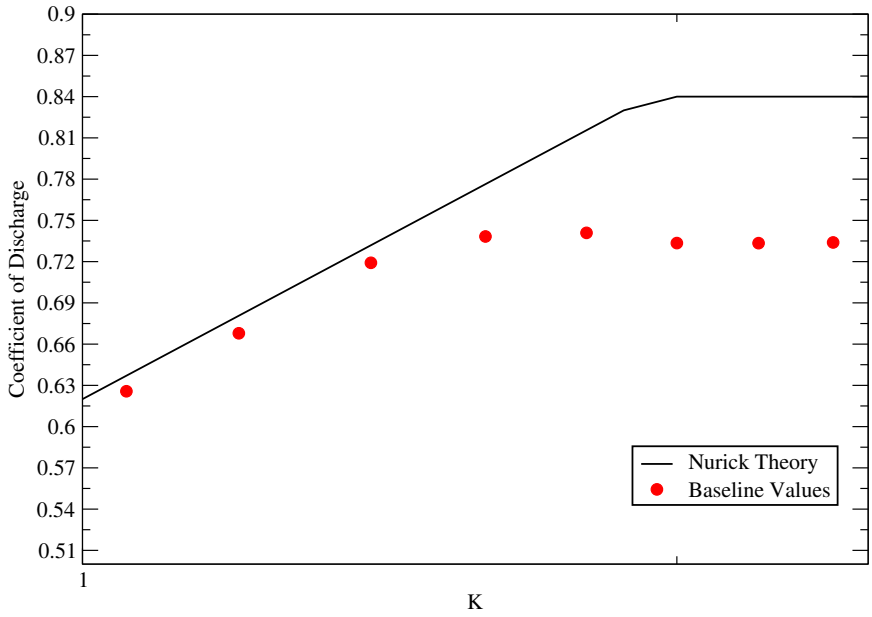

Figure 3.16: State of system before optimization.

K	Nurick C_D	Simulation C_D	% Error
1.05	0.640	0.626	2.23
1.20	0.700	0.668	4.59
1.40	0.745	0.719	3.47
1.60	0.805	0.738	8.29
1.80	0.830	0.741	10.74
2.00	0.830	0.734	11.63
2.20	0.830	0.733	11.63
2.40	0.830	0.734	11.57
		Average Error	8.02

Figure 3.17: Tabulated C_D vs. K for comparison of HRMFoam to Nurick [44].

CHAPTER 4

PRELIMINARY WORK: PARAMETER TUNING STUDY

In addition to HEM's conservation of mass, momentum, and energy, HRM includes a differential equation describing the rate at which local dryness fraction x (the ratio of vapor to liquid in a cell) returns to equilibrium;

$$\frac{Dx}{Dt} = \frac{x - \bar{x}}{\Theta} \tag{4.1}$$

where $\bar{x}$ is the unconstrained-equilibrium dryness fraction and Θ is the relaxation time. As Θ approaches 0, the HRM acts like HEM, with an instantaneous return to equilibrium conditions. As Θ becomes large, the quality will not change, as in frozen flow.

The behavior of the vapor generation rate is central to HRMFoam, as in Equation 4.1. Local relaxation time determines this vapor generation rate, and is difficult to measure directly. The void fraction and pressure distribution measurements conducted by Reocreux [52] provide an experimentally derived expression for the relaxation time Θ, as presented by Downar-Zapolski [15]:

$$\Theta = \Theta_0 \epsilon^{-0.54} \varphi^{-1.76} \tag{4.2}$$

where $\Theta_0 = 3.84 \times 10^{-7}$ seconds, ϵ is void fraction, and φ is the non-dimensional pressure difference, computed as

$$\varphi = \left[\frac{P_{sat}(T_{in}) - P}{P_{critical} - P(T_{in})} \right] \tag{4.3}$$

Together, these equations yield relaxation time as a strictly decreasing monotonic function of void fraction and non-dimensional pressure difference with an exponential tendency toward equilibrium conditions. Relaxation time, and subsequently vapor generation rate, is governed by three parameters: the time factor Θ_0, the exponent of the void fraction ϵ, and the exponent of non-dimensional pressure difference φ. These are referred to in the following as Theta0, VoidFrac, and pNonDimPress. For Downar-Zapolski's analysis of Reocreux's raw data, see Figure 2.3 in Chapter 2. Physically, Theta0 cannot be negative, as it is a time in seconds. VoidFrac and PNonDimPress are each negative. Increasing VoidFrac translates to greater vapor surface area, which yields greater heat transfer rate and smaller relaxation time, hence its negative exponent. PNonDimPress accounts for the decrease in relaxation time when the pressure difference is such that phase change occurs.

Originally calculated for water in Reocreux's work [52], the parameter values derived are not appropriate for cavitating diesel fuel. They provide the starting point to optimize the system parameters for the diesel surrogate used in the present work. While the differences in coefficient of discharge are not seemingly large, this error propagates as temperature increases. Moreover, when compounded by uncertainty in geometry measurements, working fluid surrogate density error, turbulence modeling, mesh resolution effects, and more, it becomes imperative to accurately quantify what *can* be accurately quantified.

Methodology

Computational Approach

Ideal parameter values would yield accurate results throughout the range of pressure ratios. As such, seven different pressure set-ups were used, evenly distributed throughout the K domain (Figure 4.1). All were set to enthalpy values corresponding to a temperature of 306K, to ensure cavitating (not flash boiling) conditions.

For expediency's sake, only the four lowest K values (K1.05, K1.2, K1.4, K1.6) were updated and perturbed at each step.

K	Upstream Pressure (MPa)	Downstream Pressure (MPa)
1.05	10	0.50
1.20	10	1.67
1.40	10	2.86
1.60	10	3.75
1.80	10	4.44
2.00	10	5.00
2.20	10	5.45
2.40	10	5.83

Figure 4.1: Pressure values for parametric study, by case. Upstream pressure held constant, downstream pressure adjusted by case.

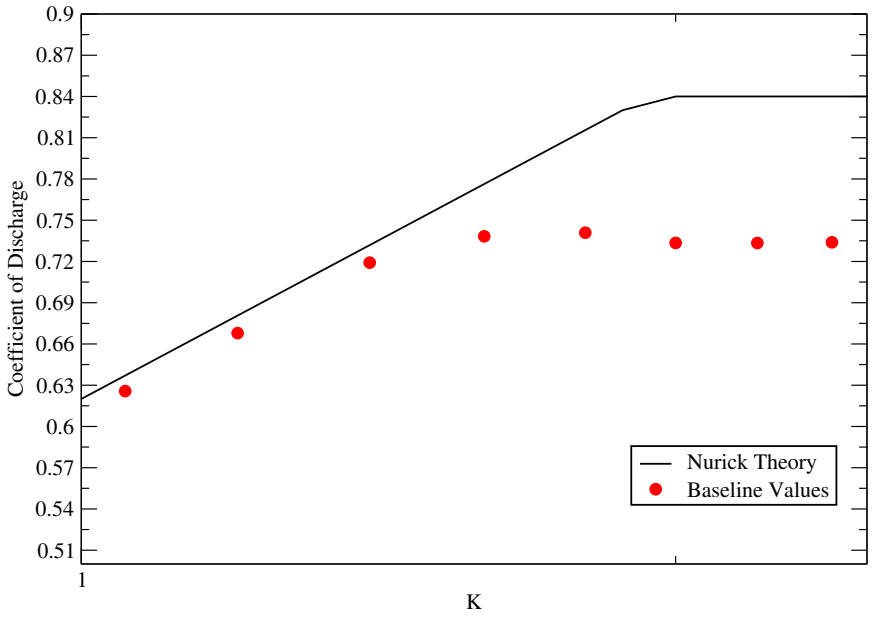

Figure 4.2: State of system before optimization.

The remaining K value cases were then updated with the new parameters, and their residuals examined. This was done with the knowledge that vapor generation rate affects cavitating cases (those below K = 1.7) much more heavily than non-cavitating cases. Error from K = 1.7 to K = 3 is equally likely to be due to a number

of other factors, not limited to viscosity, density, wall roughness, and Reynolds number effects such as turbulence. For the massive decrease in computational cost, there is little error introduced by this assumption. The initial coefficient of discharge values, obtained with the original water-derived vapor equation parameters, can be seen in Figure 4.2.

Seven 14-hour simulations were conducted for the initial baseline values, three simulations to test the domain limits, twelve for the initial gradient calculation, sixteen for the first Hooke-Jeeves step, sixteen for the second Hooke-Jeeves step, and finally four to examine the larger K values with the final parameters in place. The 59 simulations necessary were conducted on the Mach, Swordfish, and Puffer computational platforms in the Multiphase Flow laboratory. The physical geometry of the injector was discretized using 24,000 cells (see Figure 4.3). Flow is from left to right, with the upstream plenum represented by the meshed area outside the nozzle throat.

Figure 4.3: Overview of computational grid.

There is increased mesh resolution at the inlet corner (Figure 4.4) and near the walls of the throat to attempt to resolve boundary layer effects much smaller than other flow structures. The computational domain extends past the end of the nozzle to retain the physicality of the outlet orifice; a sharp boundary there would not be physically accurate as periodic vortex shedding often occurs at the outlet.

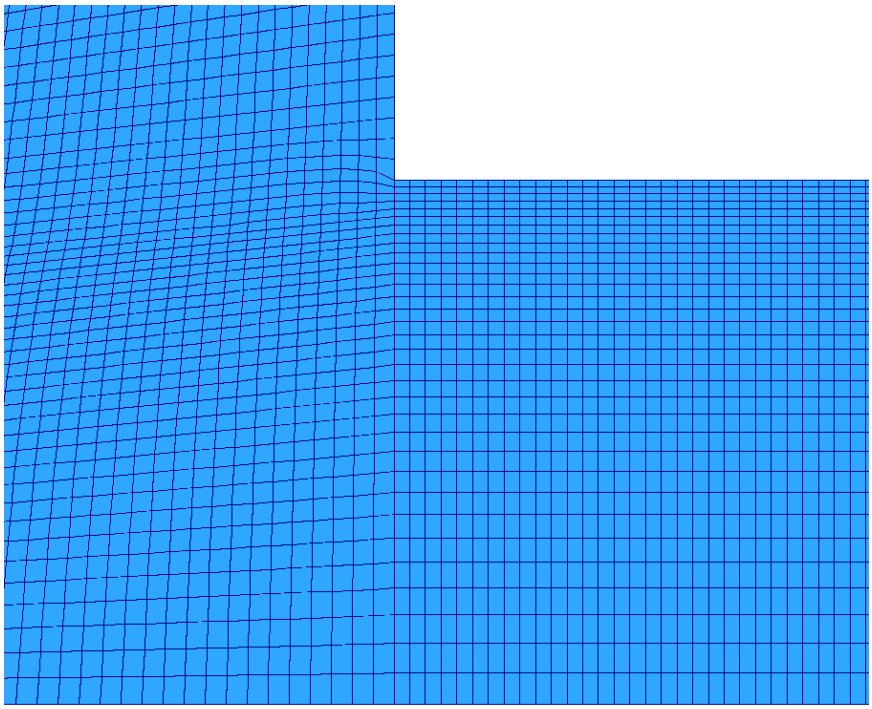

Figure 4.4: Increased mesh density at inlet corner.

The Least-Squares Algorithm

The method of iterative least squares was used to minimize the square sum of the error with respect to the expected experimental values of mass flow rate. Because the error function is dependent upon the parameters themselves *and* the sensitivity matrix ϕ (also dependent on the parameters), the function to be minimized is nonlinear, requiring an iterative solution method. Formally, the iterative least-squares is defined as [36],

$$V_N = \frac{1}{N} \sum_{t=1}^{N} \frac{1}{2} \epsilon^2(t, \theta) \tag{4.4}$$

Where ϵ is the error function, t is time, and θ is the vector of parameters to optimize. The gradient and error function are defined as,

$$V'_N = \frac{1}{N} \sum_{t=1}^{N} \psi(t, \theta) \epsilon(t, \theta) \tag{4.5}$$

$$\epsilon = y(t) - y(t) \tag{4.6}$$

with ψ as the gradient of the prediction with respect to the parameters and time, and ϵ defined as the coefficient of discharge value for a given iteration less the expected Nurick-theory value. In the current work N represents the number of cases, and Z the associated data. The V'_N term is approximated by the sensitivity matrix of the system, which measures system response to changes in the input parameters, multiplied by the current iteration's error. Each new iteration's parameters are then

$$\theta_N^{i+1} \;=\; \theta_N^i \;- \mu_N^i \left[R_N^i\right]^{-1} V'_N(\theta_N^i, Z^N) \tag{4.7}$$

where θ_N^i is the ith iteration, μ_N^i the step size. $[R_N^i]^{-1}$ is a square matrix that changes based on the chosen numerical method; when combined with V'_N, this yields change in the direction of decreasing error, incremented in proportion to the current error. The step size (or relaxation factor) mitigates this derived step size for stability. Choosing $[R_N^i]^{-1} = \mathrm{I}$, the identity matrix, makes Equation 4.7 the steepest-decent method [36]. After calculating the gradient, the proper direction of tuning for each parameter was established.

Steepest Descents

Before performing the first step, three exploratory simulations were performed; one with each parameter halved, doubled, and multiplied by six. None of the exploratory cases exhibited signs of non-physical phenomena, and did not crash. The parameter domain within these bounds was assumed stable. The prediction gradient ψ was then calculated by perturbing each parameter by 10% and comparing the change in parameter value to the change in output flow rate, as seen in Table 4.1. Cases are separated into perturbed cases (labeled by the parameter adjusted) and the baseline cases, which were calculated with the iteration-current benchmark values.

Case Name	Theta0	VoidFrac	pNonDimPress
Base	3.84E-7	-0.54	-1.76
1^{st} Perturbation	4.22E-007	-0.594	-1.94

Table 4.1: Base case and initial gradient calculation parameter values.

The gradient calculations predicted reasonable values for each of the Theta0 and pNonDimExp cases, but suggested a change of 64000% to VoidFrac (Figure 4.5). This is a spurious result - steepest descents is known to be problematic in the neighborhood of local minima, and this was certainly the case. A smaller perturbation would almost certainly have yielded more reasonable results, but in the interest of time a more stable method was selected; a method highly sensitive to step size was deemed sub-optimal with long run times.

Parameter Evaluated	Case	dtheta/dy	Epsilon	V'_N, per case	V'n	i +1 Parameter Value
theta0	K1.05	9.46E-004	-0.00957	-9.06E-006	-0.0001263896	3.20E-005
	K1.2	1.58E-003	-0.00861	-1.36E-005		
	K1.4	3.72E-002	-0.01228	-4.56E-004		
	K1.6	5.53E-004	-0.04803	-2.66E-005		
VoidFrac	K1.05	9.27E+003	-0.00957	-9.57E-003	126.170765188	-32.083
	K1.2	0.00E+000	-0.00861	-8.61E-003		
	K1.4	-5.22E+004	-0.01228	-1.23E-002		
	K1.6	1.01E+003	-0.04803	-4.80E-002		
pNonDimExp	K1.05	2.32E-003	0.00916	2.13E-005	0.000035983	-1.760
	K1.2	3.19E-004	0.00855	2.73E-006		
	K1.4	1.82E-003	0.01196	2.18E-005		
	K1.6	2.06E-003	0.04766	9.81E-005		

Figure 4.5: Steepest descents tabulated data

Hooke-Jeeves

A modified version of the Hooke-Jeeves algorithm was selected for its stability and efficiency coupled with its lack of gradient use. Because no gradient calculation is required at each step, it ideally provides more stability near a minima. Joe Bliss [5] successfully used Hooke-Jeeves to tune the vapor generation parameters for flash boiling.

Hooke-Jeeves begins with a baseline point. Similar to how the gradient was calculated in the previous section, each parameter is perturbed and the function evaluated.

Here, each parameter was perturbed by 100%, as called for by the standard Hooke-Jeeves method. If the perturbation results in a reduction of the error function, the method takes a large step in that direction, taking the perturbation case result as the new baseline. A new set of perturbation cases are examined from this new base point, and the process repeats. This is carried out until a step yields an increase in the error function, and the step size is then reduced. This continues until a sufficient error threshold is reached.

Because of the run time involved with each case, and because it was known from the gradient method that the parameters were close to the minima (within the bounds of the exploratory search), the large step size called for by Hooke-Jeeves was reduced. Normally, Hooke-Jeeves takes an acceleration step, as

$$\theta_N^{i+1} = 2\theta_N^i - \theta_0^i \tag{4.8}$$

Instead, at most steps were doubled, then when further steps did not decrease error, the step size was halved per iteration. Step size was also adjusted in cases where the derived step size would yield a value that would not make physical sense. This yielded decreasing error with each step, and is further justified by the data (Figure 4.6).

Parameter Evaluated	Perturb Prelim	Hooke-Jeeves 1	Hooke-Jeeves 2
pNonDimExp	3.22E-04	2.88E-04	2.80E-04
Theta0	3.27E-04	2.99E-04	2.76E-04
VoidFrac	3.29E-04	2.83E-04	2.78E-04
Baseline	**3.28E-04**	**2.89E-04**	**2.83E-04**

Figure 4.6: V_N Values tabulated across each case.

The parameters associated with each step are contained in Figure 4.7. The case notes explain the results of each step. Steepest Descents was used from Base to Step 1, where the VoidFrac prediction was spurious. The exploratory "doubled parameter" step was used as the baseline for the first Hooke-Jeeves step. Doubling each value

yielded a decrease in error in Theta0 and pNonDimExp, so perturbed values were accepted as the new baseline for those cases. For VoidFrac the error function increased, so the parameter was tuned in the opposite direction, at half the step-size (because the value must remain negative to retain physicality). The second Hooke-Jeeves step decreased the error function further. Its perturbations (more negative in Theta0 and pNonDimExp, less negative in VoidFrac) yielded the best values thus far.

Results and Discussion

Iteration	Case Name	Theta_0	VoidFrac	pNonDimExp	Case Notes
Base	Base	3.84E-007	-0.540	-1.76	Experimental Values
Step 1	Perturb1	4.22E-07	-0.594	-1.94	10% increase
HJStep1	Base2	7.68E-07	-0.540	-3.52	Double all values. Keep change to Theta0, pNonDim; change direction of voidFrac
	Perturb2	1.15E-06	-0.270	-5.28	Divide voidFrac by 2
HJStep2	Base3	7.68E-07	-0.270	-3.52	
	Perturb3	9.60E-07	-0.135	-4.40	step size reduced by half, kept voidFrac
	Final Values	9.60E-07	-0.135	-4.40	keep final perturbation values

Figure 4.7: Parameter Values separated by iteration and search step.

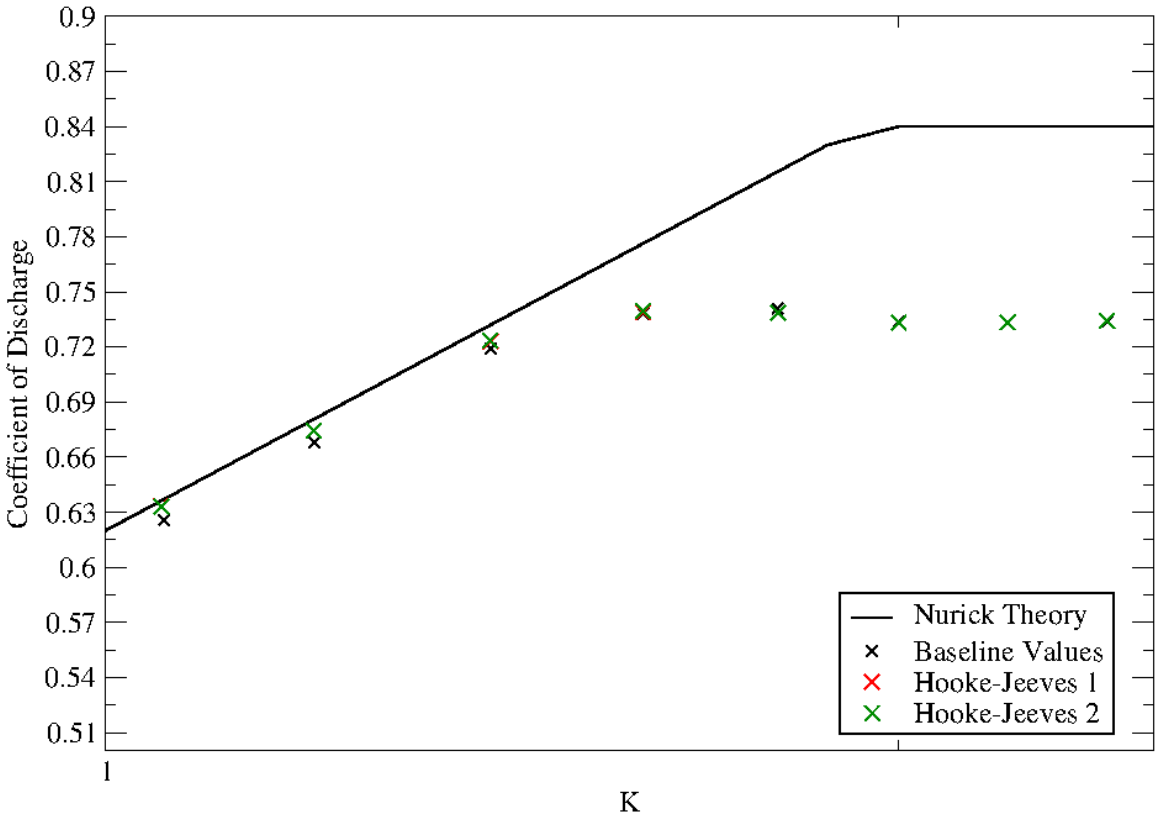

Figure 4.8: Coefficient of Discharge values by iteration.

The final (current iteration ideal) parameter values were Theta0 = 9.6E-7, VoidFrac = -0.135, and pNonDimExp = -4.40. These parameters returned an 80% decrease in the residual for the K1.05 case (most affected by vapor). As expected, the cases with pressure ratio K values larger than 1.6 showed essentailly no change, even with drastic changes to the parameters. The cases with large amounts of cavitation (K1.05, K1.2, K1.4) showed considerably more change than those above 1.7, with final resid-

uals cut down by 40.1%; over all the K values evaluated, the parameters led to a 15% decrease in overall error function value. Plotted against the Nurick Trend, these values can be found in Figure 4.8, and a closeup on the changing values in Figure 4.9. Tabulated, the coefficient of discharge data is Figure 4.10. Figures 4.8 and 4.9 show the progression of the coefficient of discharge values at each step of tuning. It should be noted that there are other sources of error beyond vapor generation, and that the current study can only go so far to mitigate that error.

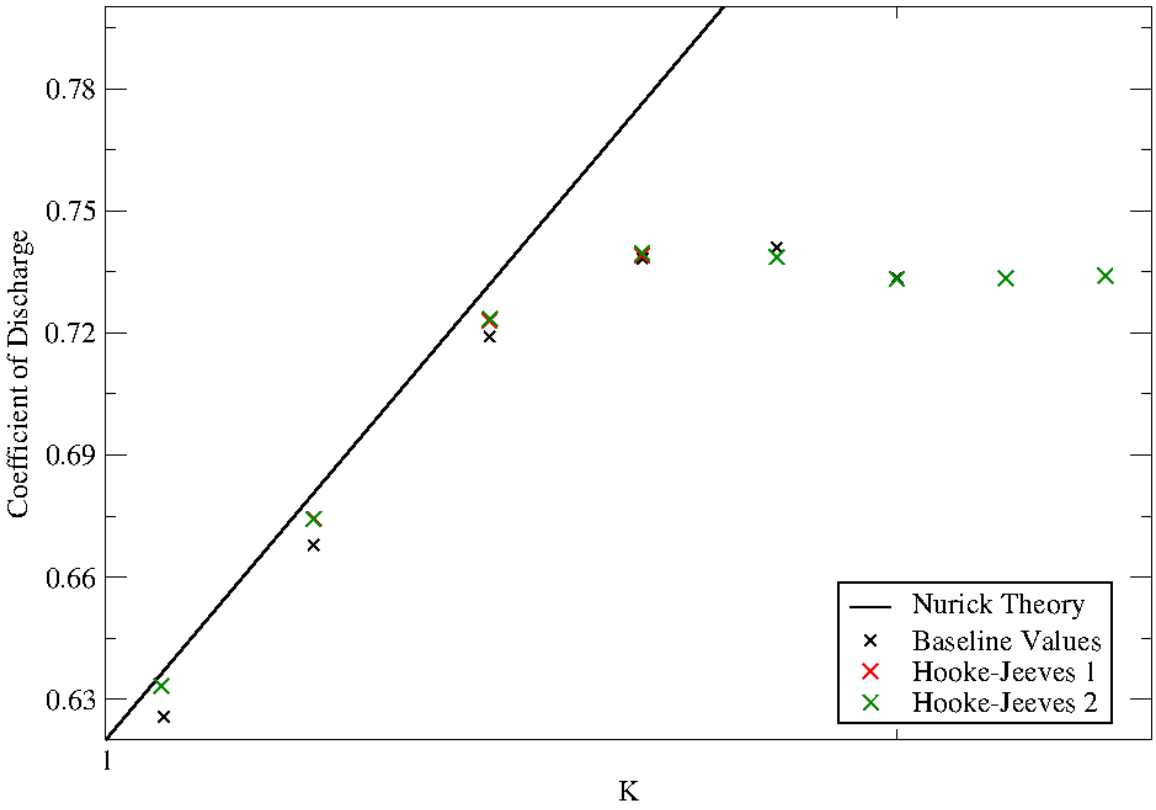

Figure 4.9: Close-up of coefficient of discharge values by iteration.

Case	Perturb Prelim	Hooke-Jeeves 1	Hooke-Jeeves 2
K1.05_BASELINE	0.62573	0.63331	0.63320
K1.2_BASELINE	0.66789	0.67435	0.67432
K1.4_BASELINE	0.71912	0.72299	0.72345
K1.6_BASELINE	0.73827	0.73904	0.73952
K1.8_BASELINE	0.74089	-	0.73867
K2.0_BASELINE	0.73351	-	0.73321
K2.2_BASELINE	0.73344	-	0.73343
K2.4_BASELINE	0.73395	-	0.73409

Figure 4.10: Tabulated coefficient of discharge data, by iteration.

CHAPTER 5

HEAT TRANSFER: EXPERIMENTAL CASES AND COMPUTATIONAL IMPLIMENTATION

Considering a fuel injector adiabatic is a reasonable simplifying approximation in simulation. With a prescribed inlet temperature, known pressure conditions, and experimentally validated vapor generation rates, flow rates near those of physical injectors can be expected. However, within the injector an engine-heated wall is a source of added enthalpy, causing boiling to occur along the injector's surface at higher temperature [6]. In HRMFoam, the ability to model non-adiabatic flows would yield a more rigorous prediction tool at elevated temperature and provide a more complete picture of fuel vaporization. To that end, the present work will implement and evaluate the energy transport equation in HRMFoam.

Because enthalpy transport from a heated surface to a liquid coolant describes the cooling of nuclear reactors, heat sink applications, and others, basic heat transfer in the context of internal channel flow has been the subject of numerous studies [34] [6] [22]. For our purposes, tube heat transfer experiments represent straightforward validation cases for the transport of enthalpy in HRMFoam. When considering the specific case of heat transfer in tubes, there are two canonical boundary conditions [25] [29]. With the specified heat rate boundary condition, a heat flux is prescribed per unit tube length. This is a reasonable mathematical description for heat caused by electric resistance, by radiant or nuclear heating, or in heat exchangers with fluids of comparable fluid capacity rates [29]. In contrast, the specified surface temperature boundary condition is appropriate in heat exchangers when there is a disparity in heat capacity between the fluids [29]. The present work examines experiments by

Allen [1] and Boelter [6] to validate enthalpy transport through the specified heat flux and specified surface temperature boundary conditions.

5.1 Transport of Energy and HRMFoam

As formulated by White [66], the energy equation is,

$$\rho\frac{Dh}{Dt} = \frac{Dp}{Dt} + \nabla\cdot(k\nabla T) + \Phi \tag{5.1}$$

where ρ is density, h is enthalpy, p is pressure, k is conductivity, T is temperature, and Φ is the dissipation function. The dissipation function Φ represents the viscous stresses; because viscosity cannot add energy to the system, the Φ matrix is positive definite [66]. For now, the viscous stress term will be neglected for simplicity. We also neglect the molecular diffusion of heat, $\nabla\cdot(k\nabla T)$. At high Reynolds number, where HRMFoam is generally used, this term is negligible compared to turbulent heat transport. Confining the discussion to the expanded material derivative terms on the left hand side, we include continuity multiplied by enthalpy h (in essence adding zero),

$$\rho\frac{\partial h}{\partial t} + \rho u\cdot\nabla h + h\left(\frac{\partial\rho}{\partial t} + \nabla\cdot\rho u\right) \tag{5.2}$$

Combining terms, we arrive at our strong conservation form of the energy equation,

$$\frac{\partial\rho h}{\partial t} + \nabla\cdot\rho uh = \frac{Dp}{Dt} \tag{5.3}$$

Using Equation 5.3 as a starting point, we decompose instantaneous pressure into its mean ($\bar{p}$) and fluctuating (p') components, and the instantaneous enthalpy and velocity into their mass-averaged ($\tilde{h}, \tilde{u}$) and fluctuating (h'', u'') components,

$$p = \bar{p} + p'$$

$$h = \tilde{h} + h''$$

$$u = \tilde{u} + u''$$

We avoid decomposing density ρ and invoke the mass average to circumvent the closure problems associated with time-averaged products of fluctuating terms. Without knowing the degree of correlation between ρ' and u'', etc, there are terms that are difficult to eliminate when products with density arise. The mass average is defined as [32] [67],

$$\tilde{u} = \frac{1}{\bar{\rho}} \lim_{T \to +\infty} \int_t^{t+T} \rho(\tau) u_i(\tau) d\tau \ = \frac{\overline{\rho u}}{\bar{\rho}} \tag{5.4}$$

Applying the mass average decompositions, the left-hand side of Equation 5.3 becomes,

$$\frac{\partial(\rho)(\tilde{h} + h'')}{\partial t} + \nabla \cdot (\rho)(\tilde{u} + u'')(\tilde{h} + h'') \tag{5.5}$$

Note that we do not decompose either density term. Expanding terms,

$$\frac{\partial(\rho\tilde{h} + \rho h'')}{\partial t} + \nabla \cdot (\rho\tilde{u}\tilde{h} + \rho\tilde{u}h'' + \rho u''\tilde{h} + \rho u''h'') \tag{5.6}$$

To obtain the Farve-averaged heat equation, we apply a time average to Equation 5.6 in the procedure of Wilcox [67], keeping in mind that this is still only the left-hand side. Several of these terms can be eliminated; recall the definition of the mass-averaged velocity,

$$u = \tilde{u} + u'' \tag{5.7}$$

Multiplying Equation 5.7 through by ρ and applying a time average yields,

$$\overline{\rho u} = \bar{\rho}\tilde{u} + \overline{\rho u''} \tag{5.8}$$

Equation 5.4 in terms of Reynolds averaging [67] is,

$$\bar{\rho}\tilde{u} = \overline{\rho u} \tag{5.9}$$

Based on Equation 5.9, we can then say:

$$\overline{\rho u''} = 0 \tag{5.10}$$

With this, we apply a time average to Equation 5.6. When multiplied by $\rho u''$ or $\rho h''$ and then time averaged, a mass-averaged mean term ($\tilde{u}$ or $\tilde{h}$) acts as a coefficient to the known average value (Equation 5.10), resulting in zero. The left-hand side of the energy equation becomes,

$$\frac{\partial \bar{\rho}\tilde{h}}{\partial t} + \nabla\cdot\left(\bar{\rho}\tilde{u}\tilde{h} + \overline{\rho u'' h''}\right) \tag{5.11}$$

Turning our attention to the right side of Equation 5.3, we expand the material derivative term. The right hand side has no term that might produce problematic correlated fluctuation terms that might also be avoided by a Farve Average, so only Reynolds Averaging is necessary. We decompose p and h in time, yielding,

$$\overline{\frac{\partial(\bar{p} + p')}{\partial t}} + \overline{(\bar{u} + u')\cdot\nabla(\bar{p} + p')} \tag{5.12}$$

Eliminating the time-averaged fluctuating terms without possible correlation issues results in,

$$\frac{\partial \bar{p}}{\partial t} + \bar{u} \cdot \nabla \bar{p} + \overline{u' \cdot \nabla p'} \tag{5.13}$$

Combining the left and right-hand sides yields the Farve-averaged energy equation,

$$\frac{\partial \bar{\rho} \tilde{h}}{\partial t} + \nabla \cdot \bar{\rho} \tilde{u} \tilde{h} = \frac{\partial \bar{p}}{\partial t} + \bar{u} \cdot \nabla \bar{p} + \overline{u' \cdot \nabla p'} - \nabla \cdot \overline{\rho u'' h''} \tag{5.14}$$

The turbulent dispersion term $\nabla \cdot \overline{\rho u'' h''}$ is modeled as $\nabla \cdot \alpha_{total} \rho \nabla h$, where α_{total} is the total diffusivity. The formulation of α_{total} will be described shortly. The Farve-averaged energy equation is implemented in the current HRMFoam framework.

Two modifications have been made in the implementation of Equation 5.14. The $\overline{u' \cdot \nabla p'}$ term is small below Mach 1, and can be safely regarded as zero at low Mach number [71]. Because most HRMFoam applications involve velocities below the speed of sound, this is a reasonable concession. Additionally, a viscous dissipation term is included, derived from the viscous terms of the stress tensor τ_{ij} [66],

$$\tau_{ij} = -p\delta_{ij} + \mu(\frac{\delta u_i}{\delta x_j} + \frac{\delta u_j}{\delta x_i}) + \delta_{ij} \lambda \nabla \cdot U \tag{5.15}$$

where μ is the dynamic viscosity, λ is the coefficient of bulk viscosity, and δ is the Kronecker delta. The hydrostatic pressure term is not included in the viscous stresses. Assuming incompressible flow ($\lambda \nabla \cdot U = 0$), the viscous dissipation term added to the right hand side of Equation 5.14 is,

$$\mu_{eff}((\nabla U + \nabla U^T) \cdot \nabla U) \tag{5.16}$$

This formulation is normally used for laminar flow. However, because the stress tensor τ_{ij} comes from the momentum equation and includes the effective dynamic viscosity μ_{eff}, we include it here for the sake of consistency in our treatment of energy.

To better handle two-phase flow and the presence of non-condensible gas, the definitions of heat capacity C_p and subsequently laminar thermal diffusivity α have

been revised as $C_{p,mix}$ and α_{mix}. The definitions of vapor fraction and dryness fraction x are unclear in the presence of a liquid working fluid, vapor working fluid, and a quantity of non-condensible gas. Quality x represents the ratio of working fluid in the vapor phase to working fluid in the liquid phase in a given computational cell by mass, as,

$$x \equiv \frac{m_{vapor}}{m_{workingfluid}} \tag{5.17}$$

No measure of non-condensible gas is included in x. To that end, y is the ratio of gas to total mass (liquid working fluid, vapor working fluid, and non-condensible gas) in a cell, as,

$$y \equiv \frac{m_{gas}}{m_{total}} \tag{5.18}$$

With these definitions in mind, the total laminar diffusivity used in the transport of enthalpy is calculated from the heat capacity of the total mass in a cell. This is computed as,

$$C_{p,mix} = (1-x)(1-y)C_{p,liquid} + x(1-y)C_{p,vapor} + yC_{p,gas} \tag{5.19}$$

This mixture heat capacity $C_{p,mix}$ reflects the ratio of the phases and gas by total mass present. The laminar diffusivity for the mixture is then,

$$\alpha_{mix} = \frac{K}{C_{p,mix}} \tag{5.20}$$

Where K is thermal conductivity. The total diffusivity used in calculating enthalpy transport is the sum of the turbulent diffusivity α_t and laminar thermal diffusivity α_{mix}.

5.2 Enthalpy Boundary Conditions

5.2.1 Specified Heat Flux: Allen Experiment

To validate Equation 5.14, we begin with the specified heat flux boundary condition and Allen's experiments. In Allen's [1] work, single-phase liquid water was passed through a long pipe heated electrically with a constant specified heat flux. After passing through an adiabatic entrance pipe of L/D 96 to reach hydrodynamic equilibrium, the fluid reaches a heated test section of diameter 0.75 inch and L/D 30. The test section was heated by electric current and insulated thermally at the outer wall. The system was kept at 75 psia (0.517 MPa). A control point was defined 22 diameters from the entrance of the test section to provide a point of reference for measuring relevant fluid quantities. At the control point, Reynolds number was 50,000, Prandtl number was 7, and wall-to-bulk-flow temperature difference was 24°Fahrenheit (F). Over the length of the heated section, bulk fluid temperature rise was 5.87 °F, with fluid entering at 59.65 °F (288.515K).

Allen quantified his results through heat transfer coefficient h, calculated as,

$$h = \frac{q''}{t_w - t_b} \tag{5.21}$$

where q'' is the heat flux, t_w and t_b are the temperature of the wall and bulk flow, respectively, for each axial location examined in the pipe. Allen evaluated and averaged the heat transfer coefficient along the last six diameters of the test section and used the computed h_{ref} to normalize the heat transfer coefficient at various axial positions along the pipe. Plotting these against the analytical results of Sparrow [59] and Deisler [14], Allen's results show an asymptotic approach to the reference h from the entrance to the outlet (Figure 5.1). The present work seeks to replicate the experimental bulk temperature rise and heat transfer coefficient curve.

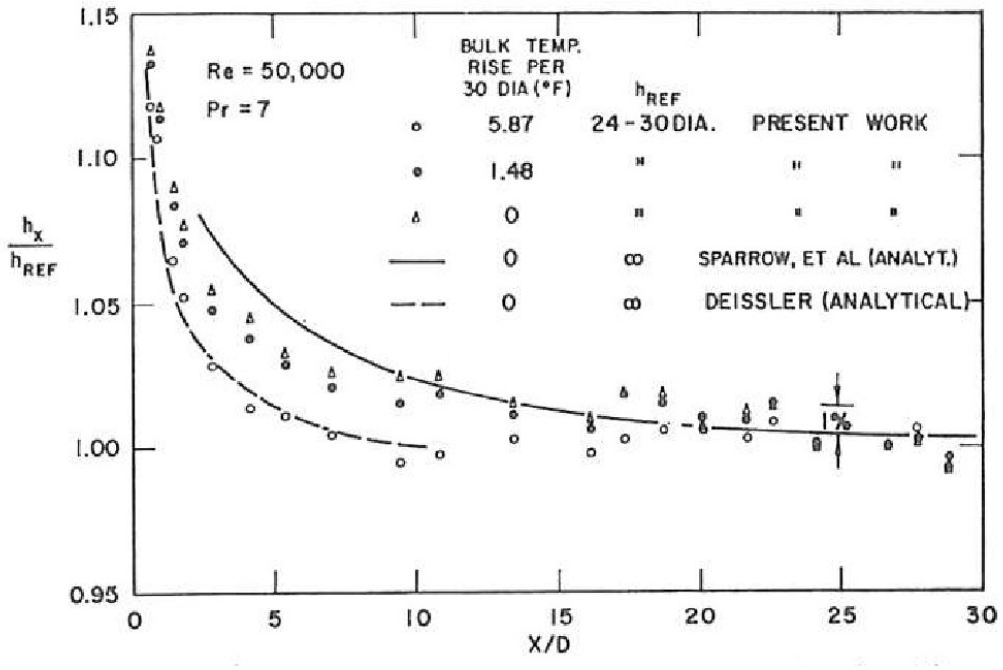

Figure 5.1: Local heat transfer coefficient from Allen's experiments plotted against Sparrow [59] and Deisler [14]. Figure from Allen [1].

5.2.2 Numerical Approach: Allen

Allen prescribed a constant heat flux over a known area, and reported the fluid's bulk temperature rise. In the experiment, the pipe surface temperature was measured via a set of 30 thermocouples attached to the outside of the tube. To replicate the conditions of Allen's experiment, the experimental heat flux into the pipe is calculated as the total heat added (Q_{in}) over the surface area of the pipe. From the bulk temperature rise, pipe surface area, and mass flow rate ($\dot{m}$), the heat flux q'' is [25],

$$q'' = \frac{Q_{in}}{\pi DL} = \frac{\dot{m} C_p (T_{out} - T_{in})}{\pi DL} \tag{5.22}$$

where D is the pipe diameter, L is the pipe length, C_p is the heat capacity at constant pressure. The outlet and inlet temperatures are T_{out} and T_{in}. To find the temperature gradient over the pipe wall due to this heat flux, we use Fourier's law [25],

$$q'' = -k\frac{dT}{dx} \tag{5.23}$$

where k is thermal conductivity and $\frac{dT}{dx}$ is the temperature gradient. Given the inlet temperature and the linear rise in bulk fluid temperature (Fig. 5.2), the average bulk temperature is known analytically. For a given heat flux, the bulk temperature at some distance x from the inlet is [25],

$$T_{bulk}(x) = T_{in} + \frac{\pi D q'' x}{\dot{m} C_p} \tag{5.24}$$

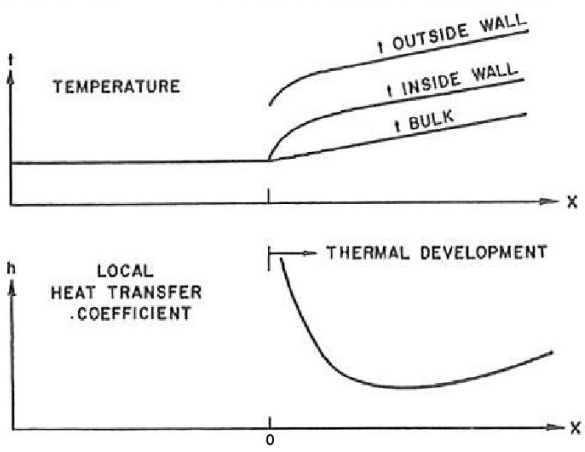

Figure 5.2: Experimental temperature and local heat transfer coefficient plotted with axial position along the heated pipe. Note the linear rise in bulk temperature and shape of local heat transfer coefficient curve. Figure from Allen [1].

A new boundary condition was implemented to properly address the prescribed heat flux. Under these conditions, a bulk rise of 5.87°F over the pipe length corresponds to a constant heat flux of 315,943 watts per square meter. Because the heat flux is known and constant, enthalpy gradient through the wall is calculated through local total diffusivity α_{total} as,

$$\frac{dH}{dx} = \frac{q'' C_p}{k} = \frac{q''}{\alpha_{total}} \tag{5.25}$$

where α_{total} is the sum of the laminar and turbulent α values. With the assumption that the enthalpy calculated at each near-wall cell was the enthalpy of the wall itself,

the "sample" OpenFOAM utility was used to extract wall enthalpy values. These were used to calculate heat transfer coefficient as per Allen (using Equation 5.21), using the bulk temperature values from Equation 5.24. Due to the curve's sensitivity to turbulent diffusivity, several turbulence models were used for completeness: kEpsilon, realizable kEpsilon, and Spalart-Allmaras.

Allen's work featured a long section of unheated pipe before the test section to ensure hydrodynamically developed conditions. At the experimental Reynolds number of 50,000, turbulent pipe flow reaches hydrodynamic equilibrium 26.7 diameters from a pipe inlet [48]. The modeled domain of 30 diameters is sufficiently long for this purpose. Simulations were allowed to reach steady state to create hydrodynamically developed conditions at the outlet. These outlet conditions were then transposed to the pipe inlet, emulating the long approach section of pipe in the experimental set-up with a minimum of computational cells. Because the inlet and outlet cell indicies are numbered similarly, translation between patches is straightforward.

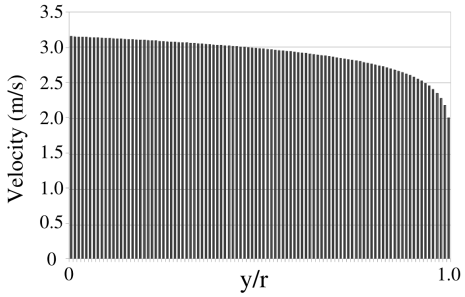

Figure 5.3: Streamwise velocity vs. transverse distance. Velocity is at minimum at the wall (y/r = 1).

Fully-developed turbulent pipe flow adheres to a log-law velocity profile; the initially prescribed inlet velocity is shown in Figure 5.3. Best initial guesses for turbulent kinetic energy k, turbulent dissipation ϵ, and the viscosity-like quantity $\tilde{\nu}$ are described in the following sections. Once temporal steady-state was achieved, the outlet conditions for velocity, k, ϵ, $\tilde{\nu}$, kinematic viscosity μ, and eddy-viscosity μ_t

were transplanted to the pipe inlet, then allowed to run to steady state again. Until the turbulent diffusivity was no longer spatially developing between the inlet and outlet (as in Figure 5.4), the process of moving outlet conditions to the pipe inlet was repeated. Note also that each field data figure depicts the entire pipe length; a scale factor of 0.1 has been applied.

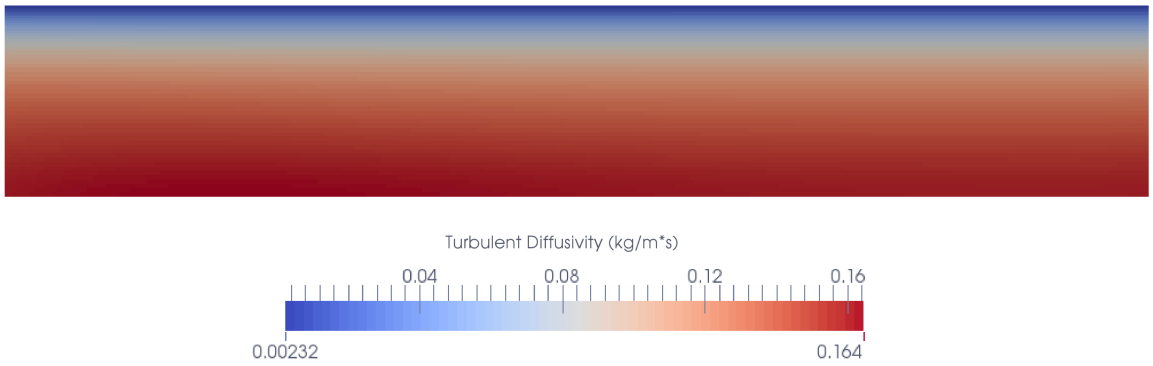

Figure 5.4: A converged turbulent diffusivity α_t field. Once α_t no longer develops spatially, simulations were considered converged. Figure from kEpsilon model.

The velocity, pressure, and vapor fraction fields were not strongly affected by the choice of turbulence model. For each, velocity was an average of 2.871 m/s over the inlet and outlet patches, with a maximum of 3.32 m/s (Figure 5.5). Pressure drop through the test section was slight at 3 kPa due to the no-slip walls boundary condition on velocity. The fluid was single-phase throughout. The performance of each model differed predominantly in the prediction of α_t and distribution of enthalpy in the flow.

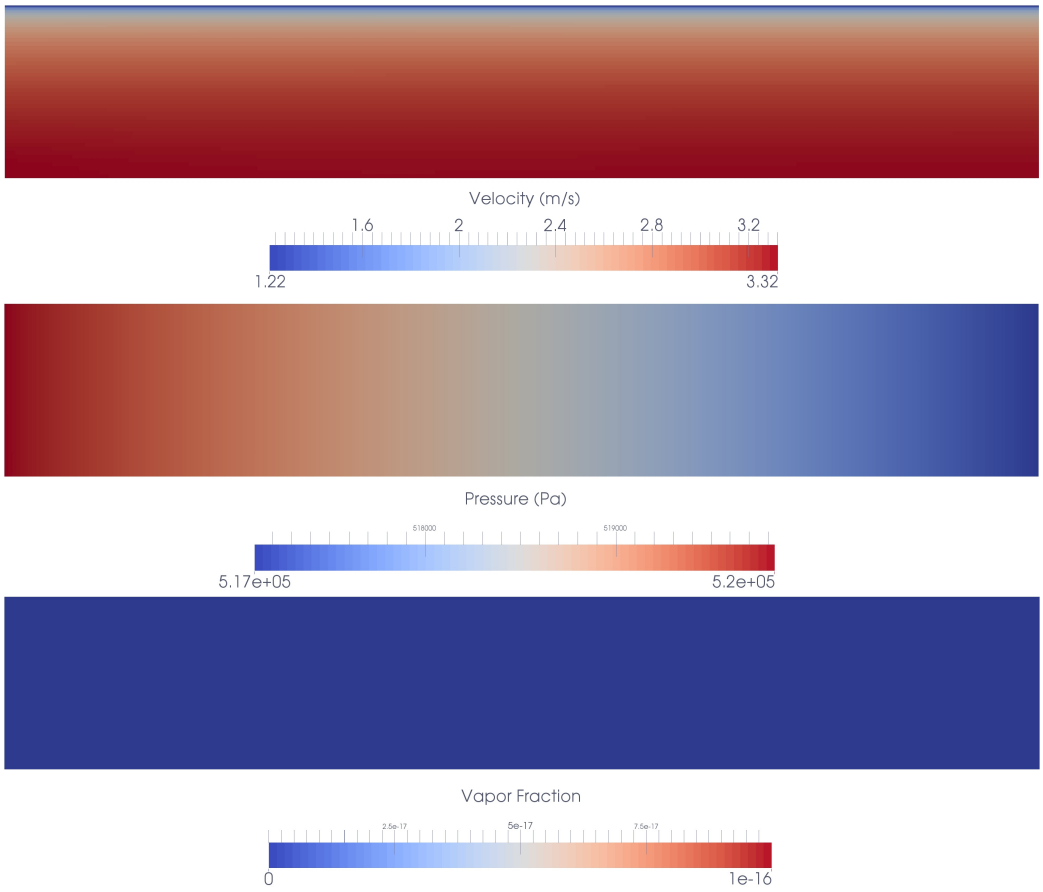

Figure 5.5: Allen simulation velocity, pressure, and vapor fraction. These fields remain largely unchanged between the three turbulence models. *(Top)* Velocity increases rapidly spanwise, while *(Middle)* pressure drops linearly between the inlet and outlet. *(Bottom)*Vapor fraction is constant throughout the flow.

5.2.3 Specified Surface Temperature: Boelter Experiment

Next we turn to a second set of experiments performed by Boelter et al [6]. Boelter's [6] work yielded temperature and pressure drop data for the flow of liquid water through a heated vertical drawn steel tube, as well as heat flux density and mass flow rate readings. High pressure, high temperature water was tested both with and without surface boiling.

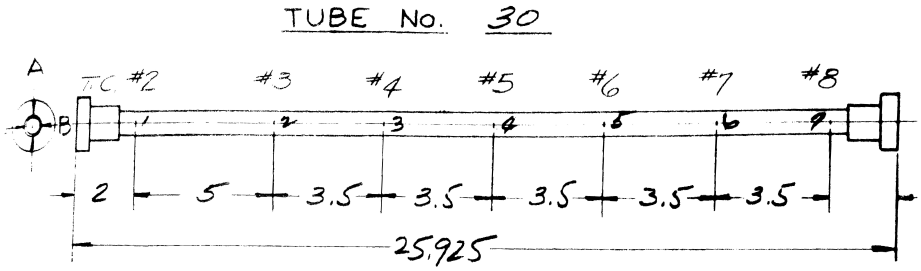

Point of Measurement		O.D. (in.)	I.D. (in.)	O.D.-I.D. (in.)	Avg. Wall Thickness (in.)
A	1	0.2515	0.2298	0.0217	0.0108
	2	0.2513	0.2297	0.0216	0.0108
	3	0.2512	0.2295	0.0217	0.0108
	4	0.2512	0.2297	0.0215	0.0108
	5	0.2514	0.2298	0.0216	0.0108
	6	0.2514	0.2299	0.0215	0.0108
	7	0.2506	0.229	0.0216	0.0108
B	1	0.2513	0.2296	0.0217	0.0108
	2	0.2513	0.2295	0.0218	0.0109
	3	0.2512	0.2294	0.0218	0.0109
	4	0.2512	0.2295	0.0217	0.0108
	5	0.2513	0.2297	0.0216	0.0108
	6	0.2513	0.2296	0.0217	0.0108
	7	0.2518	0.2295	0.0223	0.0111

Figure 5.6: Tube dimensions for a typical test section used in the UCLA water experiments [6]. Note the thermocouple locations positioned in intervals along the tube's length.

The experimental apparatus forced fluid upward through an L/D 100 section of $\frac{1}{4}$ inch diameter pipe, electrically heated along its length. The dimensions of a typical test section are visible in Figure 5.6, with thermocouples positioned as noted. Most tests were conducted at 2000 psia (13.8 MPa), at temperatures varying from 461K

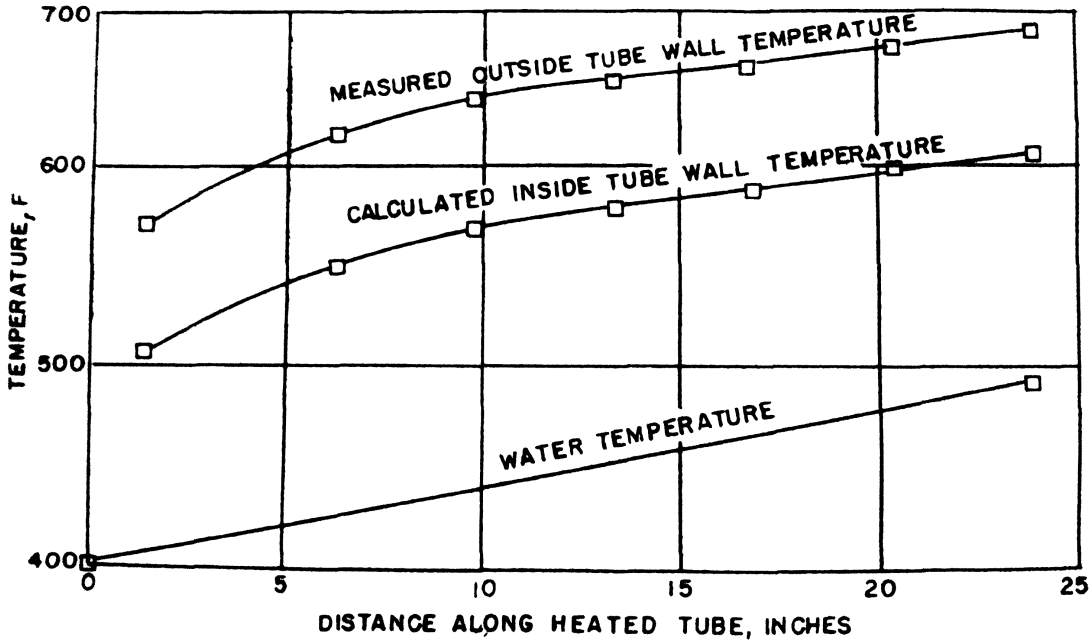

Figure 5.7: Boelter high-temperature, high-pressure water experimental data [6].

up to 589K. Varying quantities of nitrogen gas were dissolved in the water, with runs including up to 900 cc N_2 added per liter. For the purposes of the present work we consider a basic, no surface boiling, de-gassed water run.

Figure 5.7 shows the wall and fluid temperature profiles for run #448 [6]. The bulk fluid temperature begins at 398.93°F (477K), increasing to approximately 490.73°F (528K) by the heated section's exit. Equilibrium properties at these conditions indicate no vapor at the entrance or exit, providing a straightforward single-phase validation case.

5.2.4 Numerical Approach: Boelter

With a full pipe length of 100 diameters, simulating the entire test section used by Boelter would be cost-prohibitive. Instead, the region of the first three points of the calculated inside wall temperature was used, from 1.282 inches (where heating begins) to 9.622 inches (the third data point in Figure 5.7). This leaves an 8.34 inch

(0.211 meter), L/D 36.3 region of pipe, 0.2289 inches (0.0058 m) in diameter. The mesh was the same used in the Allen simulations, a 5° wedge comprised 104,000 cells, scaled appropriately.

Fluid entering the domain was set to the bulk flow temperature at 1.282 inches from the pipe entrance, 481.8K. The wall's steady state temperature was 541K at the inlet, increasing axially to 578.8K at the outlet with the profile shown in Figure 5.7. Based on the Reynolds number of 336,000, the inlet velocity was set to a log-law profile, with an average of 8.8 m/s. Fluid entering through the inlet boundary was entirely liquid. kEpsilon was used for the calculation of turbulent diffusivity α_t, and therefore enthalpy transport. Once steady state was achieved, the outlet conditions were moved to the pipe inlet, much like the Allen simulations.

5.3 Turbulence Models

Three turbulence models were applied to the Allen and Boelter simulations. The kEpsilon and realizable kEpsilon models were used for both sets of experiments, while Spalart-Allmaras was used only for the Allen case. The three models differ in their calculation of turbulent diffusivity α_t, changing the transport of enthalpy in the domain.

5.3.1 kEpsilon

The kEpsilon turbulence model solves for the transport of turbulent kinetic energy k and turbulent dissipation ϵ. Initial estimates of turbulence quantities at the inlet were made for k, ϵ, and turbulence intensity I. Turbulence intensity represents the ratio of mean flow velocity fluctuation to the mean flow velocity, expressed as a percentage. At the core of a fully developed internal flow, the turbulence intensity I is dependent upon Reynolds number, and at the pipe inlet is approximately [2],

$$I = 0.16Re^{-\frac{1}{8}} \tag{5.26}$$

For our Reynolds number of 50,000, the flow fluctuates by approximately 4%. Turbulent kinetic energy and dissipation rate are empirically then [2],

$$k = \frac{3}{2}(\bar{u}I)^2 \tag{5.27}$$

$$\epsilon = \frac{0.1643k^{1.5}}{l} \tag{5.28}$$

where $\bar{u}$ is the mean flow velocity, and l is the characteristic length of a given flow. For internal channel flow, the diameter of the pipe is used for l. The eddy-viscosity is calculated as,

$$\mu_t = \frac{C_\mu \rho k^2}{\epsilon} \tag{5.29}$$

where C_μ is a model constant. The turbulent diffusivity is then,

$$\alpha_t = \frac{\mu_t}{Pr_t} \tag{5.30}$$

where Pr_t is the turbulent Prandtl number, assumed unity in kEpsilon.

Note that the kEpsilon value of C_μ (0.09) makes the model applicable to a variety of flows. While not ideal for every flow, it is most accurate for the inertial sublayer in a developed boundary layer. In the near-wall region below non-dimensional values of $y+$ values of 50 (which will be detailed later in the text), smaller values of C_μ are more appropriate [48]. For this reason, kEpsilon is known to be suboptimal in simulating the viscous near-wall region.

5.3.2 Realizable kEpsilon

Realizable kEpsilon is the standard kEpsilon model with altered handling for eddy-viscosity, along with changes to the dissipation calculation using mean-square vorticity fluctuation [19]. Whereas C_μ is a model constant under kEpsilon, it is variable in Realizable kEpsilon. This ensures that both the normal stresses and the Schwarz inequality for the shear stresses remain positive (realizable) [19]. This changes the eddy-viscosity μ_t, thereby affecting α_t.

5.3.3 Spalart-Allmaras

Spalart-Allmaras is a single-equation model that solves for a term identical to turbulent viscosity except in the viscous near-wall region, $\tilde{\nu}$ [2]. Turbulent viscosity is computed from $\tilde{\nu}$, which is initialized at the pipe inlet as,

$$\tilde{\nu} = \sqrt{\frac{3}{2}}\bar{u}Il \tag{5.31}$$

Turbulent viscosity is then,

$$\mu_t = \rho\tilde{\nu}f_{v1} \tag{5.32}$$

where f_{v1} is the viscous damping function, determined by a ratio of $\tilde{\nu}$, kinematic viscosity ν, and a model constant. While Spalart-Allmaras is intended for external aerodynamic flows, it performs well in the present work.

CHAPTER 6

COARSE MESH APPROACH

Each experiment was first examined on a coarse grid. Due to the low resolution, subgrid-scale near-wall approximations are necessary to ensure accurate prediction. The velocity and thermal boundary layers develop rapidly outward from the wall, and require special consideration related to the minimum mesh resolution.

6.1 Near-wall Boundary Layer Modeling

Boundary layers are the viscous layers that originate from solid surfaces in fluid flows. The mean flow is predominantly parallel to the surface in the downstream direction. Velocity changes spanwise with location in the boundary layer. Non-dimensional normal distance from the wall y^+ is defined as,

$$y^+ = \frac{yu_t}{\nu} \tag{6.1}$$

where y is the physical distance from the wall, u_t is the shear velocity, and ν is the kinematic viscosity. Alternatively, y^* is sometimes used as the non-dimensional wall distance, defined as,

$$y^* = \frac{\rho C_\mu^{\frac{1}{4}} k_p^{\frac{1}{2}} y_p}{\mu} \tag{6.2}$$

where y_p is the physical distance from the surface to the nearest cell center.

The rapid changes in velocity that occur normal to the wall within the boundary layer are classified into stratified layers, grouped by regions of y^+ (Figure 6.1). In the

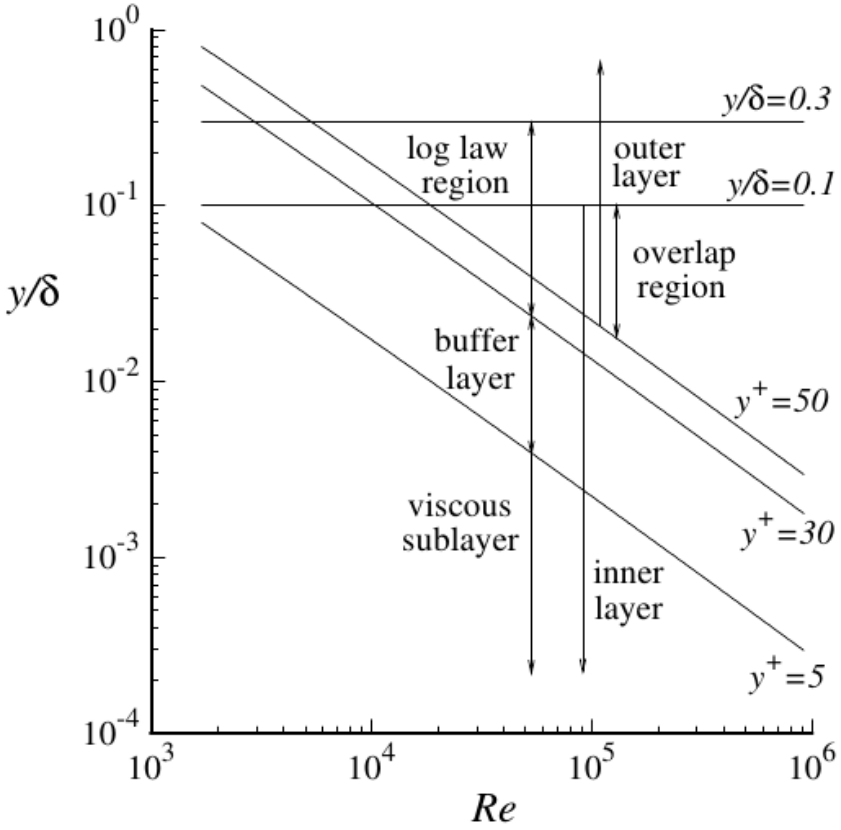

Figure 6.1: Boundary Layer Regions by non-dimensional wall distance and Reynolds number. Distance to the wall y is non-dimenionalized by the channel half-width δ in pipe flow. The entire inner layer exists between the wall and 10% of the distance to the centerline. Figure from Pope [48].

viscous near-wall region, velocity increases linearly, while in the logarithmic region dimensionless velocity is given by,

$$u^+ = \frac{1}{\kappa} ln(y^+) + C^+ \tag{6.3}$$

where the von Karman constant κ is 0.41, and C^+ is empirically defined and related to boundary layer thickness [18]. Modeling near-wall flow depends upon accurately reproducing the behavior of the boundary layer regions.

Generally, there are two main approaches to modeling the boundary layer velocity. The boundary layer region is either discretized using a high cell density or approx-

imated through wall functions that simulate the viscous sub-layer and buffer region behavior across a single near-wall cell. In the first approach, the first cell at the wall must correspond to a y^+ of no more than 5 [20]. Because velocity increases linearly from the wall to roughly $y^+ = 5$ (across the viscous sublayer) [48], linear interpolation across the single near-wall cell is an adequate approximation. In the kEpsilon model, no-slip is imposed for the wall velocity, and turbulent kinetic energy k is set to zero at the wall. Dissipation on the wall surface is not zero in that case, but instead set to [18],

$$\epsilon = \nu \left(\frac{\partial^2 k}{\partial y^2} \right)_{wall} \tag{6.4}$$

or,

$$\epsilon = 2\nu \left(\frac{\partial k^{\frac{1}{2}}}{\partial y} \right)^2_{wall} \tag{6.5}$$

These boundary conditions are typically combined with a turbulence model modified to handle the low Reynolds number flow near the wall in addition to an appropriately large mesh resolution.

Wall functions are a less computationally expensive alternative. Because high Reynolds number flow causes the viscous sublayer to become extremely thin, boundary layer velocity and turbulence are often approximated. Wall functions model fluid behavior near the wall without the need to resolve into the linear region. After imposing the experimentally-validated [18] velocity profile of the viscous sub-layer and buffer layer across the first cell at the wall [13], a simple logarithmic velocity profile will then suffice for the rest of the boundary layer. Modeling is therefore more straightforward, but requires that the cell nearest the wall be no smaller than $y^+ = 30$, where solution accuracy begins to deteriorate [20] [18]. This allows the use of a less refined mesh. However, the logarithmic layer must extend no farther into the

flow than a y^+ of 500 [13]. Use of wall functions includes the assumption of high Reynolds number, negligible flow-direction pressure gradient, and velocity variation in the normal direction only [64].

6.2 Coarse Mesh Results

The Allen case used a mesh with a first node y^+ value of 32, with 13 cells across the inlet (Figure 6.2, *top*) and 15,600 cells total. The Boelter mesh had 22 cells across the radius (Figure 6.2, *bottom*) and 17,600 total cells. Due to the higher velocities in the smaller diameter Boelter pipe, an effort was made to increase aspect ratio in the direction of the flow while maintaining reasonable cell quality. The first cell y^+ was 37, with an aspect ratio of 8 to avoid extended runtimes due to the Courant number restriction.

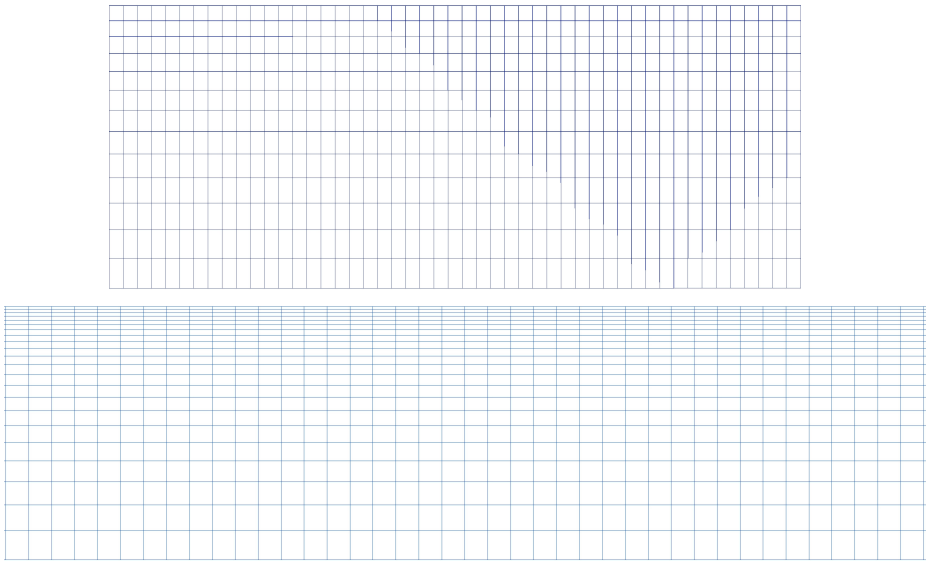

Figure 6.2: Meshes for use with wall functions. *(Top)* Allen mesh: first near-wall node corresponds to $y^+ = 32$, 15,600 cells. Maximum cell aspect ratio is 1.6. *(Bottom)* Boelter mesh: first point $y^+ = 37$, 17,600 cells. Note the exaggerated axial dimension. Maximum cell aspect ratio is 8.

With wall functions, the diffusive flux of turbulence kinetic energy is assumed zero through the wall [18]. This makes the normal derivative of k zero on the boundary. Figure 6.3 shows the values of k throughout the pipe, for the Allen kEpsilon, Allen realizable kEpsilon, and Boelter coarse mesh runs, and the zeroGradient boundary condition at the wall. Spalart-Allmaras has its own near-wall handling, and as such is only employed on the fine resolution mesh. Balance of production and dissipation is generally assumed [18] due to the nearly constant near-wall shear stress, yielding a relation between velocity and wall shear stress at the first near-wall node,

$$P_k \approx \tau_w \frac{\partial \bar{v}_t}{\partial y} \tag{6.6}$$

where P_k is turbulence production and v_t is shear velocity. The velocity gradient is derived from the log-law as,

$$\left(\frac{\partial \bar{v}_t}{\partial y}\right)_P = \frac{u_\tau}{\kappa y_p} = \frac{C_\mu^{\frac{1}{4}} \sqrt{k_p}}{\kappa y_p} \tag{6.7}$$

where the subscript P denotes evaluation at the near-wall cell.

The coarse mesh approach to the Allen and Boelter cases applies a constant heat flux condition for both, for a more straightforward approach. A more detailed approach will follow, using fixed boundary temperature for the Boelter simulation. The Allen case uses a constant heat flux of 321,049 $\frac{W}{m^2}$, while the Boelter case's boundary is heated with 4,395,490 $\frac{W}{m^2}$. In the Boelter case, higher velocities and a smaller pipe translate to much larger maximum turbulence quantities. Because dissipation depends upon wall-normal spanwise velocity gradient, it is largest close to the wall, where velocity changes rapidly (Figure 6.4). The turbulence kinetic energy and dissipation fields lead to high turbulent diffusivity near the wall, as α_t depends on k^2 (Figure 6.5). Due to the difference in predicted turbulent diffusivity, realizable kEpsilon shows higher near-wall enthalpy than standard kEpsilon for the Allen case (Figure

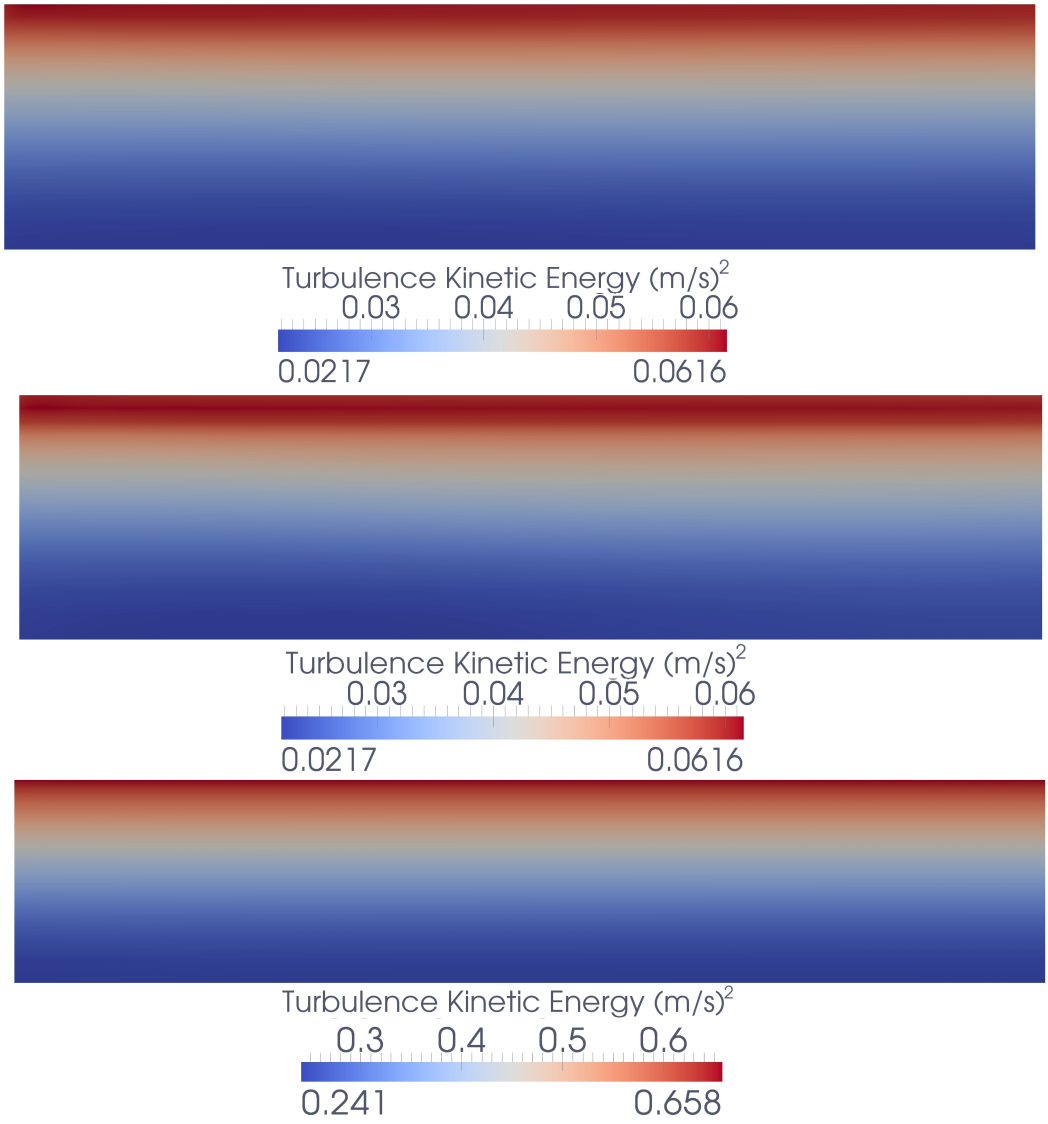

Figure 6.3: Turbulence Kinetic Energy for the coarse mesh Allen and Boelter cases. *Top*: Allen, kEpsilon model. *Middle*: Allen, realizable kEpsilon model. *Bottom*: Boelter, kEpsilon model.

6.6, *Top, Middle*). The resulting enthalpy fields provide the basis for extrapolating wall temperature to compare to Allen and Boelter's experimental measurements and determine simulation accuracy.

Temperature boundary conditions are more complicated than those for velocity. In the thermal viscous sublayer, conduction dominates, and temperature increases linearly [20]. Beyond that, it is necessary to quantify the relationship between mo-

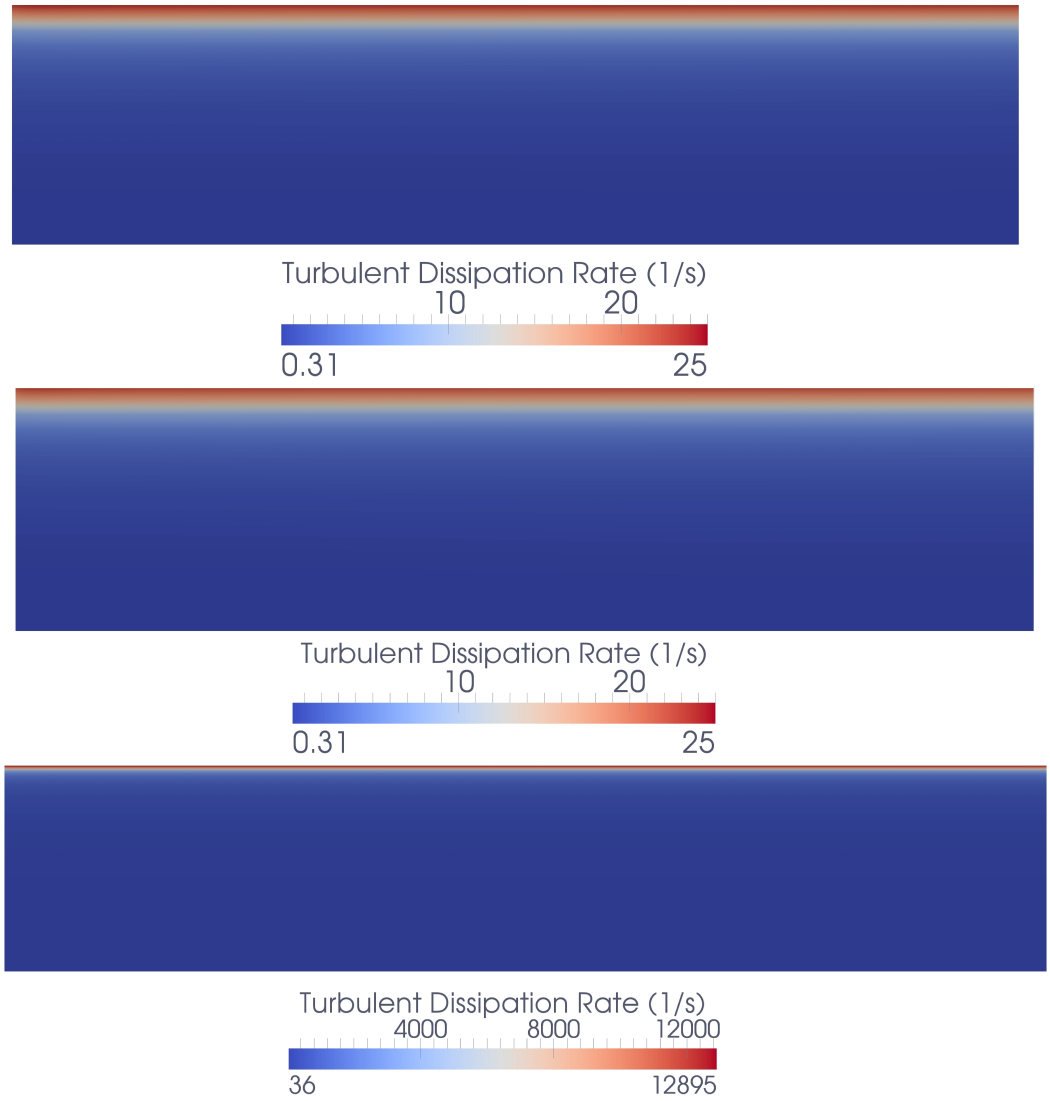

Figure 6.4: Turbulence Dissipation Rate for the coarse mesh Allen and Boelter cases. *Top*: Allen, kEpsilon model. *Middle*: Allen, realizable kEpsilon model. *Bottom*: Boelter, kEpsilon model.

mentum and thermal diffusion. This varies by fluid, and is measured by Prandtl number [48],

$$Pr = \frac{\nu}{\alpha} \tag{6.8}$$

When Prandtl number is much larger than 1 (oil), heat diffuses slowly as compared to momentum, and the thermal boundary layer is much larger than the velocity

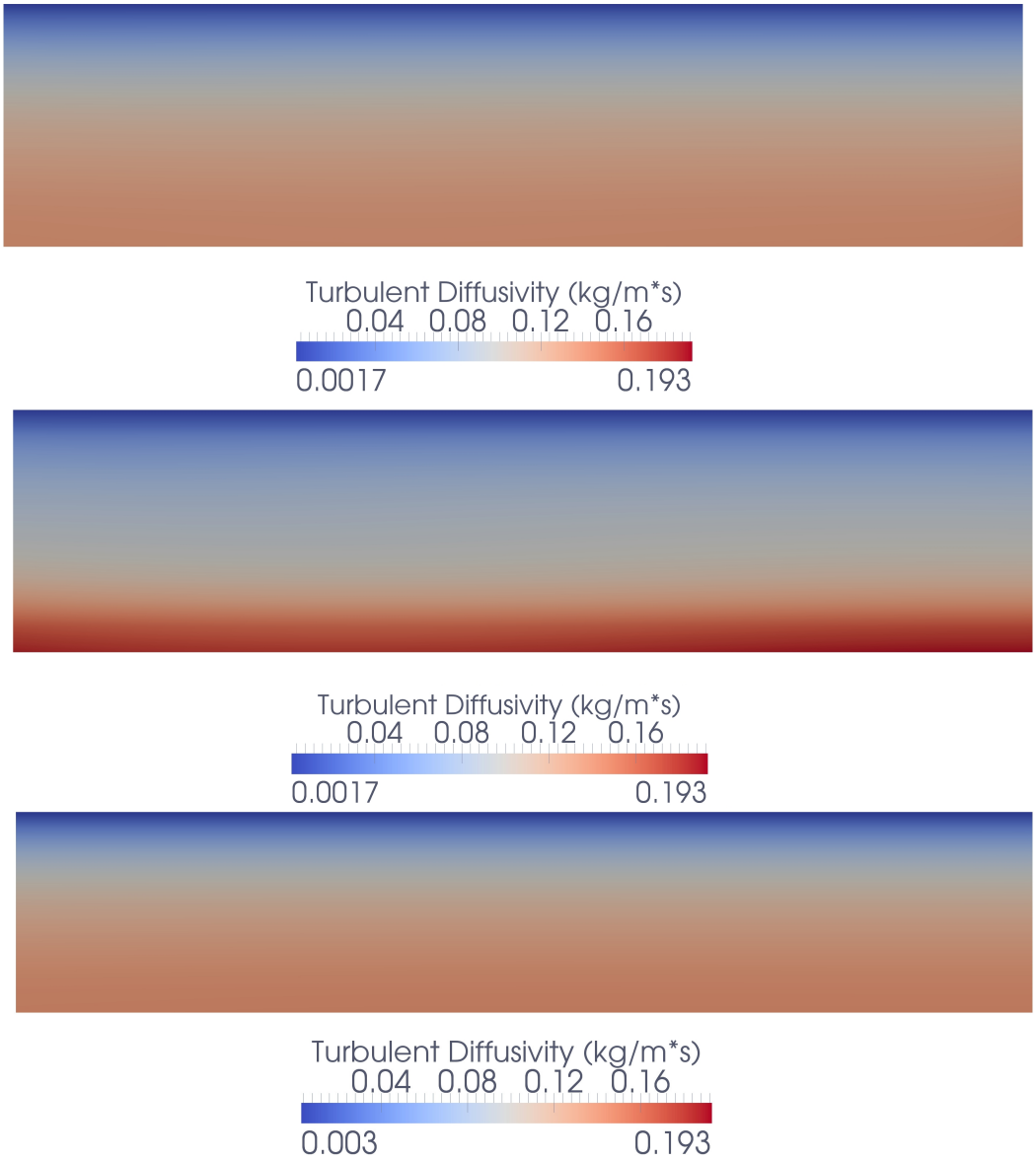

Figure 6.5: Turbulent Diffusivity for the coarse mesh Allen and Boelter cases. *Top*: Allen, kEpsilon model. *Middle*: Allen, realizable kEpsilon model. *Bottom*: Boelter, kEpsilon model.

boundary layer. When much smaller than 1, as is the case for molten metals, thermal diffusivity dominates instead [20]. In the case of water (with $Pr = 7$), the temperature difference between the boundary surface and nearest cell center can be large, even at high resolution. The analagous quantity under turbulent flow conditions is the turbulent Prandtl number, which generally lies in the range of 0.75 to 1.

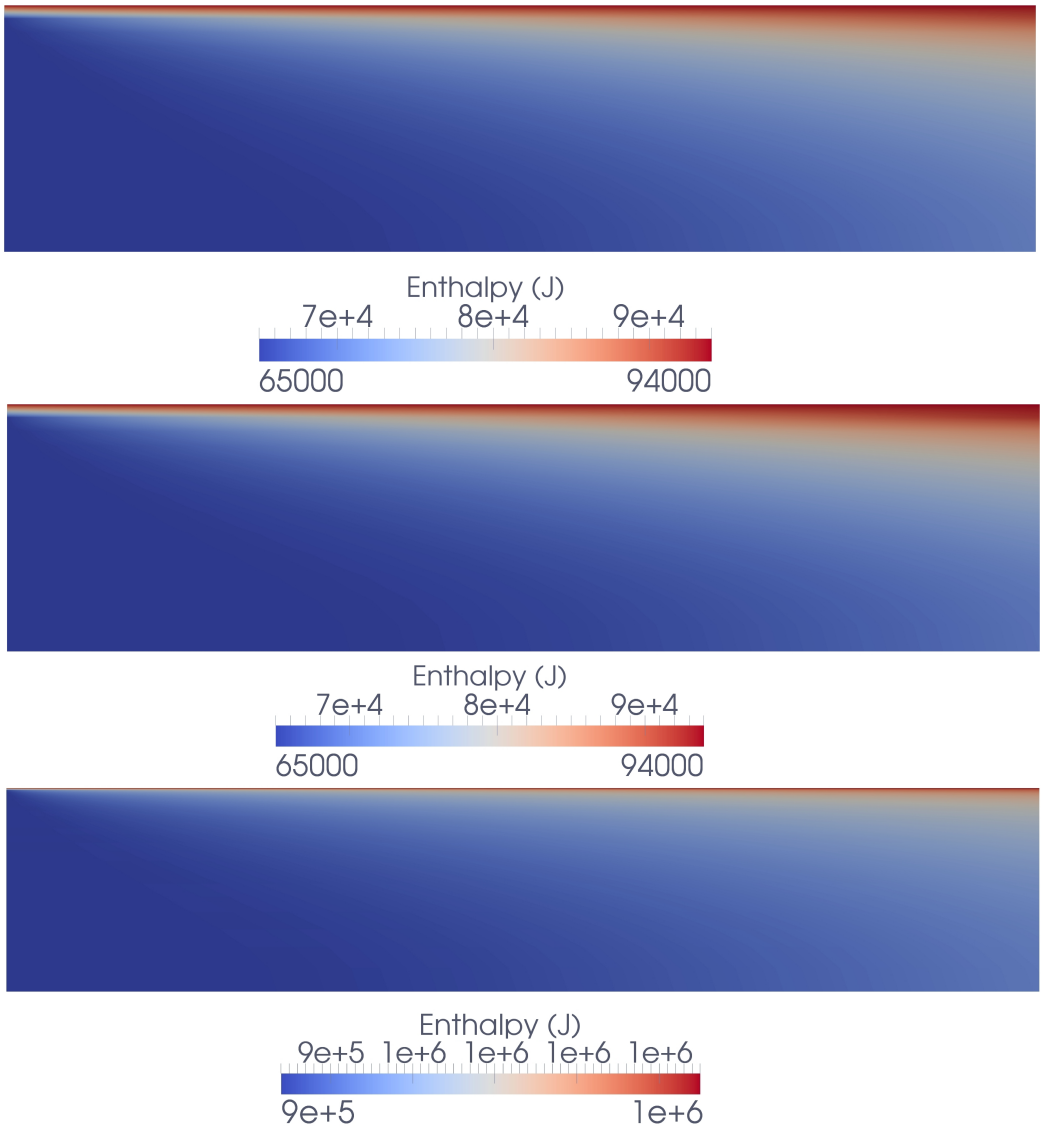

Figure 6.6: Enthalpy for the coarse mesh Allen and Boelter cases. *Top*: Allen, kEpsilon model. *Middle*: Allen, realizable kEpsilon model. *Bottom*: Boelter, kEpsilon model.

There are several relations describing the relationship between the first near-wall node temperature and that of the wall. If the first near-wall node is inside the thermal viscous sublayer (below a y^* of 11.225 [20]), temperature difference is computed as,

$$(T_w - T_p) = \frac{1}{C_p}\left[\frac{q'' Pry^*}{\rho C_\mu^{\frac{1}{4}} k_p^{\frac{1}{2}}} + \frac{1}{2} Pr U_p^2\right] \tag{6.9}$$

where T_p, k_p, and U_p are the near-wall cell center temperature, turbulence kinetic energy, and velocity. The heat flux per unit area is q'', T_w is the wall temperature, and C_μ is a turbulence model constant. If instead the first point is outside the thermal viscous sublayer,

$$(T_w - T_p) = \left[Pr_t \left(\frac{1}{\kappa} ln(Ey^*) + P \right) + \frac{1}{2} \rho \frac{C_\mu^{\frac{1}{4}} k_p^{\frac{1}{2}}}{q''} \left(Pr_t U_p^2 + (Pr - Pr_t) U_c^2 \right) \right] \frac{q''}{\rho C_p C_\mu^{\frac{1}{4}} k_p^{\frac{1}{2}}} \tag{6.10}$$

$$P = 9.24 \left[\left(\frac{Pr}{Pr_t} \right)^{\frac{3}{4}} - 1 \right] [1 + 0.28 e^{-0.007 \frac{Pr}{Pr_t}}] \tag{6.11}$$

where U_c is the velocity where the laminar and logarithmic regions meet, E is the constant 9.793, and Pr_t is turbulent Prandtl number. Further, the temperature in the log-law region can be approximated more simply with the empirical relation [28] [9],

$$(T_w - T_p) = [2.2 ln(y^+) + 13.39 Pr^{\frac{2}{3}} - 5.66] T_\tau \tag{6.12}$$

provided that Prandtl number does not greatly exceed the range of 0.7 to 5.9 [28]. The friction temperature T_τ is given by [9],

$$T_\tau = \frac{q''}{\rho C_p u_\tau} \tag{6.13}$$

and the friction velocity u_τ is [48],

$$u_\tau = \frac{Re_\tau \nu}{\delta} \tag{6.14}$$

where δ is the channel half-width. The friction Reynolds number can be approximated as $Re_\tau = 0.09 Re^{0.88}$ [48].

These relations provide an estimate of wall temperature from near-wall cell temperature, and are more accurate than an inappropriate linear wall-to-bulk temperature profile assumption. However, when applying these relations to the Allen kEpsilon simulation, near-wall cell center temperature difference is highly overpredicted.

When calculated with Equation 6.10 and locally computed kEpsilon turbulence kinetic energy, Re_τ, Prandtl number, laminar viscosity, and thermal conductivity, the bulk-to-wall temperature difference is an average of 22.11K. When using Equation 6.12, that difference is 27.49K. In experiment, the bulk-to-wall temperature difference never exceeds 13.52 K.

The current work deals with what Kays and Crawford [28] call the thermal entry-length problem or turbulent Graetz problem, where fluid enters a heated region at a uniform temperature but with a fully developed velocity profile where heat transfer begins. Solutions are known for thermal boundary layer temperature profile with dimensionless distance to the wall both in the general case [28] and internal tube flow [9] [67]. However, these are calculated under fully developed velocity and thermal conditions. The issue at hand is more complicated and specific.

The current solutions, as given by Kays and Crawford, determine bulk flow mixed mean temperature to wall temperature difference, based on Nusselt number and entrance length. They provide a family of solutions that cover a variety of possible problem formulations. The key detail is the spanwise temperature profile, determined by the dimensionless wall coordinate. Temperature variation is derived from the appropriate differential energy equation for the specific case of a turbulent tube flow [28],

$$\frac{1}{r}\left[r(\alpha+\epsilon_H)\frac{\partial \bar{T}}{\partial r}\right] = \bar{u}\frac{\partial \bar{T}}{\partial x} \tag{6.15}$$

where r is distance to the wall, $\epsilon_H + \alpha$ is the total conductance, and x is the axial distance coordinate. Fluid properties are assumed constant, along with heat rate. The wall coordinate is folded up into an average temperature $\bar{T}$ term as the relation is integrated, and closure is provided through computational eigenvalue analysis and empirical closure constants for the series approximation of several terms. This yields closure and a final relation usable specifically for finding the temperature difference

between the wall and bulk flow but smears the detail associated with near-wall node temperature. While finding the mixed mean bulk temperature and using the given relation to find the surface temperature is feasible, it does not adequately test the accuracy of the implemented enthalpy equation. Further research into closing Equation 6.15 while maintaining an allowance for near-wall distance is necessary before an adequate comparison can be made between the experimental wall temperature and wall-function-closed simulations.

Alternatively, a highly refined mesh could be used, such that the first near-wall node lies within the viscous thermal sublayer. This would require the use of a low-Reynolds number turbulence model instead of wall functions. However, because of the unknown nature of the temperature interpolation relation between the wall and first node, determining the necessary resolution may require trial-and-error or empiricism.

CHAPTER 7

FINE MESH APPROACH: SPECIFIED HEAT FLUX

The following section examines the Allen and Boelter cases with a finely resolved mesh. While the mesh used in both cases is the same, due to the differing scale of the two experiments and the velocities present the Boelter case operates at a y^+ of 24, a non-ideal but reasonable minimum y^+ for the use of wall functions. At this y^+, however, temperature difference is likely to be large between the wall and bulk flow. The calculated enthalpy is presented, but no extrapolation of simulation wall temperature is attempted. In the Allen case, the near-wall cells represent a minimum y^+ of 5. Due to the inaccuracies of using wall functions at low y^+, this translates to a 20% overestimation of near-wall cell velocity in simulation. The computed near-wall enthalpy is reported and compared to the experimental wall temperature, but similarly no extrapolated temperatures are presented. Both experimental cases were simulated using wall functions, on a mesh with a minimum y^+ of 5 for the Allen case, and y^+ of 24 for the Boelter case. In each case, for turbulence kinetic energy the compressible kqRWallFunction was used, with the compressible epsilonWallFunction for dissipation. No-slip was used for the velocity wall boundary condition.

7.1 Results

The fine resolution mesh is a 5° wedge, one cell thick (Fig. 7.1), made up of approximately 104,000 cells (102,000 hexahedra, 2000 prisms). The mesh is axisymmetric about the center axis of the pipe and of L/D 30. Because of the structured nature of the mesh, every cell face is either in the direction of the flow or perfectly nor-

mal to it. As such, the OpenFOAM utility checkMesh reported a non-orthogonality of zero. The maximum skewedness was 0.333, and the maximum aspect ratio was 3.783, both of which are reasonable for stability.

Figure 7.1: Side-view of computational domain. Contains 104,000 cells in total.

7.1.1 kEpsilon

The results obtained with kEpsilon are plotted in Figure 7.2 against the experimental outcome. The figure shows normalized heat transfer coefficient values, with each locally calculated h divided by the reference h_{ref} (the average h across the last 6 pipe diameters). The normalized heat transfer coefficient was an average of 2.75% higher than Allen's experimental values, across the entire data set (Figure 7.2). This error rises to 7.76% when considering only the first six points from the inlet. This is perhaps a better gauge of model performance, as the normalized curve always approaches unity due to its normalization factor, skewing the average. The model predicts the highest near-wall α_t of the three models, yielding the lowest wall enthalpy values as more heat is convected towards the center of the flow. Further, kEpsilon slightly overpredicts the gradient of the wall enthalpy rise early in the pipe.

Turbulent diffusivity α_t is shown in Figure 7.3. Turbulent diffusivity is distributed in a smoothly increasing gradient from the wall to the centerline (Figure 7.3), where

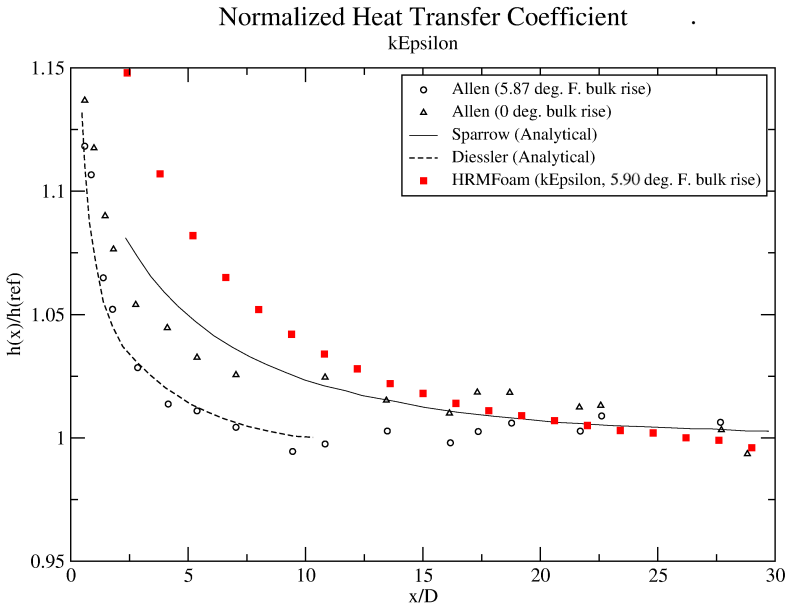

x/D	h(x)/h(ref)
1	1.240
2.4	1.148
3.8	1.107
5.2	1.082
6.6	1.065
8	1.052
9.4	1.042
10.8	1.034
12.2	1.028
13.6	1.022
15	1.018
16.4	1.014
17.8	1.011
19.2	1.009
20.6	1.007
22	1.005
23.4	1.003
24.8	1.002
26.2	1.000
27.6	0.999
29	0.996

Figure 7.2: Normalized heat transfer coefficient vs. axial pipe location, calculated using HRMFoam with kEpsilon. Local heat transfer coefficient values are normalized by the average heat transfer coefficient over the last 6 diameters of pipe length. *(Right)* HRMFoam results tabulated by x/D, axial pipe length measured in pipe diameters.

it reaches a maximum of 0.164 $\frac{kg}{ms}$. This diffusivity causes kEpsilon to predict a bulk temperature rise of 5.901°F, 0.53% above the experimental rise of 5.87°F. The outlet temperature predicted by kEpsilon was 65.557°F, 0.047% above Allen's outlet temperature.

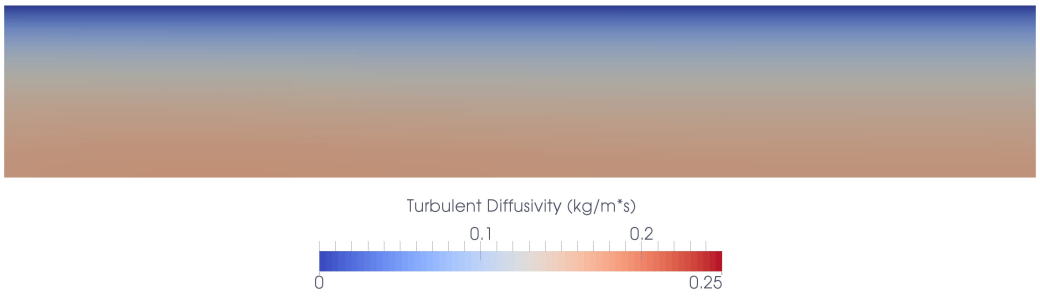

Figure 7.3: Turbulent diffusivity for the kEpsilon turbulence model. Note that each α_t plot uses the same scale for comparison. kEpsilon predicts a maximum of 0.164 $\frac{kg}{ms}$.

7.1.2 Realizable kEpsilon

The heat transfer coefficient data from the realizable kEpsilon model are plotted in Figure 7.4. The HRMFoam prediction data are 3.57% from the experimental values on average, and 9.97% in the first six curve points. The bulk rise was predicted as 5.867°F, 0.05% below the observed bulk rise. This translates to a final temperature of 65.523°F, 0.005% below Allen's observed temperature. Realizable kEpsilon better predicts the bulk outlet temperature and enthalpy of the wall as a whole, but exaggerates the difference between the inlet and outlet wall enthalpies as compared to kEpsilon. This raises the reference enthalpy, which causes the heat transfer coefficient curve to appear less accurate. The model predicts larger values of turbulent diffusivity in a more focused region about the centerline (Figure 7.5).

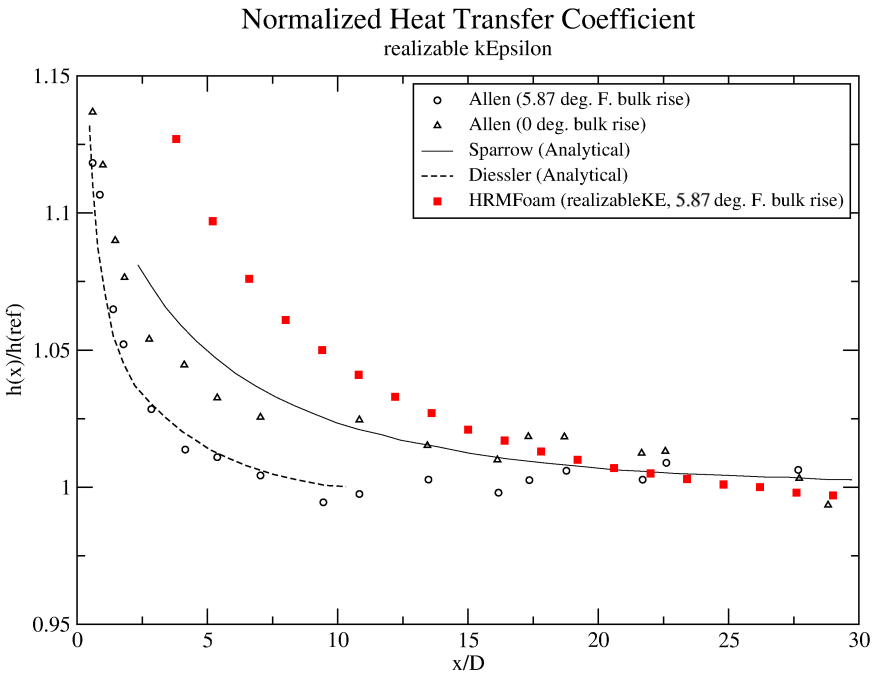

x/D	h(x)/h(ref)
1	1.291
2.4	1.176
3.8	1.127
5.2	1.097
6.6	1.076
8	1.061
9.4	1.050
10.8	1.041
12.2	1.033
13.6	1.027
15	1.021
16.4	1.017
17.8	1.013
19.2	1.010
20.6	1.007
22	1.005
23.4	1.003
24.8	1.001
26.2	1.000
27.6	0.998
29	0.997

Figure 7.4: Normalized heat transfer coefficient vs. axial pipe location measured in diameters, calculated using HRMFoam with Realizable kEpsilon.

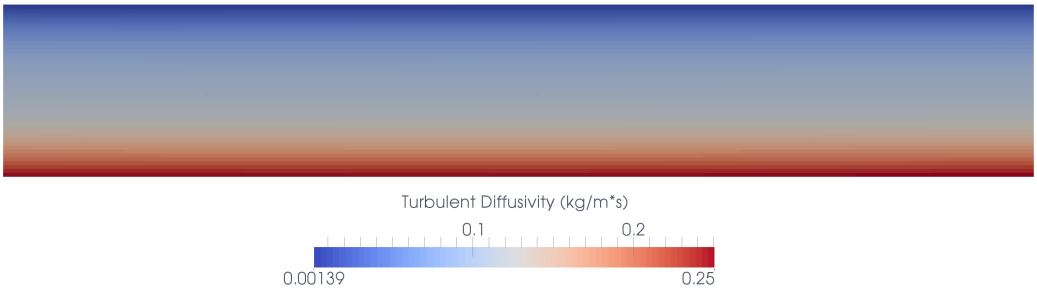

Figure 7.5: Turbulent diffusivity for the Realizable kEpsilon turbulence model. Realizable kEpsilon predicts the highest peak α_t values, about the centerline.

7.1.3 Spalart-Allmaras

The model reproduced the heat transfer coefficient curve (Figure 7.6) within 0.63% for all points, or 2.9% for the first six, replicating the shape of the curve more faithfully than either of the other models. It also predicted the lowest α_t values of the three (Figure 7.7), yielding the highest wall enthalpy values close to the pipe inlet and the closest match to Allen's wall temperature data. The experimental bulk rise was predicted to within 1.17%, at 5.939 °F, and a final temperature of 65.595°F (0.11% above the experimental value).

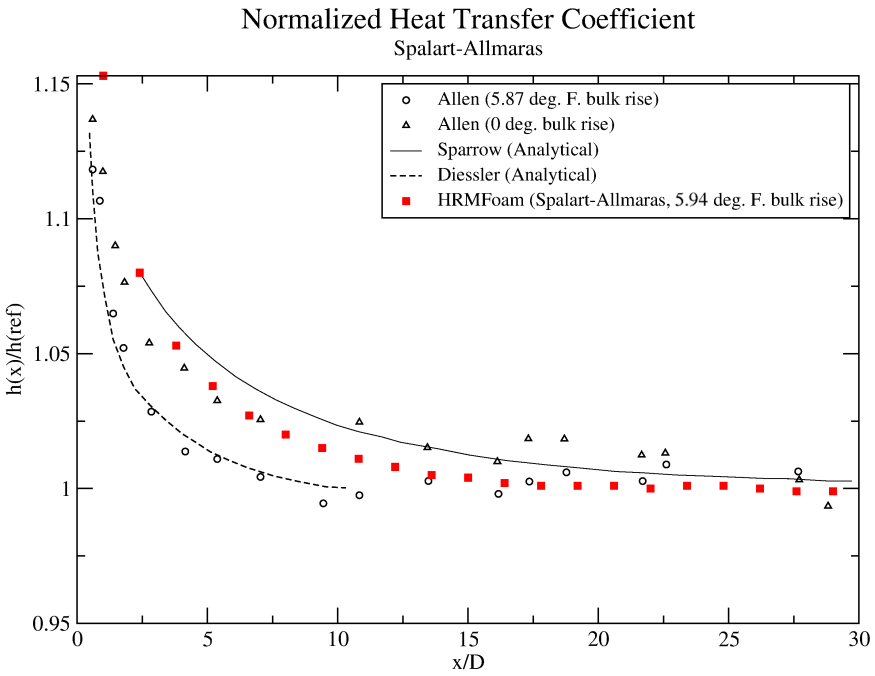

x/D	h(x)/h(ref)
1	1.153
2.4	1.080
3.8	1.053
5.2	1.038
6.6	1.027
8	1.020
9.4	1.015
10.8	1.011
12.2	1.008
13.6	1.005
15	1.004
16.4	1.002
17.8	1.001
19.2	1.001
20.6	1.001
22	1.000
23.4	1.001
24.8	1.001
26.2	1.000
27.6	0.999
29	0.999

Figure 7.6: Normalized heat transfer coefficient vs. axial pipe location measured in diameters, calculated using HRMFoam with Spalart-Allmaras.

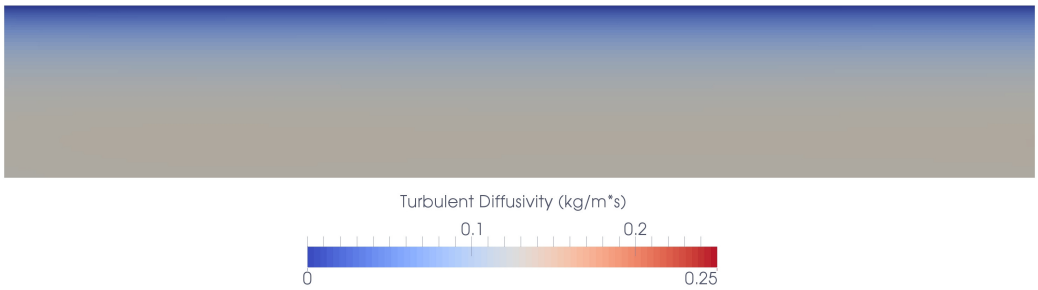

Figure 7.7: Turbulent diffusivity for Spalart-Allmaras. Because α_t is more conservatively estimated than in the kEpsilon models, the more heat remain in the near-wall region.

7.2 Near-wall Enthalpy Curves

Figure 7.8 shows a comparison of the near-wall enthalpy values for each turbulence model, plotted against Allen's wall enthalpy data. Allen's enthalpy values were back-calculated from the known temperature difference at the control point of 24°F, and the published normalized heat transfer coefficient curve.

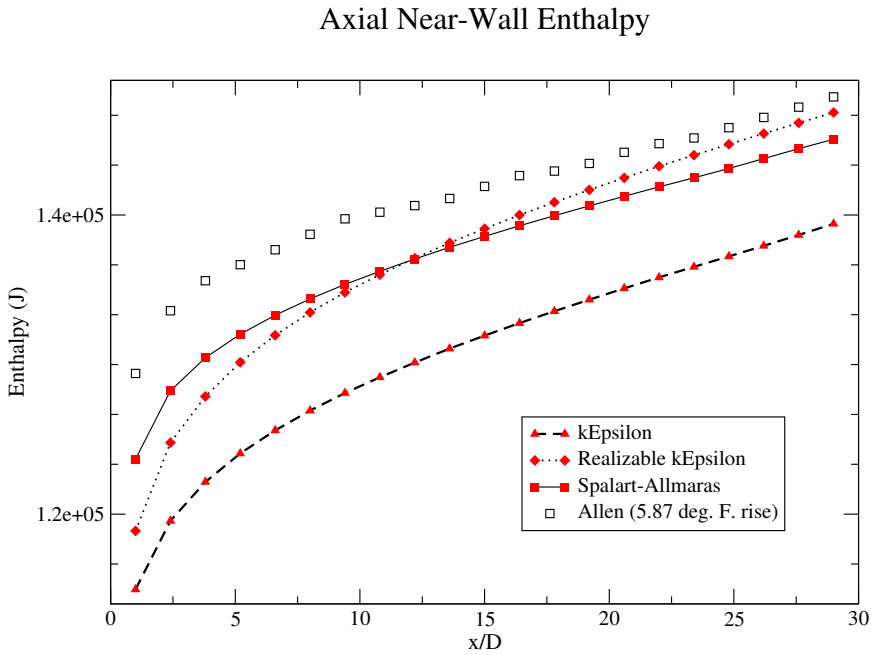

Figure 7.8: Axial Near-Wall Enthalpy, Allen. The non-dimensional axial distance from the pipe inlet is x/D, where D is the pipe diameter. Allen's wall enthalpy values calculated from the heat transfer coefficient and known temperature difference at the control point. Data from Allen [1].

It is interesting to note the differences in predicted near-wall temperature between the three models. kEpsilon predicted the largest near-wall turbulent diffusivity, and as such reports the lowest enthalpy values close to the wall. Although Realizable kEpsilon predicts the highest centerline turbulent diffusivity of the three turbulence models, it predicts lower values near the wall, producing higher near-wall enthalpy values than kEpsilon. While it provides a more accurate estimate of wall enthalpy, the Realizable kEpsilon does overestimate the difference in near-wall cell enthalpy between the inlet and outlet. It does, however, approach the enthalpy of the wall

nearest the outlet most accurately. Spalart-Allmaras predicts the trend of the experimental curve very accurately, while also returning the closest enthalpy values near the pipe inlet. Low values of α_t are predicted, and do not convect away as much of the entering heat flux as either kEpsilon or Realizable kEpsilon.

7.3 Conclusions

It is clear that the transport of enthalpy is dependent upon α_t prediction. Because kEpsilon tends to overpredict turbulence quantities, especially in regions of favorable pressure gradient, it disperses enthalpy throughout the flow. While all three models predict near-identical exit temperature and total heat added, larger α_t prediction translates to a colder wall and a warmer bulk flow. Spalart-Allmaras, with its conservative estimate of α_t, best predicts the experimental heat transfer coefficient curve shape and wall temperature data. Realizable kEpsilon best predicts the outlet temperature.

CHAPTER 8

FINE MESH APPROACH: SPECIFIED SURFACE TEMPERATURE

Boelter's experiment was also modeled using the fine resolution grid. While Boelter included temperature measurements for his entire pipe length of 100 diameters, only the first 8.34 inches (0.211 meters) of the heated region are included in simulation, as in the coarse mesh case. The mesh is the same 104,000 cell, 5° wedge mesh used in the fine resolution Allen case. To match the Boelter experiment, the mesh is scaled to model the L/D 36.3 region of pipe, 0.2289 inches (0.0058 m) in diameter.

In the Boelter fine mesh runs, the specified surface temperature boundary condition is used. Boelter recorded surface temperature data throughout the length of the pipe, providing an opportunity for a more rigorous validation method. Under specified heat flux conditions, the amount of heat entering the domain via enthalpy gradient is sensitive only to turbulent diffusivity. With specified surface temperature, both the turbulent diffusivity and heat flux vary as the difference in temperature between the wall and flow drives total enthalpy addition. Outlet temperature is therefore more sensitive to prediction accuracy under specified surface temperature conditions, yielding more stringent validation.

8.1 Results

Velocity, pressure, and vapor fraction can be seen in Figure 8.1. The velocity profile and vapor fraction remain constant throughout the pipe length. Due to the no-slip walls velocity boundary condition, pressure drops linearly by 0.1 MPa between

the inlet and outlet. The bulk fluid is raised 38 °F to 445.573°F, 16.7% above Boelter's experimental temperature rise to 440.13°F. The experimental mass flow rate is matched within 0.001%. The kEpsilon model predicts an α_t that increases from the wall to the centerline quickly (Figure 8.2).

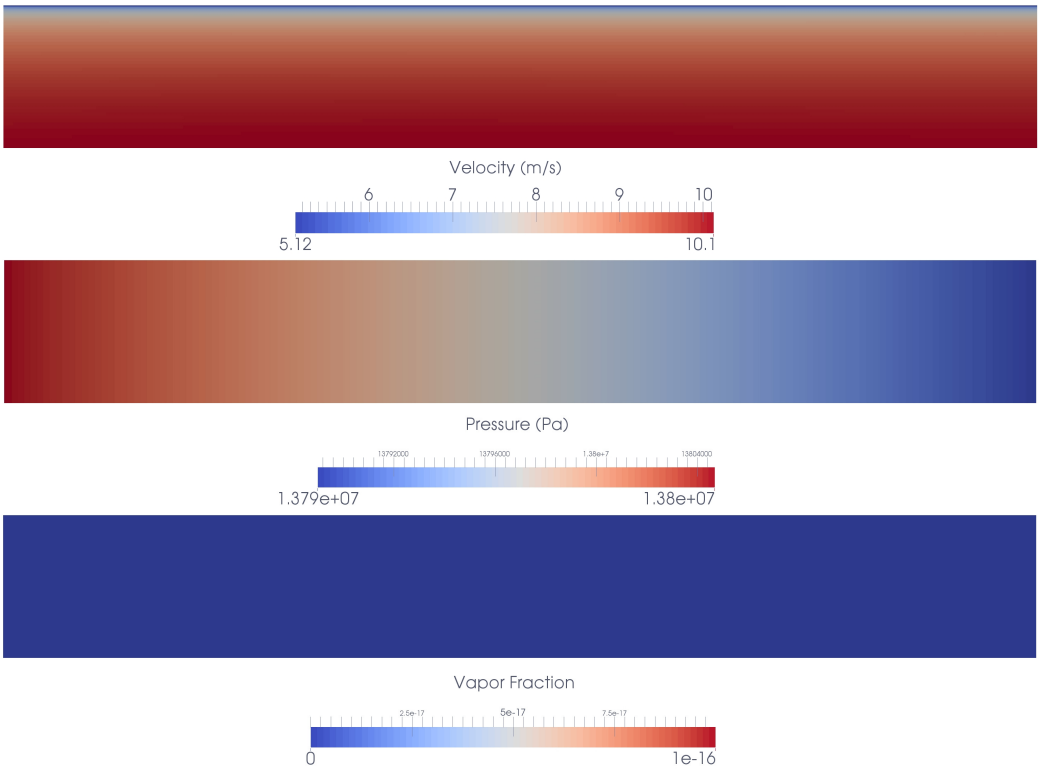

Figure 8.1: Boelter simulation velocity, pressure, and vapor fraction.

At the experimental Reynolds number of 336,000, turbulence causes fluctuations similar to those of the Allen case, at approximately 3.2% of mean flow velocity. However, the predicted α_t (Figure 8.2) is approximately 33% less than that of the Allen case run with the same turbulence model. While the Boelter case has a much higher velocity and therefore larger turbulent kinetic energy, in this case the disparity in length scales has a much larger effect on turbulent dissipation, overshadowing thermal diffusivity's k^2 dependence.

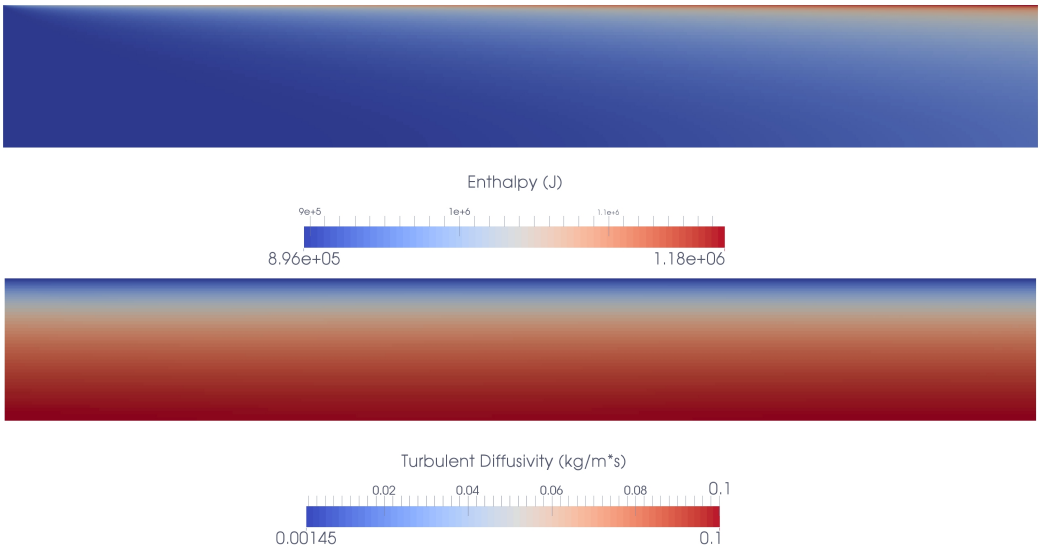

Figure 8.2: Boelter simulation enthalpy and turbulent diffusivity

CHAPTER 9

MODULE INTERACTION TESTING

While the enthalpy transport model produces accurate results in isolation, its interaction with other aspects of the code should be explored. The transport of enthalpy was also tested in conjunction with compressibility, beginning with single-phase flow. A pressure-driven nozzle simulation was conducted using a diesel-scale injector geometry, with a perfectly sharp inlet orifice. The L/D 4 nozzle was modeled as a 5° wedge, using 24,000 cells (Figure 9.1). The upstream pressure was set to 10 MPa, with 5 MPa at the downstream orifice, and a vapor fraction of zero at the inlet.

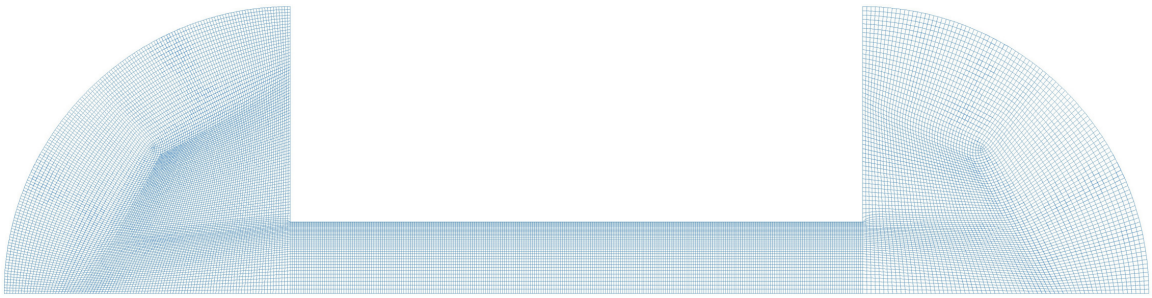

Figure 9.1: Mesh used to test interaction of compressibility and heat transfer in HRMFoam. 24,000 cells, 5°wedge.

Fluid entering the domain was 286K (at an enthalpy of 65000 J). Enthalpy was added to the domain through a heatFlux boundary condition imposed at the wall, imparting 6.24E7 watts/m^2. The outlet enthalpy boundary condition was inletOutlet, to ensure entrained fluid was a reasonable temperature. Fluid entrained by the exiting spray entered at 286K. kEpsilon was the turbulence model used.

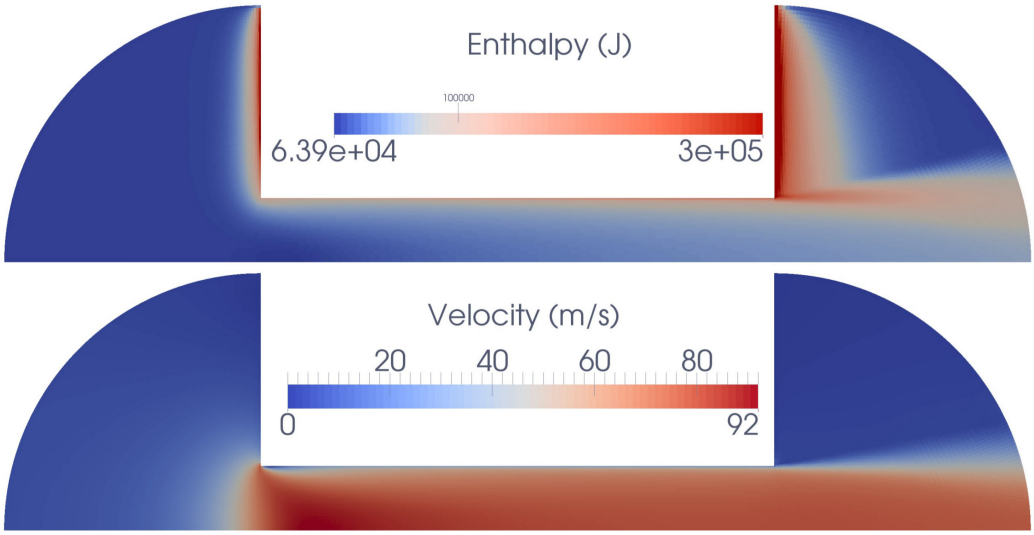

Figure 9.2: Enthalpy and velocity for single-phase compressible heat transfer. *(Top)* Velocity in the throat is much higher than the Allen or Boelter cases.

Upon reaching steady state, the distribution of enthalpy was found to be heavily concentrated in the near-wall region of the inlet and outlet plena (Figure 9.2). Velocity is extremely low in that region, causing fluid near the wall to clear from the plena very slowly. This large residence time allows for the fluid there to absorb large amounts of heat. The outlet plenum is much higher temperature than anywhere else in the domain; Figure 9.2 is scaled to show the gradations in the distribution of enthalpy. Maximum enthalpy is 7.66E5 J on the outlet plenum wall.

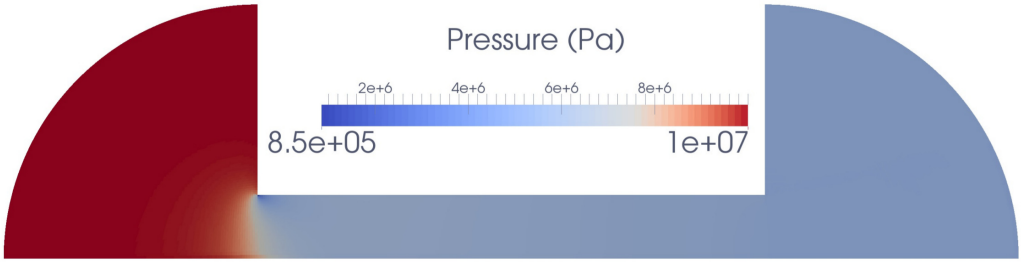

Figure 9.3: Pressure for single-phase compressible heat transfer. Note the presence of the vena contracta.

Despite the large enthalpy addition from the wall, the fluid remains single-phase due to the high pressure throughout the domain (Figure 9.3). Pressure is lowest in vena contracta, at the inlet corner. Because velocity peaks there as well, turbulent diffusivity is large in the throat (Figure 9.4). This is almost certainly an overprediction of α_t, as a favorable large pressure gradient tends to suppress turbulence, which kEpsilon does not suggest.

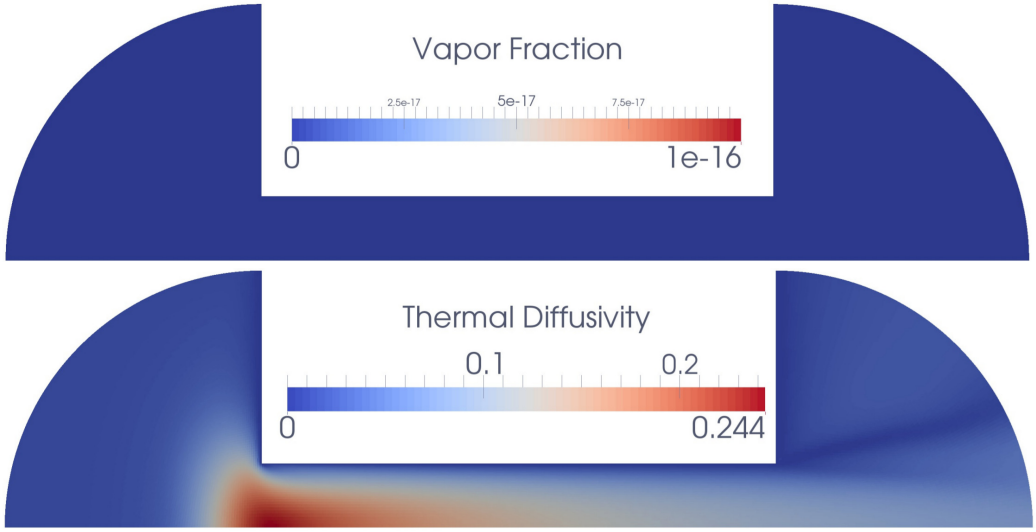

Figure 9.4: Vapor fraction and turbulent diffusivity for single-phase compressible heat transfer.

CHAPTER 10

CONCLUSIONS AND FUTURE WORK

The HRMFoam vaporization model was combined with a transport equation for enthalpy. With the energy equation implemented, experimentally measured heat flux and wall temperature curves were applied to a modeled pipe geometry. Validation was then conducted through two experimental single-phase flow cases using the specified heat flux and specified surface temperature boundary conditions. In the Allen case, all three turbulence models predicted outlet temperatures that were within 0.1% of the experimental outlet temperature of 65.53°F, from a bulk temperature rise predicted within 1.17%. HRMFoam predicted a bulk rise of 38°F in the Boelter case, 16.7% above the experimental 32.56°F. Heat transfer coefficients for the Allen case were calculated to within an average of 2.9% (for the first six points), with the assumption that near-wall and wall surface temperature were approximately equal. However, more research needs to occur before the model can be deemed quantitatively accurate.

Further analysis should more deeply explore the relationship between dimensionless wall distance and temperature in developing thermal boundary layers under fully developed hydrodynamic conditions. A model relating thermal entry length, non-dimensional wall distance, and temperature would allow for more accurate assessment of the model's performance, and is necessary before the experimental results can be compared to simulation output with minimal use of approximating assumptions. This would require integrating Equation 6.15 while leaving the wall coordinate intact, and possibly closing the relation with eigenvalue analysis and empirical methods similar to Kays and Crawford [28]. With a firmer understanding of that temperature rela-

tionship, both coarse grid simulations with wall functions and fine grid simulations using a low Reynolds number model should be compared. Near-wall temperature could then be extrapolated to assess simulation wall temperature.

With the core model validated, basic stress testing should be conducted with large velocities, larger boundary heat flux, compressibility, and non-condensible gas. Expansion to two-phase flow, and eventually fully 3D flow would be logical next steps as well. Modeling in full 3D would allow for the use of LES, and the removal of the axisymmetric assumption.

APPENDIX

ENERGY TRANSPORT EQUATION IMPLIMENTATION

Included here is the raw C++ code of hEqn.H, the implimentation of the energy transport equation in HRMFoam.

```
{
  volScalarField cpMix = (1-x)*(1-y)*cpL + x*(1-y)*cpV + y*Model.cpGas();

  volScalarField alphaMix = Model.K()/(cpMix);

  if (U.db().foundObject<volScalarField>("alphat"))
    {
      const volScalarField& alphat = U.db().lookupObject<volScalarField>("alphat");
      alphaMix += alphat;
    }

  volTensorField gradU = fvc::grad(U);

  fvScalarMatrix hEqn
    (
     fvm::ddt(rho,h)
     + fvm::div(phi,h,"div(phi,h)")
     ==
     fvc::ddt(p)
     + (U & fvc::grad(p))
     + fvm::laplacian(alphaMix,h) //turbulent enthalpy dispersion
     + turbulence->mut()*((gradU + gradU.T()) && gradU) // viscous dissipation
     );


  hEqn.solve();

  fvc::makeRelative(phiv, U);

}
```

BIBLIOGRAPHY

[1] Allen, R. W., and Eckert, E. R. G. Friction and heat-transfer measurements to turbulent pipe flow of water (pr = 7 and 8) at uniform wall heat flux. *Journal of Heat Transfer* (August 1964), 301–310.

[2] Amit Saxena, ESI CFD Senior Applications Engineer. Guidelines for specification of turbulence at inflow boundaries. `http://support.esi-cfd.com/esi-users/turb_parameters/`. Accessed: 4/14/2014.

[3] Bergwerk, W. Flow pattern in diesel nozzle spray holes. *Proceedings of the Institution of Mechanical Engineers 173*, 1 (June 1959), 600–655.

[4] Bilicki, Z., and Kestin, J. Numerical study of two-dimensional structure in critical steam-water two-phase flow. *Proc. R. Soc. Lond. 428* (1990), 379–397.

[5] Bliss, J., Schmidt, D., Smith, J., and Neroorkar, K. Model constant optimization using an ensemble of experimental data. *SAE Technical Paper*, 2012-01-0131 (April 2012).

[6] Boelter, L. M. K., and Staff. Studies in boiling heat transfer. *AEC Research Contract No. AT-11-1-Gen-9* (March 1951). Final Report.

[7] Boure, J. A., Fritte, A. A., Giot, M. M., and Reocreux, M. L. Highlights of two-phase critical flow: On the links between maximum flow rates, sonic velocities, propagation and transfer phenomena in single and two-phase flows. *International Journal of Multiphase Flow 3* (July 1976), 1–22.

[8] Boure, J. A., and Reocreux, M. General equations of two-phase flows. *All-Union Heat and Mass Transfer Conf., Minsk* (1972).

[9] Bredberg, J., Peng, S-H., and Davidson, L. On the wall boundary condition for computing turbulent heat transfer with k-omega models. *ASME 366*, 5 (2000), 243–250.

[10] Brennen, Christopher E. An introduction to cavitation fundamentals. *WIMRC FORUM 2011: Cavitation: Turbo-machinery and Medical Applications* (July 2011), 1–17.

[11] Corradini, Micheal L. Fundamentals of multiphase flow; pool boiling. `http://wins.engr.wisc.edu/teaching/mpfBook/main.html`, August 1997. Accessed: 10/04/2012.

[12] D. P. Schmidt, M. L. Corradini. The internal flow of diesel fuel injector nozzles: A review. *Int J Engine Research 2*, 1 (February 2001), 1–22.

[13] Defraeye, Thijs, Blocken, Bert, and Carmeliet, Jan. Cfd analysis of convective heat transfer at the surfaces of a cube immersed in a turbulent boundary layer. *International Journal of Heat and Mass Transfer 53*, 1-3 (2010), 297–308.

[14] Deissler, R. G. Analysis of turblent heat transfer, mass transfer, and friction in smooth tubes at high prandtl and schmidt numbers. *NACA TN 3145 1210* (1955), 69–82.

[15] Downar-Zapolski, P., Bilicki, Z., Bolle, L., and Franco, J. The non-equilibrium relaxation model for one-dimensional flashing liquid flow. *Int. J. Multiphase Flow 22*, 3 (1996), 473–483.

[16] Fauske, H. The discharge of saturated water through tubes. *Chemical Engineering Progress Symposium Series* (1965), 210–216.

[17] Fauske, H. K. Contribution to the theory of two-phase, one-component critical flow. *U.S. A.E.C. Research and Development Report*, TID-4500 (October 1962).

[18] Ferziger, J.H., and Peric, M. *Computational Methods for Fluid Dynamics*. Springer, 1999.

[19] Fluent, Inc. The standard, rng, and realizable k-epsilon models. `http://combust.hit.edu.cn:8080/fluent/fluent60_help/html/ug/node406.htm`, November 2001. Accessed: 4/14/2014.

[20] Fluent, Inc. *Ansys Fluent Theory Guide*. 2011. Release 14.0.

[21] Gelalles, A. G. Coefficients of discharge of fuel injection nozzles for compression-ignition engines. *NACA Technical Memo*, 373 (January 1931), 1–13.

[22] Hendricks, R.C., Graham, R. W., Hsu, Y. Y., and Friedman, R. Experimental heat transfer and pressure drop of hydrogen flowing through a heated tube. NASA Technical Note D-765.

[23] Henry, R. E., and Fauske, H.K. The two-phase critical flow of one-component mixtures in nozzles, orifices and short tubes. *Journal of Heat Transfer 93*, 2 (May 1971), 179–187.

[24] Hiroyasu, H., Arai, M., and Shimizu, M. Break-up length of a liquid jet and internal flow in a nozzle. *ICLASS* (July 1991), 275–282.

[25] Incropera, Frank P., and DeWitt, David P. *Fundamentals of Heat and Mass Transfer*, 4th ed. John Wiley and Sons, 1996.

[26] James, A. J. *Flow through a long orifice*. Undergraduate thesis, Nottingham University, 1961.

[27] Kato, H., Kayano, H., and Kageyama, Y. A consideration of thermal effect on cavitation bubble growth. *ASME Cavitation and Multiphase Flow*, 194 (July 2011), 7–14.

[28] Kays, W., Crawford, M., and Weigand, B. *Convective Heat and Mass Transfer*, 4 ed. McGraw Hill, 2005.

[29] Kays, W. M., and Crawford, M. E. *Convective Heat and Mass Transfer*, 3rd ed. January 1993.

[30] Knox-Kelecy, A. *Turbulent flow in a scale model of diesel fuel injector nozzle hole*. PhD thesis, University of Wisconsin, 1992.

[31] Kubota, A., Kato, H., and Yamaguchi, H. Finite difference analysis of unsteady cavitation on a two-dimensional hydrofoil. *Proc. of the 5th Int. Conf. on Numerical Ship Hydrodynamics, Hiroshima* (September 1989), 667–683.

[32] Larsson, Jonas. *Numerical Simulation of Turbulent Flows for Turbine Blade Heat Transfer Applications*. PhD thesis, Chalmers University, 1998.

[33] Lee, Chang Sik, Park, Su Han, and Suh, Hyun Kyu. Effect of cavitating flow on the flow and fuel atomization characteristics of biodiesel and diesel fuels. *American Chemical Society Energy and Fuels 22*, 1 (2007), 605–613.

[34] Lee, Poh-Seng, Garimella, Suresh V., and Liu, Dong. Investigation of heat transfer in rectangular microchannels. *International Journal of Heat and Mass Transfer 48*, 9 (2005), 1688–1704.

[35] Lichtarowicz, A., Duggins, R. K., and Markland, E. Discharge coefficients for incompressible non-cavitating flow through long orifices. *Journal Mechanical Engineering Science 7*, 2 (1965), 210–219.

[36] Ljung, Lennart. *System Identification: Theory for the User*, 2nd ed. Prentice-Hall Inc., 1999.

[37] Minato, Akihiko, Takamori, Kazuhide, and Susuki, Akira. Numerical study of two-dimensional structure in critical steam-water two-phase flow. *Journal of Nuclear Science and Technology 32*, 5 (1995), 464–475.

[38] Mitroglou, N., Gavaises, M., Nouri, J. M., and Arcomanis, C. Cavitation inside enlarged and real-size fully transparent injector nozzles and its effect on near nozzle spray formation. *DIPSI Workshop 2011 on Droplet Impact Phenomena and Spray Investigation* (May 2011), 33–45.

[39] Miyatake, O., Tanaka, I., and Lior, N. A simple universal equation for bubble growth in pure liquids and binary solutions with a non-volatile solute. *Int. J. Heat Mass Transfer 40*, 7 (1997), 1577–1584.

[40] Moody, F. J. Maximum flow rate of a single component, two-phase mixture. *Journal of Heat Transfer 87*, 1 (February 1965), 134–141.

[41] Morgan, J. G. D. *Flow through long orifice at low Reynolds number*. Undergraduate thesis, Nottingham University, 1963.

[42] Neeroorkar, K., Shields, B., Grover, R., Plazas, A. H., and Schmidt, D. Application of the homogenous relaxation model to simulating cavitating flow of a diesel fuel. *SAE Paper*, 2012-01-1269 (2012).

[43] Numachi, F., Yamabe, M., and Oba, R. Cavitation effect on the discharge coefficient of the sharp-edged orifice plate. *Journal of Basic Engineering 82*, 1 (March 1960), 1–6.

[44] Nurick, W. H. Orifice cavitation and its effect on spray mixing. *Journal of Fluids Engineering 98*, 4 (December 1976), 681–687.

[45] Ohrn, T. R., Senser, D. W., and Lefbvre, A. H. Geometric effects on spray cone angle for plain-orifice atomizers. *Atomization and Sprays 3*, 1 (1991).

[46] Pasinlioglu, Senay, Delale, Can F., and Schnerr, Gunter H. On the temporal stability of steady-state quasi-1d bubbly cavitating nozzle flow solutions. *IMA Journal of Applied Mathematics*, 74 (2009), 230–249.

[47] Plesset, S. The dynamics of cavitation bubbles. *Journal of Applied Mechanics 16* (September 1949), 277 – 282.

[48] Pope, Stephen B. *Turbulent Flows*. Cambridge University Press, Cambridge, UK, 2000.

[49] Rayleigh, Lord. On the pressure developed in a liquid during the collapse of a spherical cavity. *Philosophical Magazine 34* (1917), 94–98.

[50] Reitz, R. D. *Atomization and other breakup regimes of a liquid jet*. PhD thesis, Princeton Univ., NJ., 1978.

[51] Reitz, Rolf D. A photographic study of flash-boiling atomization. *Aerosol Science and Technology 12* (1990), 561–569.

[52] Reocreux, M. *Contribution a l'etude des debits critiques en ecoulement diphasique eauvapeur*. PhD thesis, Universite Scientifique et Medicale de Grenoble, France, 1974.

[53] Richter, H. J. Separated two-phase flow model: Application to critical two-phase flow. *International Journal of Multiphase Flow 9*, 5 (January 1983), 511–530.

[54] Sanderson, E. W. *Flow through long orifices*. Undergraduate thesis, Nottingham University, 1962.

[55] Schmidt, David P., Rutland, Christopher J., and Corradini, M. L. A numerical study of cavitating flow through various nozzle shapes. *Analysis*, 2013 (August 1997).

[56] Schmidt, D.P. *Cavitation in Diesel Fuel Injector Nozzles*. PhD thesis, The University of Wisconsin-Madison, 1997.

[57] Singhal, Ashok K., Athavale, Mahesh M., Li, Huiying, and Jiang, Yu. Mathematical basis and validation of the full cavitation model. *Journal of Fluids Engineering 124*, 3 (September 2002), 617–624.

[58] Soteriou, C, Andrews, R., and Smith, M. Direct injection diesel sprays and the effect of cavitation and hyrdaulic flip on atomization. *SAE technical paper*, 950080 (1995).

[59] Sparrow, E. M., Hallman, T.M., and Siegel, R. Turbulent heat transfer in the thermal entrance region of a pipe with uniform heat flux. *Appl. Sci. Res. 7*, 1 (1957), 37–52. Section A.

[60] Tamaki, Nobushige, Shimizu, M., Nishida, K., and H, Hiroyasu. Effects of cavitation and internal flow on atomization of a liquid jet. *Atomization and Sprays 8*, 2 (1998).

[61] Theodorakakos, Andreas, Mitroglou, Nicholas, and Gavaises, Manolis. Flow pattern in diesel nozzle spray holes. *8th National Symposium on Cavitation* (August 2012).

[62] Torres, Alejandro Hernan Plazas. *Modelado Unidimensional De Inyectores Common-Rail Diesel*. PhD thesis, Universidad Politecnica de Valencia, 2005.

[63] Vernier, P., and Delhaye, J. M. General two-phase flow equations applied to the thermohydrodynamics of boiling nuclear reactors. *Energie Primaire 4* (1968), 3–43.

[64] Versteeg, H. K., and Malalasekera, W. *An Introduction to Computational Fluid Dynamics*. Pearson Prenctice Hall, 1995.

[65] Wallis, G. Critical two-phase flow. *Int. J. Multiphase Flow 6* (1980), 97–112.

[66] White, Frank M. *Viscous Fluid Flow*, 2nd ed. McGraw-Hill, Inc., 1991.

[67] Wilcox, David C. *Turbulence Modeling for CFD*, 3rd ed. DCW Industries, Inc., 1994.

[68] Winklhofer, E., Kull, E., Kelz, E., and Morozov, A. Comprehensive hydraulic and flow field documentation in model throttle experiments under cavitation conditions. *17th Annual Conference on Liquid Atomization and Spray Systems, Zurich, Switzerland* (2001), 574–579.

[69] Won Geun Lee, Rolf D. Reitz. A numerical investigation of transient flow and cavitation within minissac and valve-covered orifice diesel injector nozzles. *Journal of Engineering for Gas Turbines and Power 132*, 5 (May 2010). 052802.

[70] Zaloudek, F.R. The low pressure critical discharge of steam-water mixtures from pipes. *Interal Report: General Electric Co. Hanford Atomic Products Operation, Richland, Wash.* (1961), 1–46.

[71] Zeman, O. On the decay of compressible isotropic turbulence. *Physics of Fluids 3*, 5 (1991), 951–955.